POLITECNICO DI TORINO

Collegio di Ingegneria Chimica e dei Materiali

Corso di Laurea Magistrale
in Ingegneria dei Materiali per l'Industria 4.0

Master thesis

Laser-Powder Bed Fusion of AISI 316L-Cu Alloy: AI-Assisted Process Parameter Optimisation, Microstructure and Mechanical Properties Analysis

Supervisor
Prof.Abdollah Saboori

Candidate
Sanae Tajalli Noabri

December 2024

Abstract

Metal Additive Manufacturing (AM) has revolutionized the production of complex metal components by enabling the fabrication of intricate geometries with high precision. This technology's potential can be significantly enhanced through the integration of artificial intelligence (AI) methods, particularly Machine Learning (ML), which offers advanced capabilities in establishing complex interrelationships and improving system and product quality control. ML algorithms present a transformative opportunity to address manufacturing challenges, optimize resource consumption, and enhance process efficiency by exploring the intricate linkages between process parameters, material properties, microstructural characteristics, and their resultant properties. This thesis aims to determine the most precise ML algorithm for achieving the process parameters defect detection relationship of AI316L stainless steel alloy components containing 2.5% copper fabricated via the Laser Powder Bed Fusion (L-PBF) method. Recognizing these relationships enables the optimization of process parameters to attain specific objectives. This optimization method facilitates applications that balance productivity and quality, allowing the selection of parameters that satisfy both criteria. By defining these parameter relationships, ML models can be created to predict optimal process parameters based on desired outcomes, such as low defect content, high productivity, and low surface roughness, thus facilitating more efficient and customized AM processes. Following the assessment of multiple models with varying training and testing sizes for the relative density of samples, the Support Vector Regression (SVR) model has been identified as the most effective model. Moreover, the effect of adding Cu has been delineated by equiaxed and columnar grains and cells observed in SEM images. Melt pool dimensions have been analyzed across components with differing process parameters to assess their relationships qualitatively. Finally, printed samples underwent tensile testing to examine the relationship between porosity and mechanical properties. The SEM images of the fractured surfaces reveal both brittle and ductile fractures, with the brittle fracture displaying a quasi-cleavage plane, possibly indicating the melt pool boundary. The microscale analysis reveals ductile fracture characteristics with extensive dimple networks.

Key words: Additive Manufacturing, Machine learning, Laser-Powder Bed Fusion, Process Parameter Optimisation

Table of Contents

Tables

Figures

Table of Abbreviations

Abbreviation	Definition
AM	Additive Manufacturing
CNN	Convolutional Neural Network
DA	Discriminant Analysis
DED	Directed Energy Deposition
DEM	Discrete Element Method
DEM	Discrete Element Method
DMLS	Direct Metal Laser Sintering
DT	Decision Tree
EB-PBF	Electron Beam Powder Bed Fusion
ELM	Extreme Learning Machines
GA	Genetic Algorithm
GMA	Gas Metal Arc
GP	Gaussian Process
IoT	Internet of Things
k-NN	k-Nearest Neighbor
LBAM	Laser Beam Additive Manufacturing
L-PBF	Laser Powder Bed Fusion
ML	Machine Learning
NN	Neural Network
PA	Plasma Arc
PBF	Powder Bed Fusion
PSP	Process-Structure-Property
RHEA	Refractory High Entropy Alloys
ROC	Receiver Operating Characteristic
SeDANN	Sequential Decision Analysis Neural Network
SHS	Selective Heat Sintering
SLS	Selective Laser Sintering
SVM	Support Vector Machine
UQ	Uncertainty Quantification
CAM	Computer-Aided Manufacturing
CAD	Computer-Aided Design
XCT	X-ray Computed Tomography
UTL	Unsupervised Transfer Learning
XCT	X-ray Computed Tomography
ANN	Artificial Neural Network
OM	Optical Microscope

Abbreviation	Definition
GPR	Gaussian Process Regression
RFR	Random Forest Regression
SVR	Support Vector Machine
GBR	Gradient Boosting Regression
MAE	Mean Absoulute Error
MSE	Mean Squared Error
BD	Building Direction
VED	Volumetric Energy Density
EDS	Energy Dispersive X-ray Spectroscopy
HAZ	Heat Affected Zone
SEM	Scanning Electron Microscope
UTS	Ultimate Tensile Strenght

1. Introduction

Additive manufacturing (AM) is an innovative approach that constructs materials layer by layer, allowing for the creation of complex geometries from CAD designs [1]. AM enhances design flexibility and allows the processing of various materials, including polymers, metals, ceramics, and composites [2]. In contrast to traditional manufacturing methods, AM offers significant benefits, including enhanced material utilization efficiency and the ability to produce structures that closely approximate their final shapes[3]. Selective Laser Melting (SLM) is one of the advanced powder bed fusion (PBF) additive manufacturing techniques. SLM, also known as Laser Powder Bed Fusion (L-PBF), utilizes high-power lasers to melt powder layer by layer selectively. This technique can yield exceptional mechanical properties when process parameters are carefully optimized [4–6]. Although the L-PBF process has demonstrated effectiveness in the rapid manufacturing of complex components, the potential applications of printed components can be limited because of some problems, such as the small value of densification [7], elevated surface roughness[8], tensile residual stresses[9], and anisotropic structures [10–12]. However, these problems can be resolved by optimizing process parameters to achieve the desired quality of LPBF-produced parts [11]. Achieving this goal requires an in-depth investigation of all critical parameters and their influence on the mechanical and microstructural properties of the fabricated components. Even though more than 130 distinct process parameters can influence the LPBF process[13], factors such as laser power, scanning speed, hatch spacing, and layer thickness are recognized as the most effective hyperparameters impacting the characteristics of the printed structures [14,15]. Despite AM's advantages, Metal AM has a notable constraint which is a limited number of compatible materials [16]. This restricts its applicability across various fields, especially in specialized industries requiring specific material properties, such as the biomedical sector. A considerable effort has been dedicated to developing novel alloys with customizable properties to address this issue. This thesis focuses on a 316L stainless steel alloy with a 2.5% copper addition. This alloy was engineered to possess antibacterial properties, making it appropriate for applications within the biotechnology field.

This work investigates the accuracy of seven supervised machine learning algorithms in predicting the process parameter defect content relationship of AISI316L-Cu stainless steel specimens manufactured by L-PBF using different combinations of process parameters, such as laser power, scanning speed, and hatch distance. The models' performance is evaluated using R^2, MAE, MAPE, and IM error estimators. This thesis aims to demonstrate the capability of Machine Learning to generate precise predictions of process parameter defect detection relation especially with different priorities, such as productivity or surface quality. This predictive ability allows for accurately customizing the additive manufacturing processparameters to meet specific requirements, thereby improving the optimization process. This emphasis is directly associated with enhancing efficiency in additive manufacturing and seeks to make substantial contributions to progress in this domain. Developing optimum process parameters for new materials is often time-consuming, costly, and environmentally unsustainable. Traditional parameter optimization methods frequently require extensive trial-and-error experimentation,

significantly investing time and resources. Due to these challenges, machine learning (ML) techniques, which offer a data-driven methodology for optimizing AM process parameters, have been the focus of this study. This thesis aims to improve parameter development using machine learning to attain desired features, such as enhanced build rates, increased productivity, optimized surface quality, and reduced defect content.

Chapter 2, titled "State of the Art," thoroughly examines current additive manufacturing technologies and machine learning. This study initially examines two significant additive manufacturing technologies including powder bed fusion (PBF) and directed energy deposition (DED). These technologies possess distinctive characteristics and are affected by multiple factors. This chapter investigates the different categories of machine learning techniques, such as supervised, unsupervised, semi-supervised, and reinforcement learning, and their application in prior research to enhance AM processes. It emphasizes explicitly recent advancements wherein researchers have employed machine learning models to forecast and regulate results. These advancements encompass the optimization of parameters for enhanced mechanical properties, the regulation of geometric deviations, and the real-time detection of defects. Comprehensive descriptions of the methodologies employed in this research are available in Chapter 3, Materials and Methods. This chapter outlines the procedures implemented in sample modeling, including the experimental design framework established to modify the process parameters consistently. A discussion follows regarding the diverse sample fabrication methods, concentrating primarily on how different process conditions affect the material's properties. This section of the chapter examines the characterization techniques employed to assess the samples' physical, mechanical, and microstructural properties. An example is X-ray computed tomography, which provides a non-destructive method for analyzing internal porosity. Archimedes' density measurements, conversely, offer insights into the material's overall density. Moreover, metallographic techniques are employed to prepare and analyze samples for microstructural assessment. Comprehensive parameter optimization can be reached by using these characterization techniques in conjunction, as they provide the necessary data for training and evaluating machine learning models. Chapter four, "Results and Discussion," presents the findings from the experiments and the assessments of the machine learning models. The initial section of the chapter outlines the procedures for data acquisition and preprocessing, along with an outline of the data partitioning for training and testing purposes. The parameter tuning method is clarified, wherein several machine learning models were employed to examine the relationship between the process parameters and the sample outcomes. Visualizing and interpreting the effects of various parameters were achieved using techniques such as heat map correlation plots, 3D surfaces plots, and 2D plots derived from hyperparameter optimization. The chapter also addresses selecting the final model based on evaluation metrics to achieve an optimized parameter set that fulfills the desired objectives. This chapter includes a comprehensive analysis of the material's mechanical properties and microstructural characteristics, alongside the optimization of parameters. It examines how variations in process parameters influence grain size, melt pool geometry, and porosity distribution within the samples. The mechanical testing results, encompassing tensile strength measurements, provide further insights into the material's performance across various conditions.The concluding chapter, entitled "Conclusion and Future Perspective," provides a

summary of the thesis's key contributions and discusses potential avenues for future research. This chapter underscores the significance of employing machine learning to enhance additive manufacturing technologies. The chapter also emphasizes the potential for additive manufacturing to enhance sustainability and resource efficiency as machine learning techniques advance. The advancement of sensors for real-time monitoring and regulation is the emphasis of future outlooks. These sensors possess the capacity to enhance the adaptability and reliability of additive manufacturing. This chapter additionally addresses the growing importance of data volume, velocity, and variety in additive manufacturing. The integration of larger, more complex datasets may yield models that are significantly more accurate and predictive. The results presented herein emphasize the capacity of machine learning and additive manufacturing to transform material development, enabling the production of customized, high-performance components across various industries.

2. State of the art

AM has offered a substantial revolution in the manufacturing process of metal components. This technology facilitates the production of complex geometries with great precision. It also provides the capability to generate localized alterations in microstructure and properties through targeted adjustments in the manufacturing process. The persistent issue of achieving consistent and high-quality outcomes for varied applications persists despite the considerable efforts made by individuals over the years that have resulted in the commercialization of metal AM technologies [17]. Direct metal AM processes can primarily be classified into two major technological categories: PBF and Directed Energy Deposition (DED). These two direct AM processes have gained substantial prominence in academic research and industrial applications, making them the primary focus of interest. In DED, material is supplied through a moving nozzle, while PBF adds thin layers of powder after each fusion step. Both methods involve melting the material with a heat source like a laser or electron beam [10,18].In recent years, extensive research has been conducted to enhance the efficiency of AM processes. One of the most effective tools for improving AM performance is using artificial intelligence (AI). AI technologies, such as machine learning (ML), automation, robotics, machine vision, data mining, extensive data analysis, and expert systems, have presented their efficacy in manufacturing [19]. ML proves to be a potent tool for enhancing the quality and efficiency of metal AM [20]. It can also play an important role in enhancing the quality of printed components, particularly when basic physical principles are not well known but data on process variables, alloy properties, and product characteristics are accessible [21]. Integrating ML with AM can detect defects early, reduce waste, optimize input and output characteristics, and improve speed and accuracy, ultimately enhancing the quality [22].

ML methods have gained considerable interest for their exceptional performance in various data-related tasks, including regression, classification, and clustering. These approaches can be classified into supervised, unsupervised, semi-supervised, and reinforcement learning based on the extent and nature of supervision needed during the training process [23]. Integrating these powerful ML techniques presents an exciting opportunity to revolutionize manufacturing processes, tackle challenges, and optimize resource utilization. By considering the parameters

of the AM process and the material properties, part geometry, and microstructural characteristics as inputs for ML algorithms, it becomes possible to establish a relationship known as Process-Structure-Property (PSP). Various linkages and correlations may be observed among data, including optimizing processing parameters and property prediction, cost estimation, defect identification, in-situ monitoring, and controlling geometric deviations. [24].

Consequently, this thesis will comprehensively analyze the applications of ML in two laser-based AM technologies, L-PBF and DED. The papers under discussion within the context of this thesis text provide an overarching view of ML applications in AM. They have investigated ML applications in AM either comprehensively or independently, focusing on specific processes such as L-PBF or DED in their respective publications. However, it is worth noting that the number of papers with a focus on ML general applications in AM [17,24,25] is notably higher than those that specifically address L-PBF [26–28] or DED [29–31], which tend to be less frequent in the literature. The reason for the selective analysis approach in this thesis is twofold. Firstly, a deeper and more comprehensive understanding of the practical applications of ML in L-PBF and DED is facilitated by focusing on them. The unique difficulties and challenges associated with L-PBF and DED, which may be overlooked in broader studies, can be explored by this approach. Secondly, generalization problems can be avoided by concentrating on these two processes. By emphasizing L-PBF and DED, more actionable insights can be provided into how ML can be effectively applied in these specialized areas. This approach enables real-world challenges to be addressed and innovative solutions to be offered.

Table 1, extracted from the Scopus database using the keywords listed in Table 1, shows a significant increase in the number of articles on integrating ML in AM. This surge can be attributed to the growing importance of the subject. The chart generally demonstrates the broad application of ML in AM.

Table 1. Keywords used to search and obtain data from the Scopus database

Application of ML in AM	Application of ML in L-PBF	Application of ML in DED
(TITLE-ABS-KEY (machine AND learning AND in AND additive AND manufacturing) AND (LIMIT-TO (SUBJAREA, "ENGI")) AND (LIMIT-TO (DOCTYPE, "ar") OR LIMIT-TO (DOCTYPE, "cp") OR LIMIT-TO (DOCTYPE, "re")) AND (LIMIT-TO (LANGUAGE, "English")))	(TITLE-ABS-KEY (machine AND learning AND in AND laser AND powder AND bed AND fusion) AND (LIMIT-TO (SUBJAREA, "ENGI")) AND (LIMIT-TO (DOCTYPE, "ar") OR LIMIT-TO (DOCTYPE, "cp") OR LIMIT-TO (DOCTYPE, "re")) AND (LIMIT-TO (LANGUAGE, "English")))	TITLE-ABS-KEY (machine AND learning AND in AND directed AND energy AND deposition) AND (LIMIT-TO (SUBJAREA, "ENGI")) AND (LIMIT-TO (DOCTYPE, "ar") OR LIMIT-TO (DOCTYPE, "cp") OR LIMIT-TO (DOCTYPE, "re")) AND (LIMIT-TO (LANGUAGE, "English"))).

Furthermore, it is worth noting that the number of articles studied for DED is significantly lower than L-PBF. Despite this, both processes are the focus of the current paper. This approach

is motivated by the desire to provide a more detailed and specialized analysis of these AM techniques, recognizing their unique requirements and challenges.

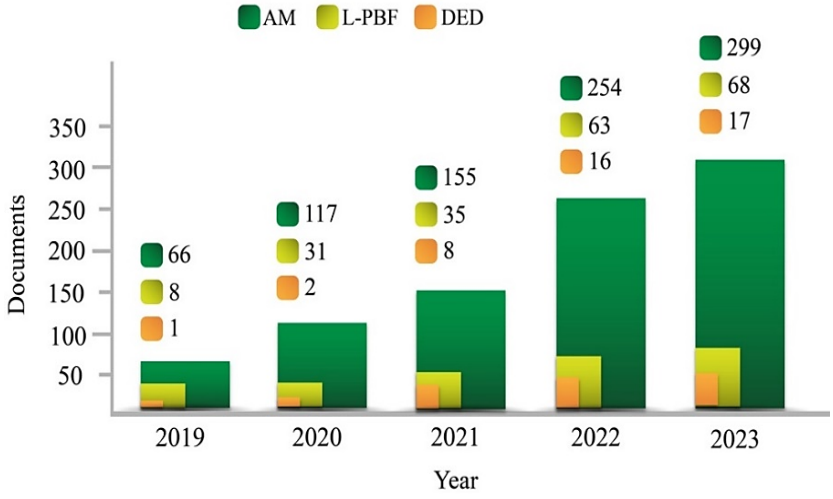

Fig. 1. The number of published papers on the application of ML in various AM methods as a function of publication year. The data was extracted according to the keywords tabulated in Table 1.

2.1. Additive Manufacturing

Metallic components can be produced via direct metal AM immediately after being designed in a single processing step [32]. During the AM process, complex shape components are built layer upon layer following a digital layout. This distinct characteristic enables the production of intricate or tailor-made components directly from the design, eliminating the need for costly tooling or shaping tools like punches, dies, or casting molds and diminishing the number of traditional processing stages [10]. Manufactured metallic parts are utilized in various industries, including aerospace, healthcare, energy, automotive, marine, and consumer products [33]. Examples of these components include metal implants designed for specific patients [34], turbine blades with cooling channels [35], manifolds for engines and turbines, and lattice structures and truss networks optimized for a better strength-to-weight ratio [36].

According to ASTM F42, AM processes can be broadly categorized into seven classes: Vat photopolymerization (VP), Material Extrusion (ME), Material Jetting (MJ), Binder Jetting (BJ), PBF, DED, and Sheet Lamination (SL) [37]. PBF and DED methods differ based on the feedstock (powder or wire) and the heat source, which can be a laser, electron beam, plasma arc, or gas metal arc. Electron beam processes are conducted in a vacuum or low-pressure inert gas environment, allowing the use of reactive metals. In contrast, some heat sources require the parts to be shielded using an inert gas [18]. Certain AM processes, known as indirect metal AM processes, can consolidate metallic materials in the form of thin sheets and ribbons using ultrasonic methods without melting the feedstock material. Additionally, Alloy powders can be fused by jetting a binder onto a powder bed and then sintering it in a high-temperature furnace [10].

2.1.1. DED

DED is becoming increasingly popular since its mechanical properties are comparable to typical manufacturing techniques. DED is an AM method that uses concentrated thermal energy, such as a laser, electron beam, or plasma arc, to liquefy and place materials, forming solid three-dimensional (3D) structures layer-on-layer [38]. This manufacturing method is faster and more cost-effective than subtractive manufacturing. It can produce intricate parts with minimal material waste. Furthermore, DED exhibits exceptional efficacy when utilized for repair and remanufacturing purpose [39]. DED can be classified into two categories based on the feedstock used: wire feed DED and powder feed DED, as depicted in Fig. 2. In the powder feed system, the material undergoes melting during the deposition process, but in the wire feed system, a laser or arc is used to fuse the wire on the substrate. The energy source is concentrated in a particular location, where it deposits the feedstock onto the previous layer (or the substrate for the first layer) simultaneously. This procedure involves the creation of a melt pool by melting both the raw material and the layer before it. The resulting deposition bead is formed as the substance cools down [40].

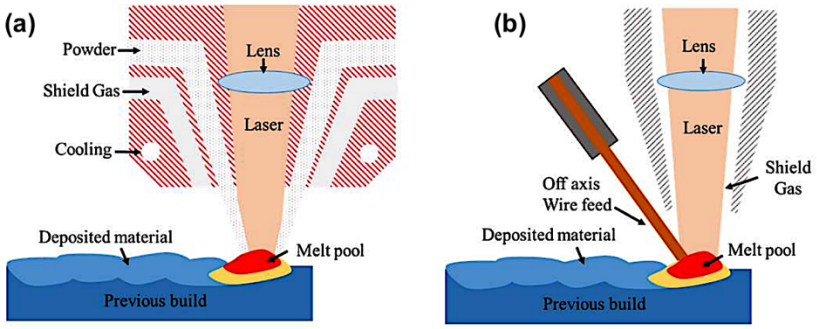

Fig. 2. Schematic illustration of DED system [41]. (a) Powder feed DED system; (b) Wire feed DED system.

In contrast to wire feed DED, powder feed DED provides higher printing accuracy, although at a comparatively reduced printing speed. Despite its considerable advantages compared to other metal additive manufacturing technologies, DED still has difficulties in attaining satisfactory surface finishes and minimizing porosity and cracks in the produced componen [42]. Microstructural defects can arise from several reasons, including trapped gas, insufficient fusion, fast solidification, and inadequate powder melting [43]. An important obstacle faced by the expanding DED sector is the considerable variation in the quality of produced components. This variability is controlled by several aspects, such as process parameters, laser-material interactions, and defect creation. Although large-scale experimentation or simulation can enhance print quality, these approaches are frequently characterized by their time-consuming and costly nature. Insitu-monitoring is an alternative method for optimizing the quality of DED parts. However, this approach is highly challenging because of the enclosed chambers and the elevated temperatures of the melt pool, which can reach up to 2000-3000 °C. Despite generating substantial real-time process data, in-situ process monitoring offers a promising option [29]. Wire-based DED is a process similar to traditional welding that uses high power to create thick layers at high deposition rates, allowing for the economical production of large

parts. However, parts produced using GMA-DED, PA-DED, and L-DED usually require machining due to significant surface waviness caused by the formation of large molten pools [18].

2.1.2. PBF

PBF is widely recognized as the primary AM method due to its advanced ability to manufacture metallic and non-metallic components with remarkable precision. Moreover, PBF may produce homogenous alloy components with remarkable strength and facilitate free-form manufacturing, therefore offering various advantages. The utilization of lightweight construction and design flexibility facilitates the achievement of decreased local manufacture of components [44]. In PBF, thin layers of powder are added after melting the last one. Instead, in DED, a laser, electron beam, or arc heat source is used to melt the feedstock, which can be in the form of a powder or wire, and it is supplied from above the object. DED involves melting the feedstock, which can be powder or wire, using a laser, electron beam, or arc heat source. In contrast to PBF, most DED processes do not have limitations in terms of bed or box size, making it possible to produce large components [10,18,45]. L-PBF, as a subset of PBF, specifically employs laser technology for AM. The critical distinction between L-PBF and other AM techniques is the use of laser, which provides high precision and control during the process. This review paper investigates L-PBF and EB-PBF methods within this context, as they have unique operational principles that significantly differentiate them. Solid components are formed from powdered material through heating, direct liquefaction, and subsequent solidification, particularly in L-PBF. Laser and electron beams serve as the primary heat sources to ensure high precision in producing these parts. The procedure proceeds by overlaying the preceding layer with the subsequent layer of powder from a pre-deposited powder mixture using a re-coater blade or roller(Fig. 3.)

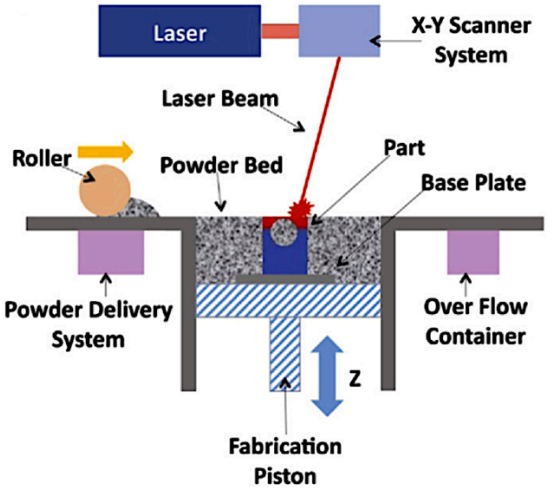

Fig. 3. Schematic of the L-PBF process [43].

The unmelted particles in the powder bed serve as structural supports for the printed components. Following the melting and solidification of a layer of powder, the build platform

descends, allowing a fresh layer to be applied and melted on top of the preceding one. Thermal rates in laser powder bed fusion can range from 10^3 to 10- Kelvin per second [46]. This method is very efficient for printing intricate Geometries, capable of handling a diverse array of materials, and necessitates little support structures. In the realm of large-scale production of gradient-structured metals and alloys, 3D printing emerges as a highly effective technique for fabricating gradient structures characterized by intricate architectures. Nevertheless, there are still obstacles to overcome, such as the presence of flaws during the printing process and the inclination for gradient structures to exhibit considerably greater grain sizes, frequently surpassing 100 nm. To address these challenges, it is essential to optimize parameters such as power density, powder flow rate, scanning speed, and hatch spacing for each alloy [47].

Identifying the suitable process frame to manufacture 3D components with exceptional microstructural and mechanical qualities is the main obstacle in employing metallic powders in L-PBF. Therefore, some research has concentrated on maximizing the optimization of LPBF process parameters. These investigations can be classified into three primary groups: laser-related, powder-related, and powder-bed-related characteristics [48].

2.1.2.1. Powder-related parameters

In manufacturing, powder-related factors such as chemical composition, surface morphology, and particle size distribution are assumed to be relatively constant [49]. The chemical makeup of the powder is essential in determining the LPBF process and its related parameters. The results suggest that minimal alterations in the chemical composition have little effect on the densification behavior. However, the powder's chemical makeup does impact its microstructure, which subsequently affects its mechanical characteristics. Kempen et al[49]. discovered that augmenting the silicon (Si) concentration in the AlSi10Mg alloy leads to improved laser energy absorption in the powder bed, thereby enhancing overall processability. The shape of the starting powder significantly dictates the ultimate quality and density of parts produced by LPBF processing. The powder morphology is a determining factor in the degree of compactness of powder particles when a new layer is deposited on top of an existing metal layer. Thus, morphology plays a vital role in determining the thickness of the layers and the roughness of the surface of the manufactured SLM component. Additionally, it determines the dimensions and morphology of the powder particles, which are significantly affected by manufacturing techniques like as gas-atomization and mechanical alloying/milling. Chang et al. [49] examined how particle size affects the microstructural characteristics, constitutional phases, and mechanical qualities of parts produced by LPBF processing. Their findings demonstrated that decreasing the size of powder particles enhances the uniformity of the microstructure of the resulting product. Erika Lannunziata Chang et al[50]. focused on investigating the impact of the powder atomization method on the densification, roughness, and mechanical characteristics of AISI316L samples manufactured using the L-PBF technique. Their results illustrated that when density statistics were considered, gas-atomized samples frequently exhibited higher density due to their decreased oxygen concentration and enhanced flowability.

2.1.2.2. Laser-related parameters

The dimensions of the laser system, including its type (pulsed or continuous wave), spot size, and laser power, as well as scanning parameters such as scanning strategy, speed, and hatch spacing, greatly influence the properties of the constructed component [49]. These parameters significantly impact the characteristics and excellence of components produced by LPBF and are essential for defining the energy density or energy input. The term "energy density" denotes the extent to which a unit volume of powder absorbs energy during the process of melting. Enhancing the laser energy density can optimise the density of manufactured components, even when subjected to various atmospheres like argon, nitrogen, or helium, as illustrated in Fig. 4. Yet, in the case of Al–12Si components, there exists a critical energy level of 30 J/mm³, below which the energy is inadequate to completely liquefy the powder, resulting in reduced density and heightened porosity [49], as seen in Fig. 4. Moreover, over this limit might have a negative impact on the surface quality by causing the development of balling [46].

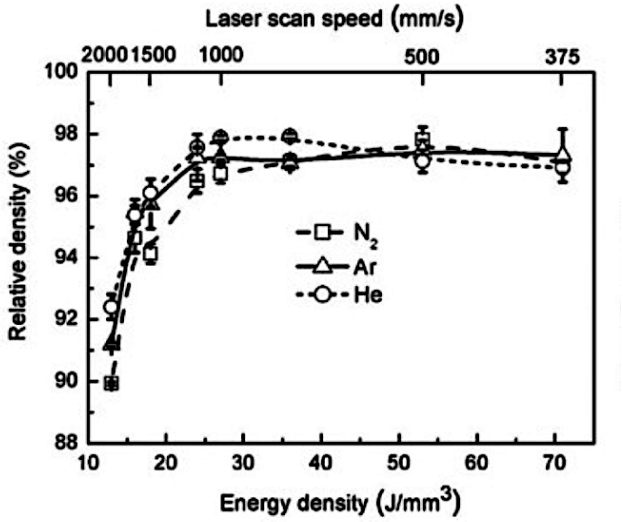

Fig. 4. Analysis of the relationship between relative density and incident laser energy for Al–12Si components treated using LPBF. The result evidences a positive correlation between laser energy density and relative density. At energy densities below 30 J/mm³, the energy is insufficient to completely melt the powder, leading to a reduced relative density. Once this threshold is surpassed, the relative density stabilizes at [46].

The increasing general acceptance of LPBF technology is hindered by the substantial hurdles presented by residual stresses and deformation in LPBF-built parts. During Laser Powder Bed Fusion Fusion (LPBF), the application of localized heat generates significant temperature gradients, resulting in stress inside the manufactured components. Plastic deformation happens when the thermomechanical stress exceeds the yield strength of the material. Repetitive thermal cycles from consecutive layers can lead to the buildup of stress and deformation, which may ultimately lead to failure and significant distortion of the LPBF components, including cracking and layer delamination. As a result of its impact on local heat distribution, the scanning technique significantly affects these deformations and residual stresses [46].

Complex parts with fine and closely spaced features can be printed using tiny diameter beams and small metal powders. These metal printing processes differ in their heat source power,

scanning speed, deposition rate, surface roughness, and other essential features, as depicted in Fig. 5 [10].

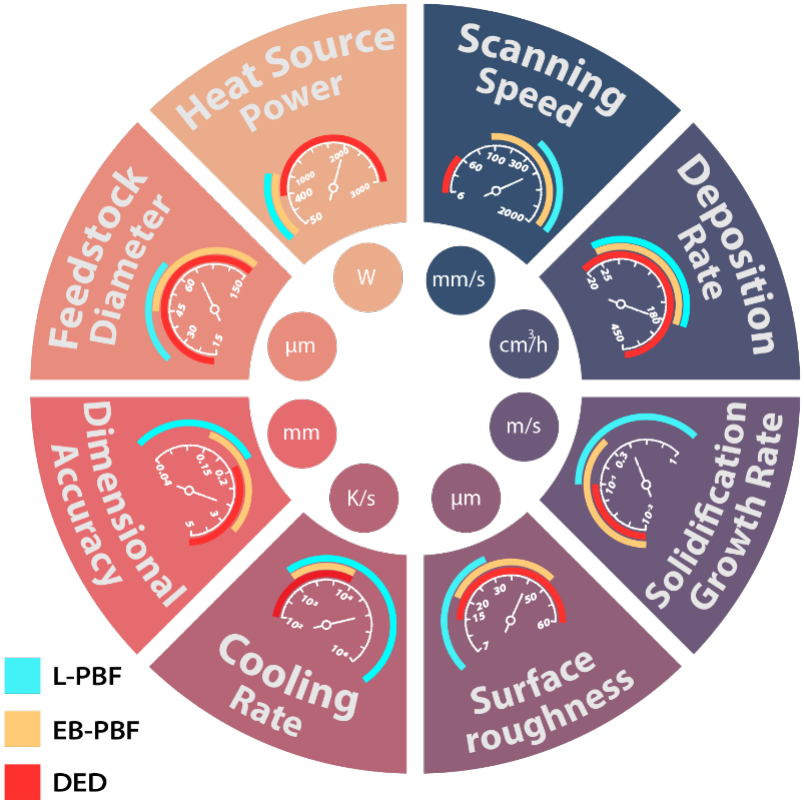

Fig. 5. Process parameters for various AM methods upon consulting Refs [10,18,33,51–56]. The surface roughness represents the average deviation of the surface from its mean height.

These parameter differences can cause a 10,000-fold variation in cooling rates and notable differences in temperature gradient and heat input among various AM methods. As a result, the microstructure and properties of components are affected by the cooling rate and heat input, which is why the parameters shown in Fig. 5 must be controlled with more effective approaches than in conventional processes to ensure the production of high-quality and dependable parts [44,57–60].

Achieving precise control over the microstructure, defects, and properties in AM processes is still a challenge due to the need for extensive experimentation to explore a wide range of process parameters. Printing conditions are often selected based on the machine manufacturer's recommendations or through trial and error [61]. Trial and error methods are not ideal for improving part quality in AM due to the expensive nature of the feedstock and machines [51], as well as the fast-evolving economic culture that leads to the creation of new products at a rapid rate. Instead, mechanistic models can predict various physical attributes of AM parts, such as temperature fields, solidification characteristics, microstructure, and defect formation. These models rely on a phenomenological understanding of the process variables and thermophysical properties of alloys [62].

2.1.3. AI in AM

The use of AI methods in digital manufacturing is becoming increasingly prevalent due to advancements in data acquisition technologies, robotic systems, and computer science [63]. These methods, including ML, automation, robotics, machine vision, data mining, big data analytics, and expert systems, have all demonstrated their effectiveness in enhancing control over systems and product quality [19]. ML can assist in various stages of the AM process by analyzing data on process variables, alloy properties, and product attributes. This analysis can help reduce defects, achieve superior microstructures and properties, and accelerate product qualification. Additionally, using ML and developing mechanistic models can create opportunities for producing novel alloys [51]. The combined use of mechanistic models and ML is crucial for various aspects of AM, including designing, planning, producing, characterizing, and evaluating the performance of printed parts (see Fig. 6)

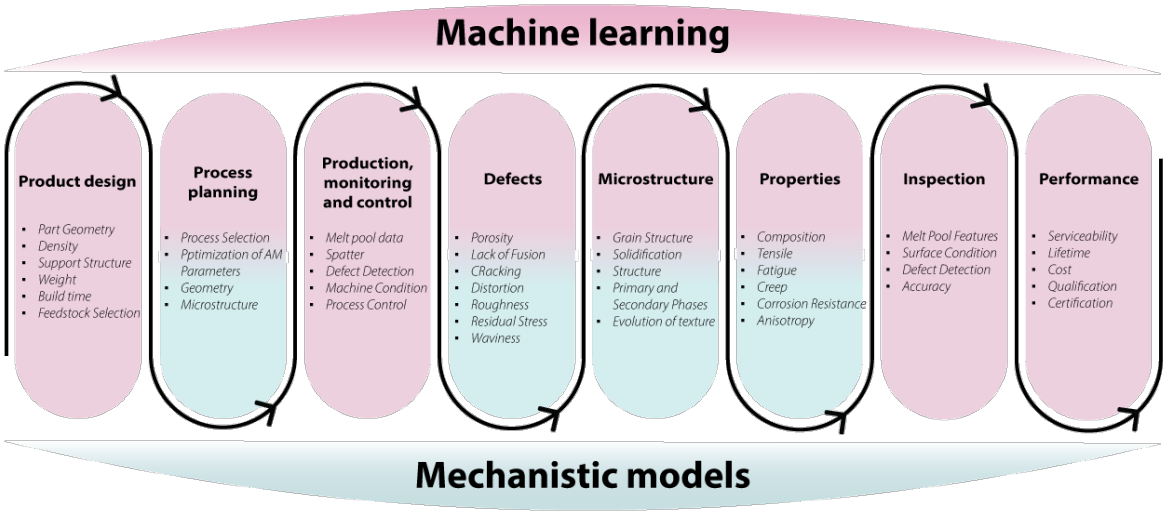

Fig. 6. Application of mechanistic models and ML in the various steps of metal AM. Both mechanistic models and ML offer a quantitative framework for understanding the characteristics of components. This figure illustrates the respective roles of ML and mechanistic models at different stages in manufacturing and analyzing elements.

The integration of ML with AM processes presents an opportunity to effectively address defects during the early stages and stop the production of defective components as soon as a defect is detected. ML can optimize input and output characteristics and predict the properties of a component, while also enhancing AM process speed, accuracy, and efficiency, ultimately influencing quality outcomes [22,64].

2.2. Machine Learning

Machine learning methods have gained considerable interest due to their exceptional performance in various data-related tasks, including regression, classification, and clustering. As seen in Fig. 7, these approaches can be classified into supervised, unsupervised, semi-supervised, and reinforcement learning, based on the extent and nature of supervision required during the training process [23]. Supervised learning involves labeled data that is divided into training and testing sets. The primary objective is to develop models that establish links between predictors (features) and the response (target) within the dataset [65]. In contrast, unsupervised learning does not require labeled data or a training set to create the model. In the case of semi-supervised learning, a small portion of the dataset is labeled, enabling the system to learn from these labeled samples and classify a larger volume of data. Reinforcement learning differs from other machine learning methodologies by using a reward-and-penalty framework for algorithm training [32].

Fig. 7. Three different approaches for the classification of ML.

ML models can also be classified as batch/offline learning or online learning. In the case of offline learning, the model cannot learn incrementally and must be trained using all available data, which demands substantial time and computing resources. Online learning enables the model to learn dynamically, and incrementally as new data is presented without the need to retrain the entire model. This methodology is particularly appropriate for working with large and continuously expanding datasets [23]. Likewise, ML approaches can be categorized as instance-based or model-based learning. Instance-based models use a similarity measure to identify new cases, while model-based learning involves constructing and using a model for predictions. In the field of AM, ML approaches are typically offline instance-based or model-based, incorporating supervised or unsupervised learning models [23]. As depicted in Fig. 8,

each method in machine learning uses multiple algorithms, which are elucidated in the accompanying table.

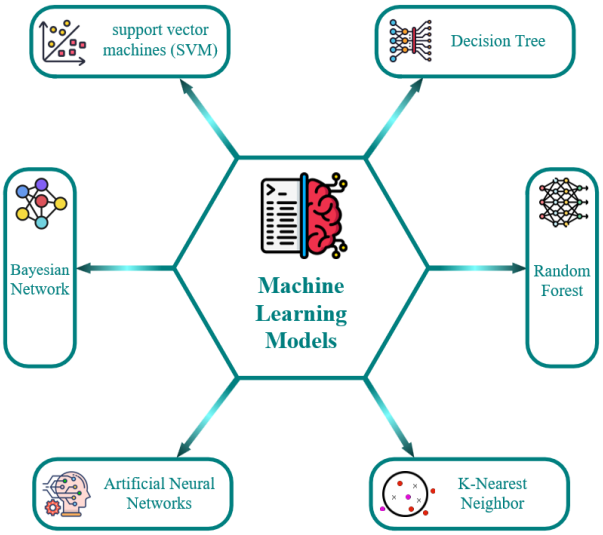

Model	Description
	Used for classification and regression, the model can split data into groups based on their locations in feature space; the features of the data fully determine their locations and there is no stochastic element involved.
	Progressively classifies a group of variables based on rules and displays them as an upside-down tree; the root of the tree often displays the most important variable, and the apex shows the least important variable
	Consists of multiple decision trees, each with a classification; the forest gets a classification from the attributes of the greatest number of trees; for regression, the model considers the average of the outputs of different trees
	Separates data into different classes based on the attributes or the class of the majority of the nearest neighbours; the number of nearest neighbours, k, is selected by trial and error
	Layers of hidden nodes connect input and output variables; an activation function is used to connect nodes with each other; errors in predictions are minimized by adjusting weights for each connection.
	A statistical model that represents the probabilistic relation between cause and effect; the conditional probabilities are computed using Bayes' theorem

Fig. 8. Some of the most essential ML algorithms with their description.

2.2.1. Supervised Learning

Supervised learning is the most frequently employed method among machine learning techniques [66]. In this method, a model can be developed by training the dataset to accurately classify labeled data within the test set [67]. However, acquiring labeled data for training supervised learning models can be challenging and costly, especially for large datasets. Additionally, the manual labeling process is susceptible to human bias, which can further degrade the accuracy of the model [23]. Supervised machine learning is divided into two main categories: classification and regression methods. Classification methods contain SVMs, DTs, Naïve Bayes, k-NNs, and ANNs. These methods rely on the "pattern recognition" principle to categorize data. Conversely, regression involves predicting continuous values by analyzing a dependent variable concerning one or multiple independent variables. This procedure provides the optimal pattern that best fits the given data [68]. In supervised learning, the ML model

adjusts the weights assigned to input variables iteratively until it achieves an optimal data fit. This process involves an algorithm that identifies patterns within a training dataset. As shown in Fig. 9, some specific considerations and preliminary measures must be undertaken to execute this task [66,69]:

1. Acquiring a dataset and data processing
2. Feature selection (target variable)
3. Splitting the dataset (training, cross-validation, testing)
4. Hyperparameter tuning and prediction.

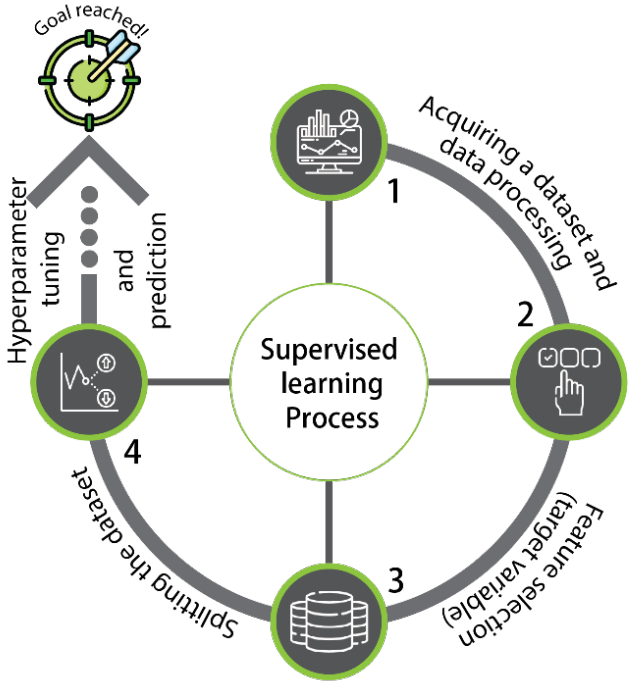

Fig. 9. The steps required for developing ML models based on supervised learning algorithms.

Supervised learning algorithms can address various numerical engineering problems. Each input data point is associated with a corresponding output variable Y, and the training dataset comprises multiple input-output pairs [70]:

$$\boldsymbol{Y} = \begin{bmatrix} \boldsymbol{y_1} \\ \boldsymbol{y_2} \\ \vdots \\ \boldsymbol{y_n} \end{bmatrix} \tag{1}$$

Meanwhile, various mathematical techniques can be employed to represent scalar values in the context of observations. These observations are typically organized in rows, with each column representing a specific feature. This arrangement of statements leads to the formation of a matrix structure [71]:

$$\boldsymbol{X} = \begin{bmatrix} \boldsymbol{x_{1,1}} & \boldsymbol{x_{1,2}} & \cdots & \boldsymbol{x_{1,n}} \\ \boldsymbol{x_{2,1}} & \boldsymbol{x_{2,2}} & \ldots & \boldsymbol{x_{2,n}} \\ \vdots & \vdots & \ddots & \vdots \\ \boldsymbol{x_{n,1}} & \boldsymbol{x_{n,2}} & \cdots & \boldsymbol{x_{n,n}} \end{bmatrix} \quad (2)$$

In this method, datasets can take various forms, including photos, audio samples, and text. The error between the predicted and actual output values is calculated using an objective function known as the cost function. To provide an unbiased assessment of the model's accuracy, a trial phase is conducted using a test set consisting of previously unseen additional information [70].

2.2.1.1. Regression Learning for AM Applications

Regression analysis is a valuable tool for predicting and optimizing various process parameters for AM applications. Several studies have explored the applications of this technology, providing valuable insights into how it can enhance manufacturing processes and product quality. For instance, Eshkabilov et al. [72] implemented an SVR algorithm to establish the relationship between process parameters and the relative density, hardness, yield strength, and tensile strength of samples produced by L-PBF. Similarly, a random forest regression (RFR) model was developed by Peng et al. [73] to determine the correlation between the fatigue behavior of AlSi10Mg alloy and the defects of parts manufactured by L-PBF. In another work, Caiazzo et al. [74] applied an NN model to correlate laser power, scan speed, and powder feeding rate with geometrical parameters of the deposited track, highlighting the significant impact of regression analysis in optimizing AM processes.

2.2.1.2. Classification Learning for AM Applications

Classification analysis has also proven to be a valuable tool in various fields of AM for categorizing and optimizing diverse process parameters through different algorithms. Khanzadeh et al. [75] used multiple ML algorithms, including KNN, SVM, DT, and DA, to detect defects. Fig. 10 illustrates a procedure that uses images as input for defect detection in the L-PBF process of Ti-6Al-4V. For each thermal image labeled as porous or non-porous, geometric features are extracted and used to train the ML models.

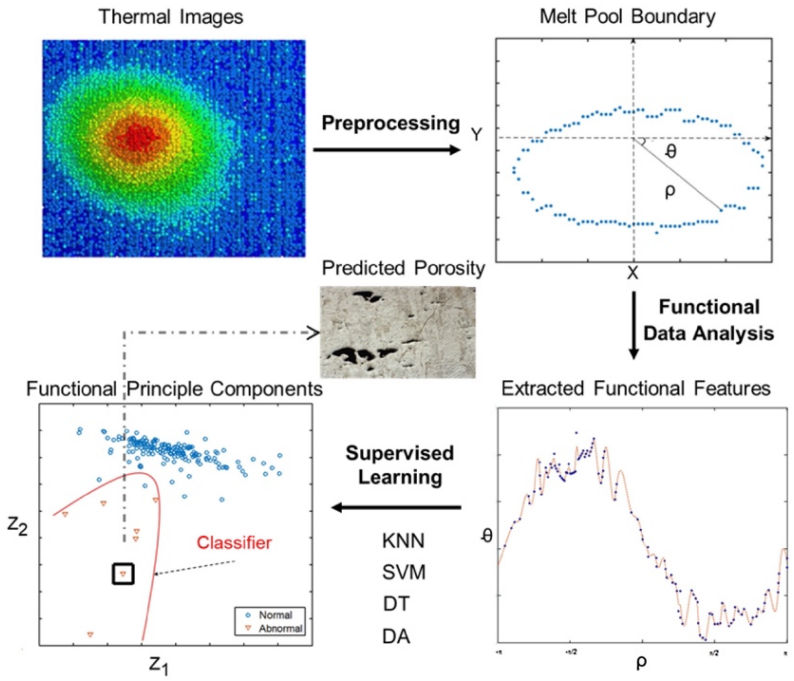

Fig. 10. Illustration of the process for predicting porosity through supervised machine learning [75].

SVM is another well-known ML tool that efficiently handles classification and regression tasks. This algorithm has garnered significant attention from researchers, especially in defect detection. The SVM algorithm relies on hinge loss for its operation. The exponential loss is associated with the classic boosting method, while the logistic loss function is linked to logistic regression. The logistic loss function is significant as it serves classification purposes and is prominent in ML problems [76,77]. The mathematical expression for logistic regression is articulated as follows:

$$\text{Log Loss} = \sum_{(x,y)\in D} -y\log(\acute{y}) - (1-y)\log(1-\acute{y}) \qquad (3)$$

In the context of logistic regression, the dataset $(x, y) \in D$ consists of a significant amount of data with various labels. In this classification task, the variable y denotes the chosen label applied to a particular instance. It is essential to acknowledge that logistic regression commonly deals with binary classification, wherein the dependent variable y assumes either 1 or 0 values. However, the variable (y') represents the estimated value, which falls within the continuous range of 0 to 1 [78].

In classification problems, NNs stand out as one of the most widely adopted algorithms. Traditional NNs are typically employed when dealing with inputs consisting of parameters and class labels. However, for tasks involving images, handwritten digits (see Fig. 11), and autoencoders, a specialized form of NN algorithm known as CNN is specifically designed to provide practical solutions [79]. This model initially dissects image characteristics such as curves, edges, and lines in the early layers. Subsequent layers then organize and synthesize these features, while the final layers are responsible for reconstructing the image from scratch [79,80]. In another task, Yuan et al. [26] investigated the application of CNN to predict the continuity of L-PBF tracks. The ML model was fed with melt pool images captured at various printing positions. Variances in melt track width resulted from adjustments to L-PBF process

parameters. The algorithm primary task for each track was to evaluate the mean and standard deviation of track width and achieve a 93% precision rate in classifying track continuity.

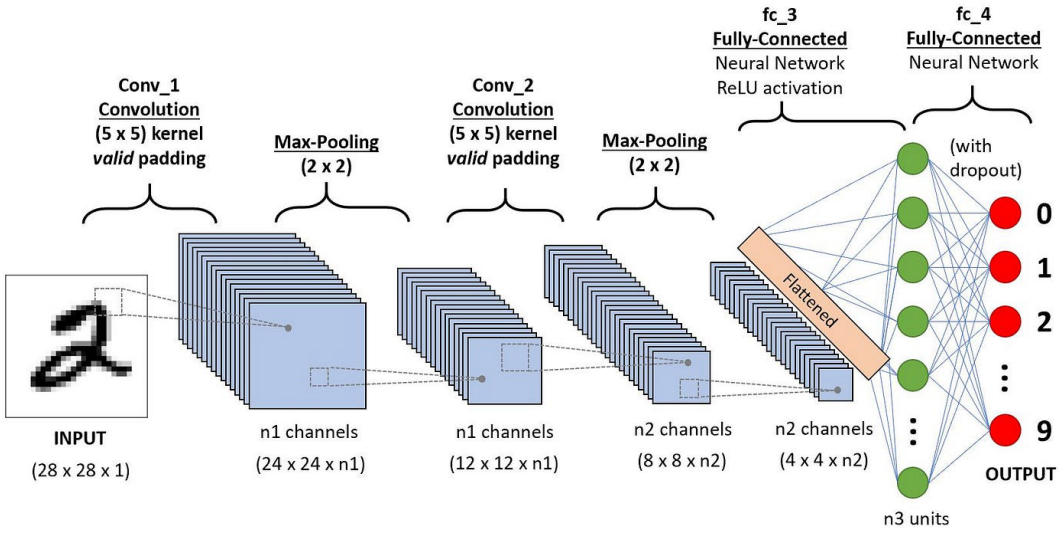

Fig. 11. Schematic of CNN algorithm for classifying handwriting digits [66,81].

2.2.2. Unsupervised Learning

Unsupervised learning is a machine learning method that aims to identify previously unknown patterns within a dataset without predefined targets or labels. Unlike supervised learning, which relies on labeled training data, unsupervised learning, also known as self-organization, can construct probability density models using input data with minimal human supervision [82]. Unsupervised learning is employed to explore algorithmic approaches that can effectively organize complicated inputs and detect elemental patterns with limited human guidance to create improved predictive systems [68]. For instance, UTL has been used as a promising approach for anomaly detection in industrial applications. It is a specific type of unsupervised ML that can train abnormal detectors adapted to changing operating situations [83]. Additionally, unsupervised learning models are typically less accurate than supervised learning models, and the user should still explain the results of the algorithm [23]. There are five main categories for unsupervised learning: outlier detection, data clustering, dimensionality reduction, hierarchical learning, and latent variable models [68]. The primary task in unsupervised learning involves analyzing data clusters formed based on their similarity. However, in AM, dataset sizes are often limited, restricting the application of the clustering analysis [24]. Wang et al. [25] used conventional optical images as input data for the autoencoder in an AM process. They implemented a clustering algorithm to identify the data group that yielded optimal results. The subsequent evaluation using a scoring system showed that the ML-based clustering method aligned effectively with conventional parameter optimization techniques, such as laser point distance, powder layer thickness, and laser scanning speed. Furthermore, an unsupervised ML model inherently possesses the ability to differentiate extraneous inputs within models and develop strategies to ensure uniform material

production under consistent conditions and quality benchmarks [66]. Likewise, unsupervised learning is useful for identifying cyber-physical attacks in AM processes [84].

2.2.2.1. K-means Clustering

The K-means clustering algorithm is a widely used unsupervised learning method for clustering challenges due to its simplicity and effectiveness. The algorithm involves setting up k centers that are assigned to a particular cluster [85]. While k-means operates as an unsupervised technique, selecting the number of clusters requires careful consideration to minimize the probability of generating inaccurate results. Furthermore, k-means encounter challenges when dealing with non-spherically dense data clusters [86]. Snell et al. [87] introduced a pore classification methodology that relied on k-means clustering for distinguishing gas pores, keyholes, and lack of fusion for L-PBF specimens. In that study, X-ray Computed Tomography (XCT) was employed to gather 3D pore data from L-PBF Ti-6Al-4V specimens. The CT-obtained radiographs were used to reconstruct 3D volumes with specific voxel sizes. The datasets were processed, segmented, and quantified using image processing methods, where the length, sphericity, and aspect ratio were employed as parameters for clustering 2664 pores. Optical Microscopy was applied to gather 2D pore data from 81 L-PBF Inconel 718 specimens through micrographs, utilizing the roundness and length measurements from a total of 21,955 pores as inputs for k-means clustering. Optical microscopy is a quick and cost-effective method for collecting data across numerous samples, making it an ideal choice for optimizing metal AM parameters. The results, partially illustrated in Fig. 12, indicate that the clustering of 3D pore data is more effective than the traditional limits-based approaches in classifying the pore types [87].

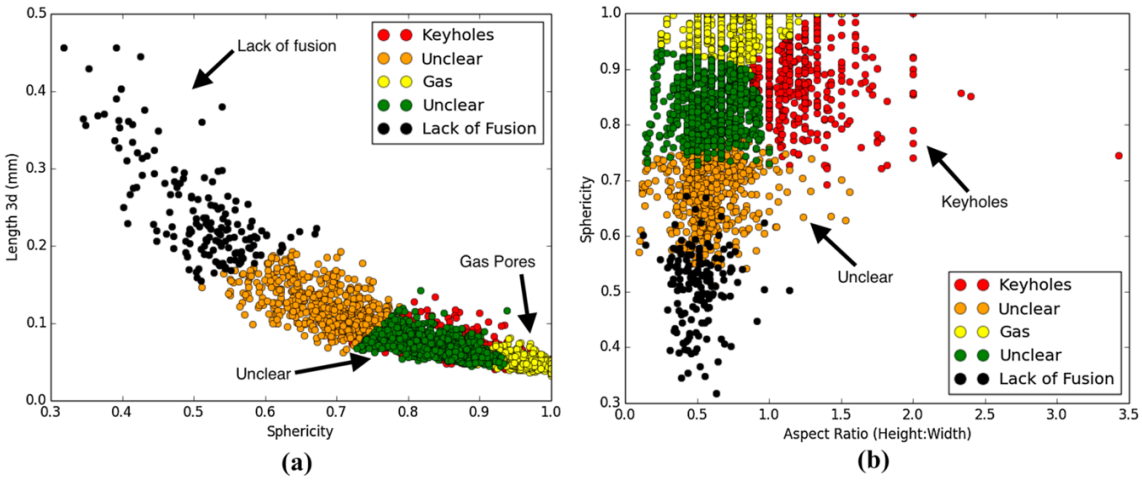

Fig. 12. Pore classification based on k-means clustering for L-PBF Ti-6Al-4V specimens. (a) pore length and sphericity. (b) Sphericity and vertical aspect ratio [87].

2.2.3. Semi-Supervised Learning

Semi-supervised models are used to overcome the limitations of both supervised and unsupervised ML models [88]. Semi-supervised learning is an ML approach that combines labeled and unlabeled data to train a model. By integrating the advantages of both

methodologies, semi-supervised models can achieve higher levels of accuracy and interpretability compared to supervised and unsupervised learning methods. Semi-supervised models can also be used to learn from unlabeled data, which is valuable when labeled data is scarce [89].

Labeled data from supervised learning methods can be used to initialize a model for unlabeled inputs, which may or may not have been previously labeled. Semi-supervised learning methods can be divided into two categories: transactive graph-based methods and inductive methods. Inductive methods use three subcategories to define how they use unlabeled data: Wrapper methods, unsupervised processing methods, and semi-supervised methods. Wrapper methods, such as self-training, co-training, and boosting, use unlabeled data to improve the performance of a supervised learning model. Unsupervised processing methods, such as feature extraction, cluster-then-label, and pre-training, use unlabeled data to extract features or learn a representation of the data that can be used to improve the performance of a supervised learning model. Semi-supervised methods, such as maximum-margin, perturbation-based, manifolds, and generative models, use unlabeled data to learn a model that is resistant to noise and outliers [90].

Although semi-supervised ML models have great practical value, they have been used less frequently in the AM field than in other fields. Okaro et al. [89] developed a Gaussian mixture model to automatically detect defects in AM products. They used a large photodiode dataset to extract key features and set up a monitoring system that included both in-situ and ex-situ labeling methods. The ex-situ data was labeled using ultimate tensile strength tests. A receiver operating characteristic (ROC) curve was calculated as the classification algorithm provides the probability of each data point association with a specific class. The analysis entailed evaluating the effectiveness of the classification algorithm by varying the 'threshold probability.' The semi-supervised model developed in the study was found to capture the benchmark results more closely than the supervised approach, as shown in Fig. 13.

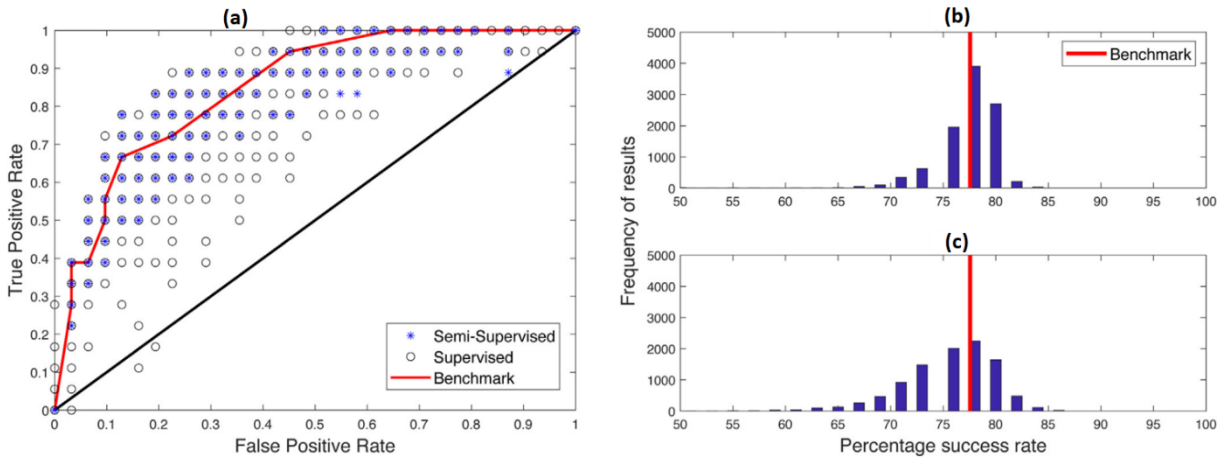

Fig. 13. The ROC curve of the machine learning models, along with the histogram of algorithm success rates for the (b) semi-supervised and (c) supervised [89].

2.2.4. Reinforcement Learning

Reinforcement learning is defined as "the process of acquiring a mapping from a given situation to corresponding actions to maximize a scalar reward or reinforcement signal" [91]. When the primary goal is to generate a prediction-based system, reinforcement learning is the best approach compared to other ML methods. The most crucial characteristic of this approach is its ability to acquire ways to lead to desired results using encouragement. The rewards motivate the learning process and influence the behavior of the algorithm [92,93]. This approach is occasionally referred to as the "environment-centric approach", which is an effective technique for enhancing automation and refining the efficiency of complex systems [94].

Wasmer et al. [95] established a quality monitoring system for L-PBF by incorporating reinforcement learning with acoustic data acquired from acoustic emission during printing. Their evaluation of classification accuracy for AISI 316L samples indicated the potential of their reinforcement learning-based approach for in-situ, real-time quality monitoring within L-PBF. In another study, Knaak et al. [96] introduced the application of reinforcement learning for predicting surface roughness in the L-PBF process, illustrated in Fig. 14. They implemented an advanced optical imaging system with an extended dynamic range combined with convolutional neural networks. The main benefit of this approach is its capacity to be incorporated into a control system for real-time surface optimization [96].

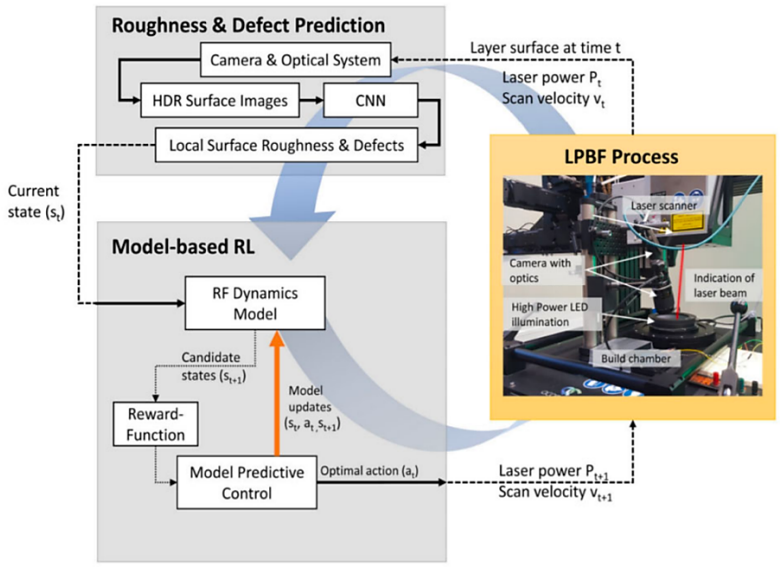

Fig. 14.Layer-wise Monitoring and Optimization Framework for L-PBF Processes Based on Reinforcement Learning Models[96].

2.3. Application of Machine learning in Additive Manufacturing

The interplay between process-structure-property relationships has been thoroughly examined and documented in multiple review articles [16,24,49,97]. The processing phase in the commonly used process-structure-property relationships has two distinct components: "processing parameters" and "processing resultant data". This division aims to differentiate between data existing before the manufacturing process and data created during the process [98]. These data types are employed for ML purposes in various AM aspects, including processing parameters optimization and property prediction, cost estimation, geometric deviation control, defect detection, and in-situ monitoring [24]. In the subsequent sections, each of these applications and their associated relationships will be explored.

Table 2 lists recent literature on metal AM that applies data-driven approaches, categorized based on the data acquisition method. This classification allows readers to become familiar with potential data sources, their applicability, and the features that can be detected or predicted by applying them. It can be seen in the table that the in-situ monitoring techniques, such as optical, thermal, X-ray imaging, and acoustic methods, are the most utilized data acquisition techniques. The techniques mentioned are used to observe general anomalies during the process [99] or specific phenomena like the detection of plume and spatter phenomena [100] and keyhole porosity [101,102]. This finding highlights the need for standardized protocols and robust quality assurance systems, including a closed-loop control system that comprehensively monitors and dynamically executes real-time modifications to the end product. This approach has the potential to broaden the application domain for additive manufacturing methods. For this purpose, researchers have utilized statistical techniques to examine different forms of in-situ data acquisition to identify process signatures and process windows. The analyzed data has been utilized to develop ML models to predict or identify the desired features.

Table 2. Literature on metal AM works applying data-driven approaches

Data acquisition method	AM technology	Data source	Alloy	Application	References
In-situ monitoring	L-PBF	High-speed thermal imaging	17-4 PH stainless steel [99], 304L stainless steel [103]	Anomaly quality prediction [99], detection of micropores [103]	–
		High-speed optical imaging	316L stainless steel	Prediction of plume and spatter phenomena [100], identification of local defects related to overheating [104]	–
		Synchrotron X-ray imaging	Ti6Al4V [101,102], AlSi10Mg, Inconel 625, CP1, 316L stainless steel, Aluminium [102]	Keyhole porosity detection [101,102]	–
		Optical tomography image	AlSi10Mg	Detection of local hot spots	[105]
		Thermographic imaging	H13 tool steel	Detection of geometrical shape, delamination, and splatter	[106]

Data acquisition method	AM technology	Data source	Alloy	Application	References
		Acoustic signal	Ti6Al4V, CM247- LC [107], 304L Stainless steel [108]	Prediction of porosity and surface imperfections [107], single track defects [108]	–
		High-resolution sensor imagery	GP-1 stainless steel	Detection of discontinuities, such as incomplete fusion, porosity, cracks, or inclusions	[109]
		Optical imaging	17–4 PH stainless steel [85,110], Ti6Al4V [85,111–114], 316L stainless steel [26,85,115], bronze alloy [85]	Defect prediction [110], prediction of porosity [112,114], powder bed anomalies [111], detection of single track width and continuity [26,115], identification of edge smoothness [113], process anomaly detection [85]	–
		Photodiode	Inconel 718 [116,117], AlSi10Mg [103]	Porosity detection [117], Fault detection, quality classification [116], detection of overhang defects [103]	–
	L-DED	Pyrometry	Ti6Al4V	layer-wise quality prediction [118], Porosity [119],	–
		Synchrotron X-ray imaging	Inconel 718	Prediction of track height, roughness, and melt pool geometry	[102]
		Acoustic signal	A mixture of Ti6Al4V with H13 tool steel	Detection of porosity and crack	[120]
		Melt pool thermal image	Ti6Al4V [75,119,121,122] [123], Sponge Ti powder [124], 316L stainless steel [125]	Porosity prediction [75,119,121,122,124], dilution estimation [125], surface distortion prediction [123]	–
		Point cloud processing	316L stainless steel	Identification of surface defects	[126]
Post-process characterization	L-PBF	High-speed camera	316L stainless steel	Determination of build quality	[127]
		Archimedes test	17-4 PH stainless steel [128], AlSi10Mg [129]	Prediction of porosity	[128,129]
		XCT experiment, 2D micrograph	Ti6Al4V [87,130], Inconel 718, Ti5553, Haynes 282 [87]	Identification of different pores [87,130]	
		Archimedes test, and surface roughness	Stainless steel 316L-Cu	Predicting part density and surface roughness in multi-material region	[131]
		Optical micrograph, first-principles	TiZrNbTa RHEA	Prediction of defects during in-situ alloying	[130]

Data acquisition method	AM technology	Data source	Alloy	Application	References
		calculations, and compression tests			
		Optical micrograph	316 L stainless steel, AlSi10Mg, Fe60Co15Ni15Cr10 MEA	Prediction of porosity	[132]
	L-DED	Optical micrograph	Al-5083 [133], 316L stainless steel [134], ER70S-6 mild steel [135], 1.5130 [136], Ti-10Fe [130]	Macro and micropores analysis [133], track depositing height [134], track geometry prediction [135], prediction of welding distortion [136], build height and grain size [130]	–
		Fatigue and XCT experiments	Ti6Al4V	Fatigue life prediction	[137]

2.3.1. Processing Parameters Optimization and Property Prediction

Ensuring part quality with specific processing parameters can be costly and time-consuming for designers. More specifically, the biggest challenge in the L-PBF process is the determination of the optimal process parameters that will results in a high-density and well-processes component. While experiments and simulations are helpful, they may not always be practical in cases with various input parameters. However, ML models efficiently establish the link between the process parameters and part quality, reducing costs and speeding up the optimization process [138]. Process parameter optimization is usually carried out when either innovative materials or a new approach needs to be processed by AM methods [139]. Process parameters can also be set as input features in ML methods to optimize the geometric variations for L-PBF components [20]. Several instances exist in the literature [140–144] where researchers have utilized various ML models and algorithms for optimizing process parameters. Among the ML models, ANNs have demonstrated superior efficacy for process parameter optimization [145]. Reddy et al. [97] developed an ANN model to predict the volume fraction of α phase for various Ti alloys produced via the DED method followed by different heat treatments. The ANN model used in this study had two hidden layers, each consisting of six neurons representing Al, V, Fe, O, N, and heat treatment temperature for the input layer, and two neurons representing α and β phase volume fractions for the output layer. The model was trained over 18,000 iterations with hyperparameters set at a learning rate of 0.7. The comparison between experimental and model prediction results can be observed in Fig. 15.

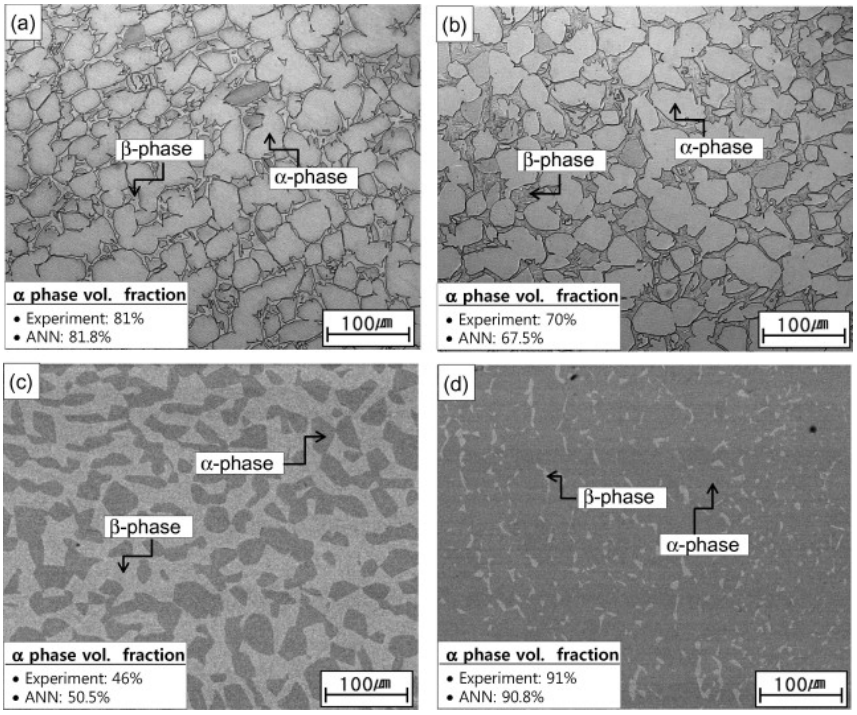

Fig. 15.Comparison between experimental data and ANN predictions for the quenching process of a Ti–6.3Al–4.1V–0.21Fe–0.17–0.005N alloy at four different temperatures: (a) 700 °C, (b) 815 °C, (c) 900 °C, and (d) for a Ti–6.85Al–1.6V–0.13Fe–0.17–0.001N alloy quenching[146].

Silbernagel et al. [147] used ML techniques to optimize process parameters for L-PBF of pure copper using optical imagery. Data in the form of images was gathered and subsequently fine-tuned through ML methodologies. In this case, as shown in Fig. 16, the results indicate that the most favourable track outcomes were achieved across all layer thickness variations using a point distance of 50 μm and laser scan speeds of 250 mm/s or higher.

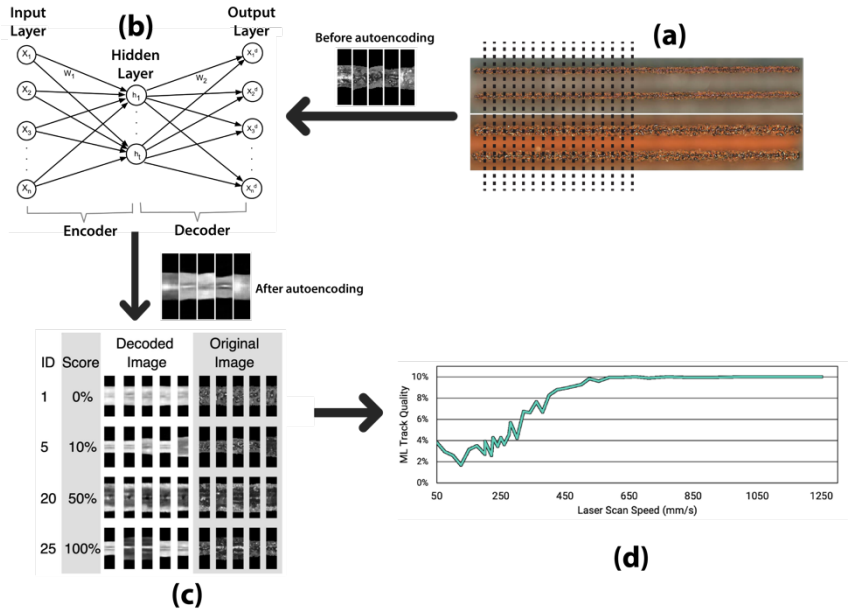

Fig. 16. The procedure of ML methodology adopted by Silbernagel et al. [147]. (a) Pairs of 18 mm long full scan track images of thin walls [147]. (b) Using the CNN algorithm with an AE [148] for decreasing the high-dimensional image data into a simplified reconstructed output, (c) selection of the top 20 images from clusters

which were evaluated and scored between 0 (clusters which showed signs of balling or an unstable melt pool) and 100 (clusters where the images demonstrated high-quality weld tracks), and (d) ML track quality for different laser scan speeds [147].

ML methods have also been used to predict the mechanical behaviour of AM products, including tensile properties [149–152], fatigue behaviour [153–156], and microhardness [157–160]. In a research by Maleki et al. [149], the process parameters were optimized, and the mechanical properties of Ti6Al4V were improved using a Neural Network model (see Fig. 17). The research indicated that scanning speed, laser power, and hatch spacing have the most notable effect on the tensile strength, as shown in Fig. 18.

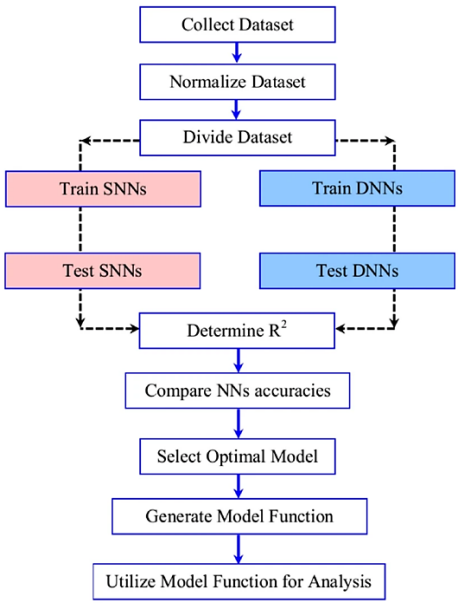

Fig. 17.The flowchart of the procedure of the research done by Maleki et al[149].

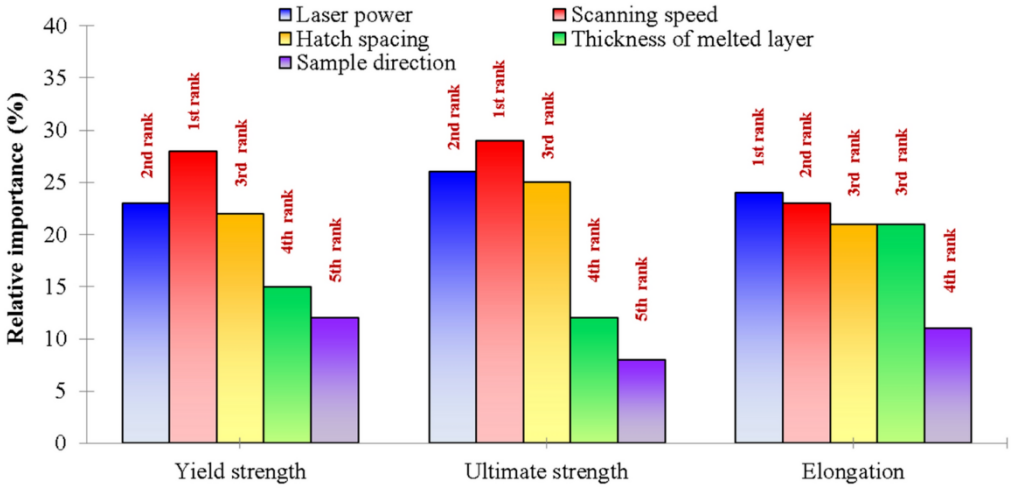

Fig. 18. Effects of the various tensile process parameters on the properties of L-PBF fabricated Ti-6Al-4V [149].

Moon et al. employed a drop-out neural network (DONN) [155] to predict the fatigue behavior of Ti–6Al–4V L-PBF-produced samples. The model features consisted of stress, surface roughness (R_a, R_t, R_{iso}, $\bar{r}$), pore density, diameter, compactness, sphericity, and projected YZ area for 41, 35, and 76 data points, with the predicted target being log cycles to failure. Due to the limited amount of data, the leave-one-out cross-validation method was employed. One data point was reserved for testing, while the remaining data was used for training. This process

was iterated through for all the data. Predictions and the experimental values can be observed in pair plots depicted in Fig. 19, where M and AB refer to two samples with different surface features.

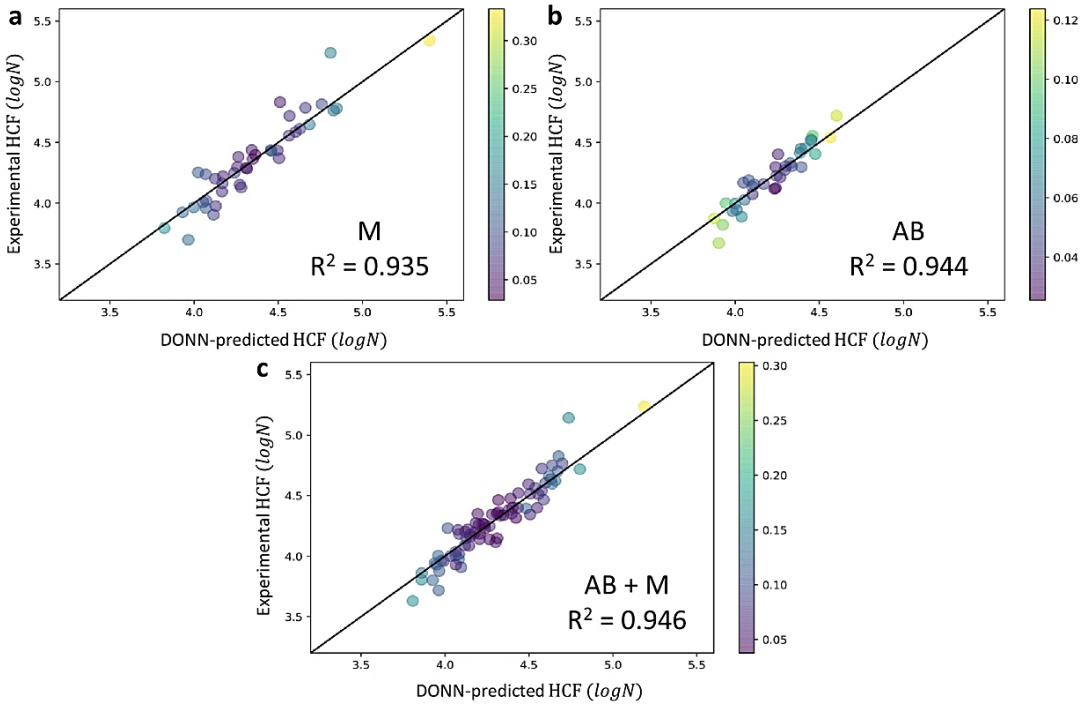

Fig. 19 Comparing DONN predictions with experimental high-cycle fatigue (HCF) in logN for (a) AB, (b) M, and (c) combined AB+M samples. The uncertainties are displayed in different colours [155].

The fatigue behavior of metallic materials is mainly influenced by their surface characteristics, such as roughness, porosity, and defects, thus necessitating their consideration in metal AM products for cyclic loading applications. Therefore, the surface quality of the metal AM components needs to be enhanced so the products are widely adopted in delicate applications like medical components. Zhang et al. [161] presented an ANN algorithm to model and interpolate the complex, nonlinear relationship between different parameters and the targeted surface roughness and porosity of L-PBF Ti-6Al-4V samples. The training dataset, which consists of 35 samples, was obtained from DEM simulations (refer to Fig. 20). This approach enabled the creation of a process map, which helped to determine the optimal process parameters to achieve the desired surface roughness with a prediction accuracy of over 97%. Consequently, this method led to time savings during the printing process and reductions in the overall manufacturing cost. Additionally, Kumar et al. [162] worked on predicting the surface roughness of components produced by DED using KNN modeling. The predictive model demonstrated a prediction error of 2.8% for powder-based DED and 2.3% for wire-based DED.

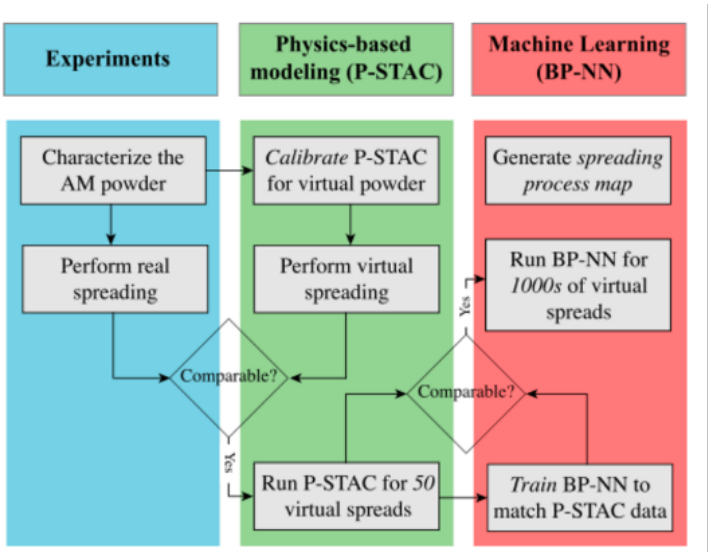

Fig. 20. The collaborative integration of experimental work, physics-based DEM simulations, and ML techniques [161].

Aside from the surface features, microstructure has also been of interest to the researchers. Cao et al. [163] used the Generative Adversarial Network (GAN) model to quantitatively predict alpha phase morphology in additively manufactured Ti-6Al-4V specimens. Due to its efficient handling of image datasets, the GAN model is a promising option for exploring the relationships between microstructure and manufacturing processes. Fig. 21 shows that the GAN model is trained to analyze and learn the complex details of the needle's physical structure, including its shape and size. Once the model has gathered sufficient data, it can reconstruct the predicted microstructure morphology in a visually understandable form, as depicted in Fig. 21.

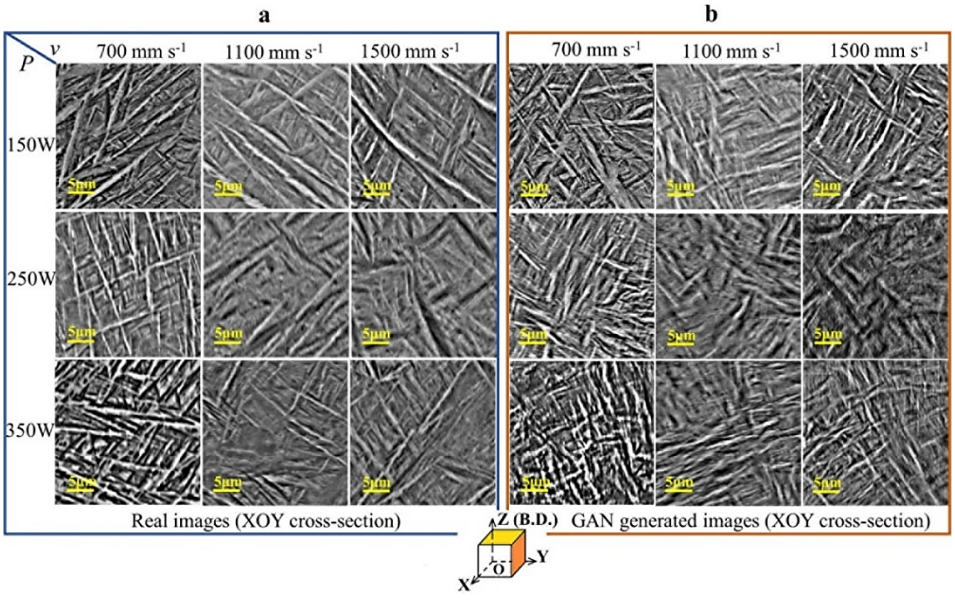

Fig. 21. XOY cross-sections of L-PBF fabricated Ti-6Al-4V; (a) real micrographs and (b) micrographs produced by GAN [163].

Yao et al. [115] conducted a study using an ML-based processing parameter optimization approach to identify the proper sets of processing parameters, resulting in a superior synergy of strength and ductility in L-PBF. As shown in Fig. 22, the formation and morphology of α' phases and the resultant properties (Fig. 22c) were investigated by considering the influence of

L-PBF process parameters and heat treatment influence (Fig. 22a) as the ML model features. Moreover, the researchers used the partial dependence plots generated by the ML models (see Fig. 22b) to determine that the maximum ductility may be achieved at P/V=0.1 (J/mm), and the hatching distance was determined through experimentations.

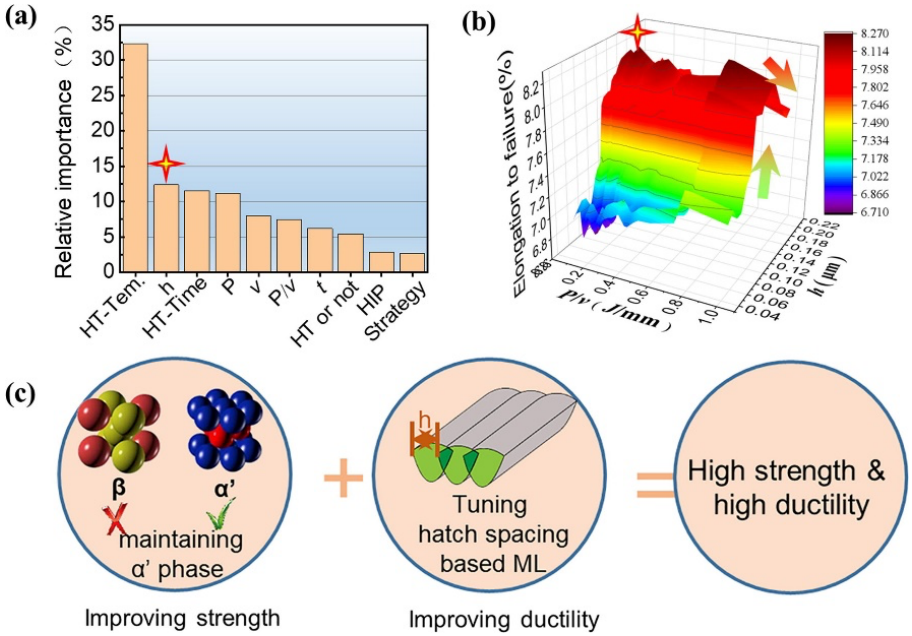

Fig. 22. (a) The relative importance of different features that affect ductility in L-PBF-produced Ti64 alloys, as calculated using machine learning. (b) The 3D contour map, and (c) a schematic illustrating the design concept for simultaneously enhancing both strength and ductility in the studied sample [115].

2.3.2. Geometric Deviation Control

Frequently encountered issues with AM components include low geometric precision and suboptimal surface quality [164]. These challenges hinder the widespread adoption of AM in different industries, such as the aerospace and medical sectors [165]. To address this issue, ML models can identify geometric imperfections, quantify the degree of deviation, and suggest solutions to improve these issues. For example, Francis et al. [123] developed a framework that compensates for geometric errors in the L-PBF process using a CNN model. The ML model, after being trained, could predict distortions by considering thermal data and a set of process variables. This ultimately generated an error detection and correction outcome within the CAD model. According to reports, this method improved the geometric precision of objects produced with the adjusted CAD model. In this case study, the authors utilized the CAMP-BD approach, which is a combination of a CNN and ANN, designed to predict results by analyzing extensive datasets. As shown in Fig. 23, the input information comprises the tensor structure of the thermal history and the processing/designing parameters. At the same time, the deep learning model predicts which set of data corresponds to the output data, specifically distortion.

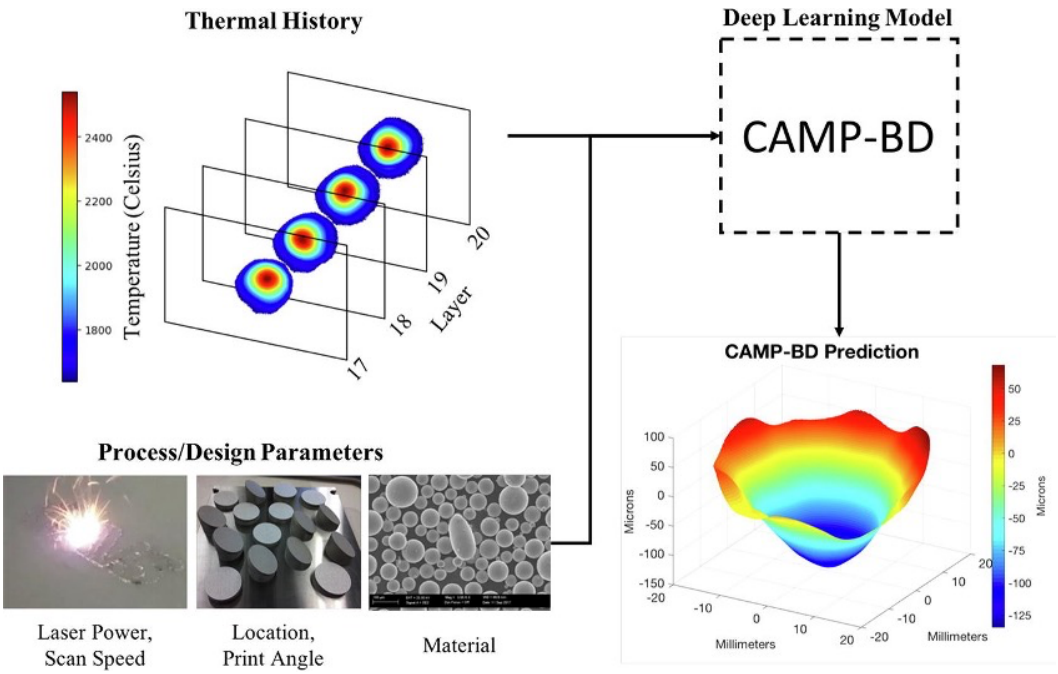

Fig. 23. Illustration of the procedure of geometric error compensation proposed for Ti-6Al-4V in L-PBF using CAMP-BD [123].

Zhu et al. [166] used the CNN method in the L-PBF Process to predict geometric deviation in AM parts. They employed Ansys Additive as an AM simulation software to generate the deviation data. Three processing parameters, part size, and a multi-channel model were used to predict deviation profiles on a 2D layer with a deviation field consisting of three channels as input. The convolution and pooling operations were performed at two stages, forming the suggested network. To overcome the problem of the limited dataset, they used Statistical Shape Analysis to increase the data and generate new samples.

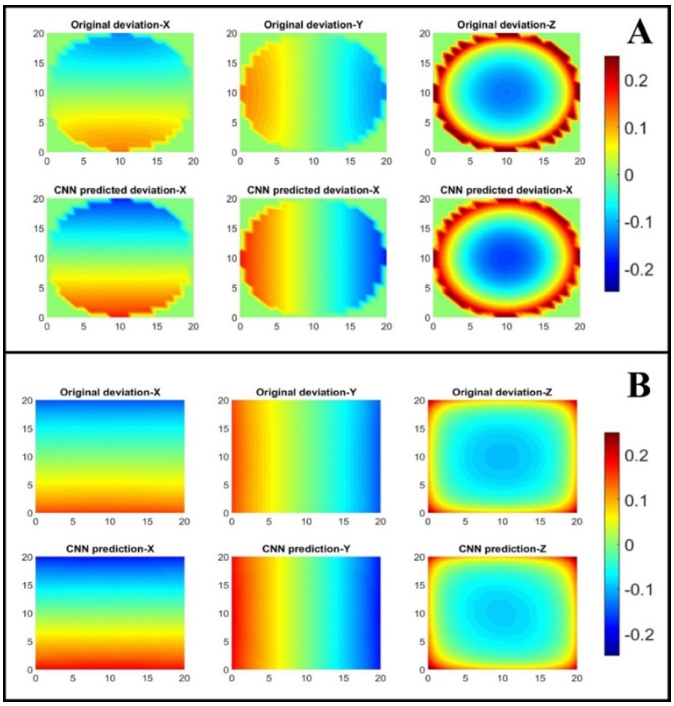

Fig. 24. Comparative analysis of the original deviation profile and the CNN prediction for (A) cylindrical shape and (B) square shape [166].

2.3.3. Defect Detection and In-situ Moniotoring

The accuracy of human visual inspection is subject to errors and irregularities; nonetheless, the accurate detection of errors is highly prioritised in the AM process. Regarding defect detection issues, a crucial first step towards achieving in-process quality assurance is establishing a correlation between process conditions and defects [71,167]. Table 2 lists some case studies that focus on the application of ML in AM for defect detection. For instance, Gobert et al. [168] captured layer-wise images of the AM process during L-PBF. The images illustrated in Fig. 25 were subsequently utilized as input data for computed tomography scans to identify defects. The input data consisted of layer-wise images captured under varying lighting conditions. The main objective of the ML algorithm was to accurately classify whether each layer displayed any anomalies or not.

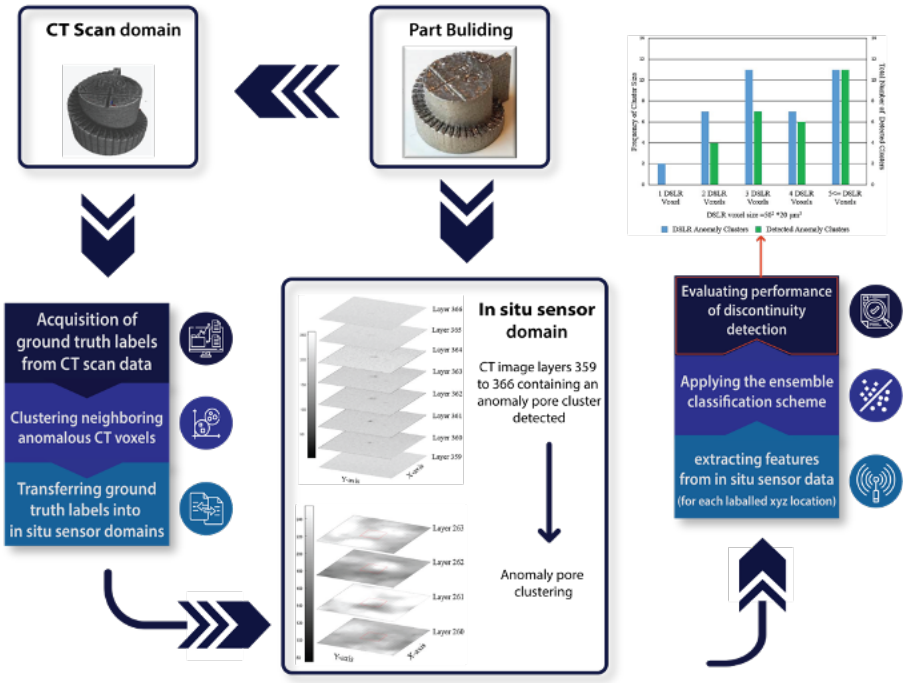

Fig. 25. Schematic of the procedure proposed by Gobert et al. [168]. The left side of the illustration depicts anomaly extraction from CT scans, while In-situ sensor imagery is shown at the center. Feature extraction, supervised machine learning, and performance assessment are also depicted on the right.

In a previous study, Ye et al. [169] presented a layer-wise monitoring framework for quality control of AM using in-situ point cloud fusion (Fig. 26). Their approach maximized the advantages of 3D scanning for direct monitoring, resulting in a more accurate assessment of morphological changes. The results showed an improved ability to identify small changes that can impact the overall quality of the component.

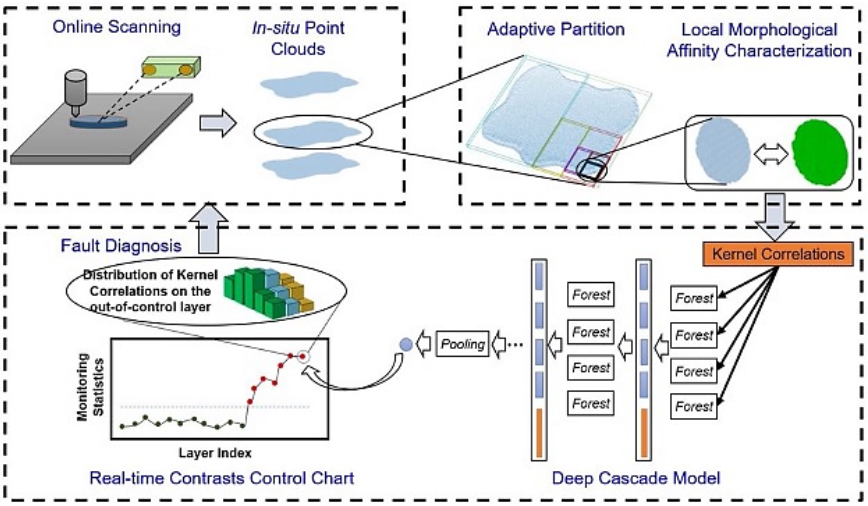

Fig. 26. The schematic of the framework of the selected methodology in the study by Ye et al. [169].

Early detection of defect formation can be facilitated by integrating in-situ monitoring with unsupervised learning techniques. Scime et al. [85] applied unsupervised learning techniques for anomaly detection within the powder layer of the L-PBF process. As illustrated in Fig. 27, they used images of powder beds as input for their ML model, intending to classify various anomalies that could lead to irregularities in powder spreading. Filters generate different responses depending on the distribution of images. Pixel responses are recorded as vectors and clustered using the k-means algorithm. Each cluster is defined by an average response vector known as "visual words". Filter response vectors are compared to the closest visual word in the dictionary. The fingerprint of each training image patch is recorded in a tabular format. Results from the three patch-type analyses, along with CAD data, are integrated using context-driven heuristics to classify anomalies for individual pixels in the powder bed image.

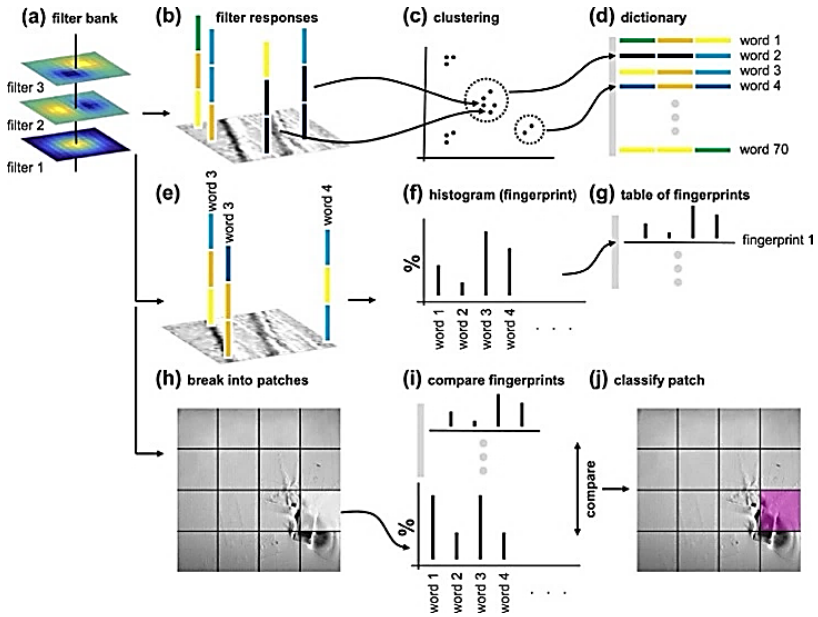

Fig. 27. Schematic of ML procedure applied in the case study proposed by Scime et al. [85] for in-situ monitoring and analysis of powder bed images.

Surface anomaly identification has gained significant interest in minimizing the need for expensive post-processing work due to the uneven and rough surface finish characteristic of

DED-printed components. Kaji et al. [170] employed DBSCAN (Density-based spatial clustering of applications with noise) and RAND-LA net to detect surface anomalies in a powder feed DED system, achieving a prediction accuracy of 93%. A laser line scanner was used to acquire 2D surface profiles from the DED-built part surface to create a 3D point cloud. The validation results, shown in Fig. 28, indicate the model struggles to recognize concave surfaces. This is because these surfaces are global features, that are difficult to detect using the DBSCAN clustering algorithm and the RandLA-Net model.

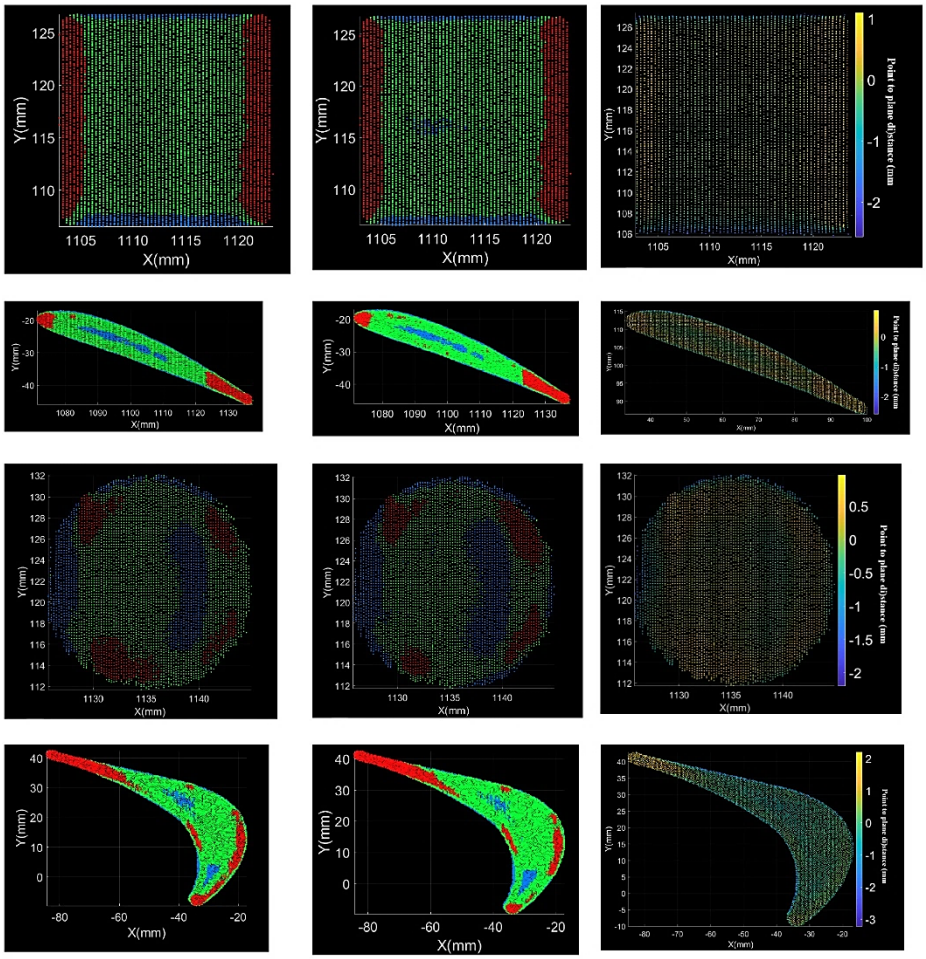

Fig. 28 Comparison of RandLA-Net prediction with Ground Truth (GT). The colors depict different surface types: red for convex, blue for concave, and green for normal surfaces [170].

Gaikwad et al. [171] used the L-PBF process to create a ML model that examines the quality of a single track printed with Stainless Steel 316L powder. The Sequential Decision Analysis Neural Network (SeDANN) algorithm was used for this purpose. The input data was gathered by pyrometer and high-speed video camera. The model analyzed the effects of printing parameters, such as laser power and velocity, on the quality of the single track. The study found that the SeDANN algorithm had higher accuracy than other ML models in detecting balling, lack of fusion, conduction, and keyhole during the process monitoring.

Du Plessis [172], examined the effect of process parameters on the formation of defects in L-PBF Ti6Al4V. The results showed that while higher scanning speeds offered a safer processing window for avoiding pore formation, the possibility of keyhole formation increased with increasing laser power. Understanding the interactions between lasers and materials as well as the dynamics of melt pools, is crucial in reducing the formation of defects such as keyhole pores. Laser absorption as a result of keyhole formation was investigated by Jiang et al. [173] using a deep learning method, while Synchrotron X-ray imaging was used to generate input data for the ML models. The authors reported a mean absolute error of less than 3.3% [173]. Similarly, Gorgannejad et al. [174] used X-ray imaging to train data fusion machine learning models for predicting the localized evolution behavior of keyhole pores. The authors also utilized thermally induced optical emission measured using both off-axis and coaxial photodiode sensors, as well as acoustic emission. According to heavily featured models, it was observed that the prediction results depended largely on the acoustic monitoring signal, with a secondary contribution from the optical emission sensors.

3. Materials and methods

3.1. Sample Modeling

The samples were manufactured using the Prima Additive 250, 3D printer. The Computer-Aided Design (CAD) files were created, and the construction process was carried out in the IAM Center of Politecnico. The operations commenced with the production of the CAD file, resulting in the creation of 64 cubes for each task. Fig. 29 displays the exact measurements of the samples.

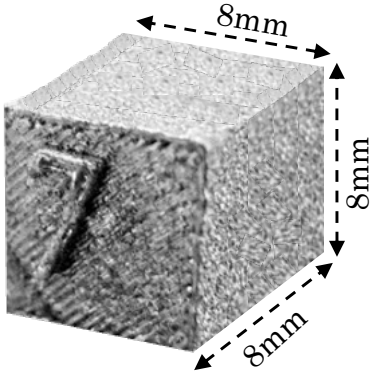

Fig. 29. Nominal dimension of the cubic samples.

The software Materialise Magics was used to input the pre-selected process parameter settings for each component. It is crucial to acknowledge that every component was allocated a specific laser speed, laser power, and hatch distance, leading to unique features for each component once it was printed.

3.1.1. Design of experiment

The Design of Experiment (DoE) includes all the factors used at this experience. Before starting a work in the PBF process, several parameters can be modified. These parameters are the necessary machine settings needed to manufacture a component using powders. To simplify matters, these process parameters are divided into four groups inculding laser-related, scan-related, powder-related, and temperature-related parameters.The laser-related characteristics encompass laser power, wavelength, spot size, pulse duration, and pulse frequency. Scan-related characteristics encompass the velocity at which scanning occurs, the interval between each scan (also known as hatching distance), and the specific pattern used for scanning. The factors connected to powder include particle size and distribution, particle shape, powder bed density, layer thickness, and material qualities. The temperature-related characteristics include the temperature of the powder bed, the temperature of the powder feeder, and the uniformity of temperature [175].

The selection of appropriate process parameters is crucial as the ultimate quality of the product depend on them. It is crucial to emphasize the interplay between these characteristics, as altering one parameter can sometimes yield the same outcome as altering other characteristics of the end product. In general, it is necessary to maintain a balance between all criteria. Indeed, achieving this objective is the ultimate goal of this thesis research. While all process parameters influence the final product, their impact varies depending on specific material characteristics.. The layers that have been demonstrated to have greater influence are parameters like thickness, laser power, laser spot size, scanning speed, and hatching distance are important factors to consider. The concept of Volumetric Energy Density (VED) was first established in references [176,177] to Attain substantial significance by comparing the different sets of parameters.

$$VED = \frac{P}{v.h.l} \quad (1)$$

Where:

VED= Volumetric energy density $[\frac{J}{mm^3}]$

P= Laser power $[\frac{J}{s}]$

v=Scanning speed $[\frac{mm}{s}]$

h= Hatching distance [mm]

l= Layer thickness [mm]

VED stands for Volumetric Energy Density, which quantifies the energy that impacts a volume of 1 cubic millimeter in the powder bed. Subsequently, it will be utilized as a benchmark to enhance the efficiency of the procedure.

The EP Hatch Prima Industrie's program program was used to provide these process parameters, resulting in the generation of a CAM file. Table 3 displays the calculated VED and the process parameters that were given to the software to generate the CAM file. Each sample has its particular process parameters. Subsequently, using Prima Industrie's program, the STL file was sliced. Subsequently, this file serves as the input for the PrintSharp 250 machine. Fig. 30 illustrates the design of 64 components, with their respective CAM files being visible.

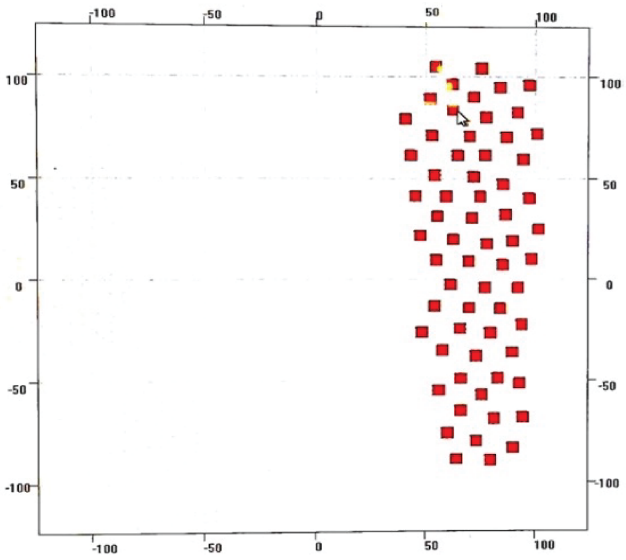

Fig. 30.Illustrartion of he CAM model depicts the positioning of the 64 components on the platform.

Table 3. Process parameters for each of 64 samples.

s. ID	Power [w]	Scanspeed [mm/s]	Hatch Distance [mm]	VED [J/mm^3]	s. ID	Power [w]	Scanspeed [mm/s]	Hatch Distance [mm]	VED [J/mm^3]
1	190	400	0.1	158	**33**	190	400	0.12	132
2	190	600	0.1	106	**34**	190	600	0.12	88
3	190	800	0.1	79	**35**	190	800	0.12	66
4	190	1000	0.1	63	**36**	190	1000	0.12	53
5	200	400	0.1	167	**37**	200	400	0.12	139
6	200	600	0.1	111	**38**	200	600	0.12	93
7	200	800	0.1	83	**39**	200	800	0.12	69
8	200	1000	0.1	67	**40**	200	1000	0.12	56
9	270	400	0.1	225	**41**	270	400	0.12	188
10	270	600	0.1	150	**42**	270	600	0.12	125
11	270	800	0.1	113	**43**	270	800	0.12	94
12	270	1000	0.1	90	**44**	270	1000	0.12	75
13	340	400	01	283	**45**	340	400	0.12	236
14	340	600	0.1	189	**46**	340	600	0.12	157
15	340	800	0.1	142	**47**	340	800	0.12	118
16	340	1000	0.1	113	**48**	340	1000	0.12	94
17	190	400	0.11	144	**49**	190	400	0.13	122
18	190	600	0.11	96	**50**	190	600	0.13	81
19	190	800	0.11	72	**51**	190	800	0.13	61
20	190	1000	0.11	58	**52**	190	1000	0.13	49
21	200	400	0.11	152	**53**	200	400	0.13	128
22	200	600	0.11	101	**54**	200	600	0.13	85
23	200	800	0.11	76	**55**	200	800	0.13	64
24	200	1000	0.11	205	**56**	200	1000	0.13	51
25	270	400	0.11	136	**57**	270	400	0.13	173
26	270	600	0.11	102	**58**	270	600	0.13	115
27	270	800	0.11	82	**59**	270	800	0.13	87
28	270	1000	0.11	258	**60**	270	1000	0.13	69
29	340	400	0.11	172	**61**	340	400	0.13	218
30	340	600	0.11	129	**62**	340	600	0.13	145
31	340	800	0.11	103	**63**	340	800	0.13	109
32	340	1000	0.11	158	**64**	340	1000	0.13	87

After producing the 64 cubic samples for a more thorough examination of VED, process parameters, and porosity formation, seven additional components were sourced from other studies [178] to explore the relationship between porosity and mechanical properties, as detailed in Table 4.

Table 4. process parameters of the seven extra samples collected from other studies[178].

s. ID	Power [W]	Scan speed [mm/s]	Hatch Distance [mm]	VED [J/mm^3]
1	100	1000	0,1	33
2	200	1000	0,2	33
3	100	800	0,1	42
4	150	1000	0,12	42
5	200	800	0,2	42
6	270	1000	0,2	45
7	190	1000	0,13	49

3.2. Samples Building

The samples were produced using the PrintSharp 250 (Fig. 31), which is a Powder Bed Fusion machine designed for medium-volume applications. It is specifically intended for the industrial manufacture of intricate components. This machine is well-suited for companies providing Additive Manufacturing services and prototype purposes. It offers a great level of flexibility when it comes to managing parts. The technical features of the machine are documented in Table 5.

Fig. 31. Prima Additive Print Sharp 250

Table 5. The technical parameters of the PrintSharp 250

Category	Specification
Dimensions (LxWxH)	3500 (L)- 1100 (W)- 2450 (H) mm
Weight	2000 kg
Power Supply	380 V/50 Hz/8kW
Type of laser	Yb (Ytterbium) Fiber Glass
Laser Power	200 W/ 500 W (Optional)
Laser Focus Diameter	70 – 100 µm
Beam Wavelength	1060 – 1080 nm
Building Volume	250 x 250 x 300 mm
Beam Deflection Speed	8 m/s
Positioning Speed	10 m/s
Build rate	12 – 30 cm^3/h
Layer Thickness	0.02 – 0.1 mm
Layer Width	0.1 mm (single line width)
Recoater Specs	Travel: 650 mm
Building Platform z-axis	Travel: 300 mm/Speed max : 6 mm/s/Res: 0.01 mm
Heating Platform	Up to 200°C
Monitoring of O_2 Level	Below 100 ppm
Permissible Room Temperature	15 – 30°C
Gas (Consumption – running/filling)	7 l/min (running)
System Fill Consumption	20 l/min (up to filling)
Cam Software	Materialise Magics
Control & Other Software	Eplus control software (EPC)
Industrial Interfaces	Ethernet

Originally, the 3D printer was loaded with the prepared CAM file, followed by the preparation of the corresponding powder. The feedstock material consisted of AISI316L stainless steel gas atomized powder, provided by Oerlikon, and gas atomized copper powder from Sandvik Osprey Ltd. A mixture of copper and stainless steel particles was blended in a ball mill with minimal energy input for a duration of 16 hours, without the use of any balls. The concentration of copper in the combination powder was 2.5 weight percent. Fig. 32 displays the morphology and related Energy Dispersive X-ray Spectroscopy (EDS) elemental maps of the initial powder mixture. The powder distribution analysis reveals that the average particle diameter of the blended AISI316 and Cu is 27 µm, with specific values of 13 µm for d10, 23 µm for d50, and 40 µm for d90. Similarly, the average particle diameter of Cu is 6.3 µm, with specific values of 3.1 µm for d10, 5.3 µm for d50, and 13.1 µm for d90. Table 6. displays the chemical composition of the Cu-containing AISI316L stainless steel powder utilized in this study, as determined by EDS.

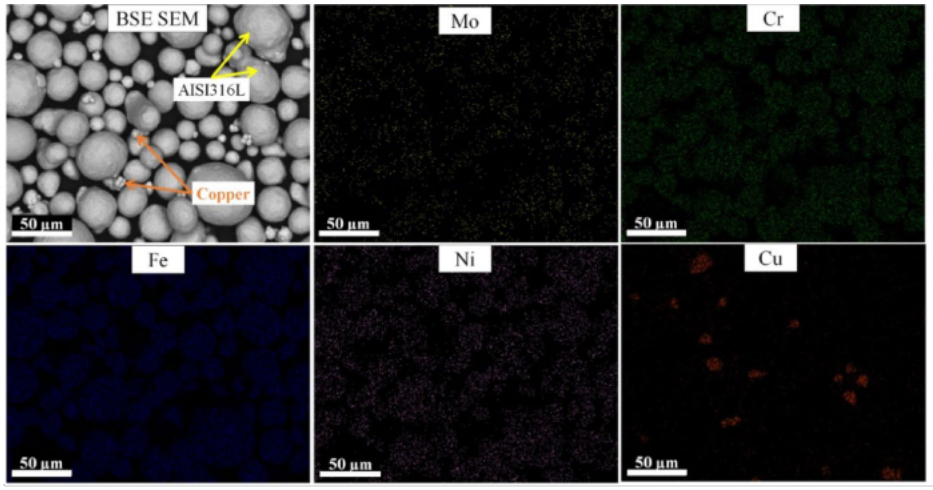

Fig. 32. Scanning electron microscope (SEM) image of a mixture of powders. It is accompanied by elemental maps obtained using EDS [179].

Before commencing the printing process, the build chamber was thoroughly emptied to a residual oxygen level of less than 0.1%. High-purity Argon was used to preserve an inert atmosphere within the construction chamber and minimize the likelihood of oxidation. A scanning approach was employed using a bidirectional stripe scanning pattern with a 67° rotation between each succeeding layer. The height of each layer was 30 µm. Subsequently, the components were cut from the construction platform [179].

Table 6. The chemical composition of the combined AISI316L-Cu powder was determined both nominally and by analysis.

Elements	Cr	Ni	Mo	C	Mn	Cu	P
Nominal (wt%)	17-19	13-15	2.25-3	0.03	2.0	2.5	25
Analysed (wt%)	17.02	13.5	2.04	0.02	2.11	2.92	22

In Fig. 33, the highlighted section illustrates the laser in operation during the LPBF process. The laser accurately melts a small layer of metal powder to create the desired shape. The process of melting is fundamental to LPBF, as it enables the fabrication of intricate and highly accurate metal parts through the sequential deposition of layers. Fig. 33 illustrates the samples positioned on the building platform after the completion of the building process. After completing the construction, every job was removed from the workspace and cleaned. Subsequently, a focus assessment was carried out. Ultimately, the samples were obtained from the plate employing Wire Electrical Discharge Machine (EDM). Furthermore, the samples were labeled with a numerical value to signify their distinct process parameters. The x-axis corresponds to the recoater's orientation, while the z-direction aligns with the building direction.

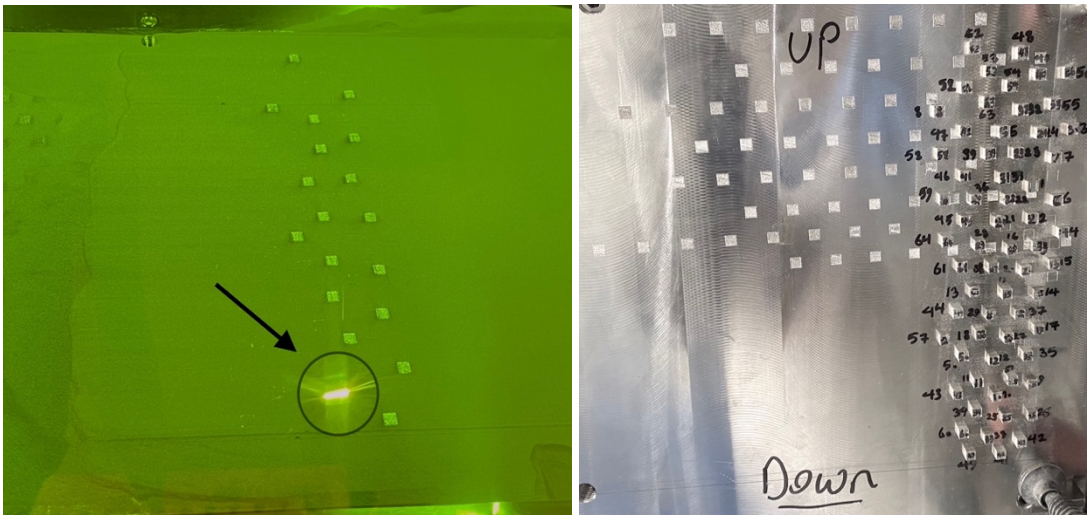

(a) (b)

Fig. 33. (a)The platform during job running (b) Result after completion of 3D printing.

3.3. Sample characterization

During this stage, activities involved using a wire-cutting machine to separate the pieces from the platform. Subsequently, the density of the components was determined utilizing the Archimedes method. After conducting density measurements, certain components were chosen for tomography analysis, which was then performed on them. Furthermore, following the tomography procedure, some samples were selected for metallography. Subsequently, the microstructure of these samples was analyzed using an optical microscope (OM). The experiments took place in the IAM laboratory.

3.3.1. Cutting Machine

The wire-cutting machine functions by employing a slender wire that is electrically charged to meticulously sever metal with the highest accuracy. The method operates by generating electrical discharges between the wire and the workpiece, resulting in the gradual removal of material along the cutting trajectory. The sparks as can be seen in Fig. 34 are produced rapidly and efficiently, resulting in the removal of small quantities of metal and the desired shape of the workpiece. Throughout the cutting procedure, a constant flow of deionized water is employed to cool both the wire and the workpiece, thereby preventing excessive heat and removing the eroded particles. This water also functions as a dielectric medium, a crucial requirement for the occurrence of the electrical discharge process. The words "time on" and "time off" relate to the length of the electrical pulses (on-time) and the gaps between them (off-time), respectively. The parameter "t_{on}" regulates the energy and length of each spark, which directly impacts the cutting speed and surface quality. On the other hand, "t_{off}" enables a brief cooling period, minimizing the potential for thermal damage and enhancing the accuracy of the cutting process. These parameters are essential for maximizing the cutting efficiency and ensuring the high quality of the end product [180].

Fig. 34.Illustration of electrical sparks and the movement of water during the wire-cutting procedure.

The G.cut WEDM machine was utilized to cut the samples at this particular stage. This machine is shown in Fig. 35. Section 1 corresponds to the software of the cutting machine, where the settings for wire movement, the auto process, and the start and stop buttons for cutting are managed. Section 2 displays the X, Y, and Z coordinate directions, which assist in ensuring the cutting is performed in the correct direction. Section 3 is the main part of the machine, where the workpiece is placed, and the cutting operation is carried out. At first, the platform was attached to the wire-cutting machine using clamps. Next, in the software that deals with locating the wire in the cutting machine, the wire was placed on the platform to establish the reference point for both the x and y coordinates. Subsequently, the wire's location was adjusted according to the platform's parameters, and the appropriate dimensions and correct orientation were loaded into the machine to commence the cutting operation. Following the conclusion of this stage, the severed components were separated and prepared for further procedures, which was determining their density by the utilization of the Archimedes approach.

Fig. 35.Key components of the WEDM machine: Section 1 (software controls), Section 2 (coordinate display), and Section 3 (cutting area).

3.3.2. Archimedes density

The Archimedes approach is employed to determine the relative densities of components produced by SLM [181]. This method involves weighing a single sample in two distinct fluids Typically, the fluid used for reference is air. The second fluid consists of distilled water, acetone, or ethanol. While distilled water is frequently utilized [182], it may only sometimes be appropriate due to the potential formation of air bubbles on the surface of the sample. This phenomenon occurs in lattice systems, such as when air bubbles hinder the complete penetration of water into the interior of the mesh due to the high surface tension of the water[183].

The Archimedes density measuring method, according to the ASTM F3637-23 [184], enables the calculation of total porosity. Firstly, the measurement chamber is prepared, and the beaker is filled with distilled water, with a density of 0.997 $\frac{g}{cm^3}$. Subsequently, the device underwent calibration, and the dry weight (W_{dry}) of the sample was measured, as depicted in Figure 6(part 1). The dry weight was determined in part 1 of Fig. 36 , and noted from the digital measurement shown in part 3. Upon finishing this procedure, the device was reset to a value of zero, and the sample was positioned in slot 2 to be fully immersed in distilled water. All the bubbles that had formed were eliminated, and the sample was completely submerged in the water. The weight at this point was documented as $W_{immersion}$. Subsequently, the sample was extracted from the water and promptly reweighed at position 1 in Fig. 36 to determine the amount of water that had been absorbed during immersion. This phase resulted in obtaining the wet weight, indicated as W_{wet} . Furthermore, the theoretical density of the powder was determined to be 7.985 $\frac{g}{cm^3}$ using the relative technique. This method considers that the powder consists of 2.5% copper and 97.5% AISI316. Subsequently, the total porosity percentage and relative density percentage for all samples were computed utilizing the given formulas.

$$\rho_{Archimedes} = \rho_{liquid} \times \frac{w_{dry}}{w_{dry} - w_{immersion}} \quad (2)$$

$$\rho_{Geometrical} = \rho_{liquid} \times \frac{w_{dry}}{w_{wet} - w_{immersion}} \quad (3)$$

$$\text{Total porosity percntage} = \frac{\rho_{teorethical} - \rho_{bulk}}{\rho_{teorethical}} \times 100\% \quad (4)$$

$$\text{Relative Density percntage} = \frac{\rho_{Archimedes}}{\rho_{teorethical}} \times 100\% \quad (5)$$

Where: :

$\rho_{Archimedes}$ = Archimedes density (apparent density) $[\frac{g}{cm^3}]$

$\rho_{Geometrical}$ = Geometrical density (bulk density) $[\frac{g}{cm^3}]$

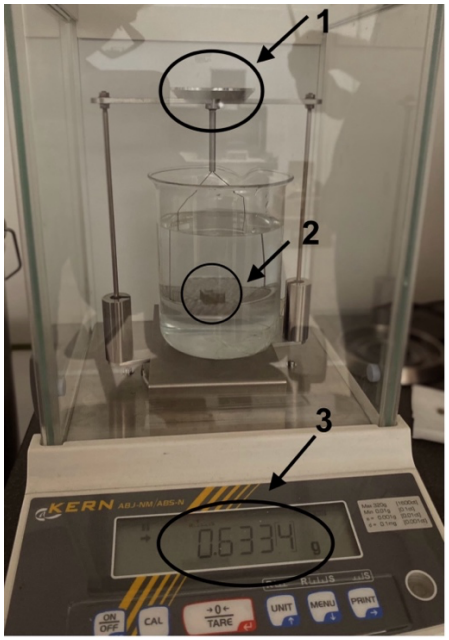

Fig. 36. The measurement setup for Archimedes' density is 1) a position for measuring the dry and wet weight, 2) a place for measuring the immersion weight, and 3) a digital display for showing the weight values.

3.3.3. X-ray computed tomography

X-ray computed tomography employs algorithms to construct 3-D representations by combining many X-ray images taken around a rotational axis. Over time, three primary XCT techniques have been developed, each enhancing the speed of data collection. The

initial XCT method acquires density data along each pencil beam of X-rays that is linearly displaced in the opposite direction of an X-ray detector. A small increment rotates the scanner, and this process is repeated until a full 360° of data is acquired. The second technique employs a two-dimensional array of X-rays that covers the entire object's width, along with a one-dimensional array of detectors positioned at the edges of the X-ray fan beam. The third approach employs a two-dimensional detector with a complete three-dimensional X-ray cone. The x-ray source and detector of the pencil beam scanner move in a straight line to scan a slice of the xy plane. The source and detector undergo slight movements in the z-axis for the item being measured, and this process is repeated. The fan beam scanner exposes an entire slice of the object simultaneously, whereas the cone beam scanner exposes the entire thing. To capture the entirety of the item, each scanning method undergoes a full rotation of 360°[186]. Fig. 37. shows each XCT approach. XCT evaluations focus on image quality, notably resolution and contrast. The maximum magnification of XCT images decreases with object size due to X-ray penetration, reducing resolution. Reducing magnification increases scan voxels and reduces image clarity. Low X-ray penetration makes measuring high-density materials difficult, limiting object size. This is because reliable contrast requires more prolonged exposures. Instead of scanning the whole object, XCT scanners measure a particular section or use a reference coupon with similar features. This improves image quality. This technique may increase scan quality but not capture the object of interest, which may skew the results.

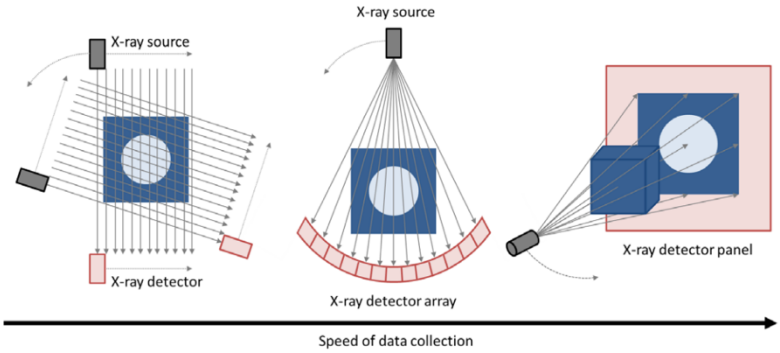

Fig. 37. Pencil, fan, and cone beam XCT schematics. The fan beam image shows a curved detector, whereas the cone beam image shows a flat panel detector. Both can be employed in each case[6].

Eleven samples were chosen for XCT analysis using specific range of veds.The samples underwent tomographic analysis to ascertain their porosity, which would be compared with alternative methodologies. In addition, comprehensive data were obtained on porosity distribution, the geometries of porosities, their diameters, and other relevant features, which will be further elaborated in the findings section. The sample was initially positioned on the holder, as depicted in Fig. 38(a). In section (b) of Fig. 38, a copper filter was positioned in front of the X-ray gun. The monitor detector is depicted in section (c). The sample's position was verified and corrected using the device's related software, as shown in Fig. 39, to guarantee that the sample stayed within the X-ray imaging frame. Once the correct

placement was confirmed, the tomography process began. Before introducing a new sample for tomography, it is imperative to eliminate any remaining residue by uniformly resetting the detector using X-rays.

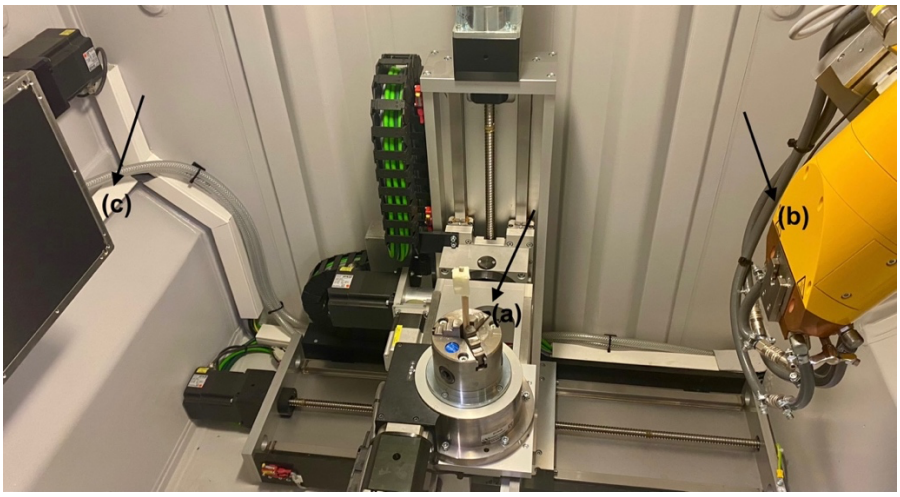

Fig. 38. (a) sample holder for tomography analysis,(b) X-ray beam gun, and (c) Detector configuration for accurate tomography analysis.

Fig. 39. The software checks and alters the sample's position during tomography analysis to keep it in the X-ray imaging frame.

3.3.4. Metallography (Grinding, polishing, and etching)

Following the completion of tomography on many samples, some of them were determined using the acquired data, and these particular samples were then selected for metallography. Given the small size of the samples, it was necessary to mount them to assist in the subsequent grinding and polishing procedures. For the initial mounting stage, acrylic resin KMU and methyl methacrylate hardener were employed, as depicted in Fig. 40(a). The samples were

placed in the mount frame in the specified orientation. A mixture consisting of a 2:1 ratio of resin to hardener was made by thoroughly mixing for a duration of one minute. Subsequently, the mixture was put into the mounting mold. After 15 minutes, the mounted samples were extracted from the mold, as depicted in Fig. 40(b). At this point, the samples underwent preparation for the processes of grinding and polishing.

(a) (b)

Fig. 40. (a)The acrylic resin and methyl methacrylate hardener were used for mounting the samples before the grinding and polishing process. (b) Mounted samples were removed from the mold, ready for the grinding and polishing process.

The process of grinding and polishing was conducted using a Presi machine, as seen in Fig. 41(a).At first, abrasive papers with grit sizes of P480, P600, P800, P1200, and P2400 were chosen for grinding as can be seen in Fig. 41 (b). The grinding process commenced using the most abrasive paper, and the chosen paper was dampened before being placed on the machine. Then, the machine was activated and a rotational speed of 150 rpm was established for this step. For the procedure to be successful, water is necessary to carry away the particles that are being abraded and to maintain a low temperature throughout the operation. Thus, the water flow was located in the center which is controlled via a dial. At this step, it became feasible to commence the procedure. Subsequently, the sample can be positioned on the abrasive paper is used to grind the surface in a manner that achieves the necessary level of abrasion. Following each grinding repetition, the material was scrutinized under a microscope to verify the visibility of the grinding lines. Assuming that the lines were distinct, the sample was rotated by 90 degrees, and a more refined abrasive paper was employed to eliminate the existing lines and generate new ones. The process was repeated until the final grinding stage using the P2400 paper was finished.

(a) (b)

Fig. 41. (a)The Presi machine was used for the grinding and polishing of the samples.(b)The selection of abrasive papers (P480, P600, P800, P1200, and P2400) used for grinding the samples.

After the grinding stage, the samples underwent polishing to eliminate the scratches caused by the preceding procedures. Polishing pads with grit sizes of 1 microns and 3 microns were utilized, as depicted in Fig. 42. A 1-micron pink pad was positioned on the device, and diamond suspension, together with a lubricant, as depicted in Fig. 43 (a), was utilized to attain a polished surface. Subsequently, the surface was further refined using the 3-micron blue polishing pad and a 0.3-micron aluminum oxide solution, as shown in Fig. 43(b).

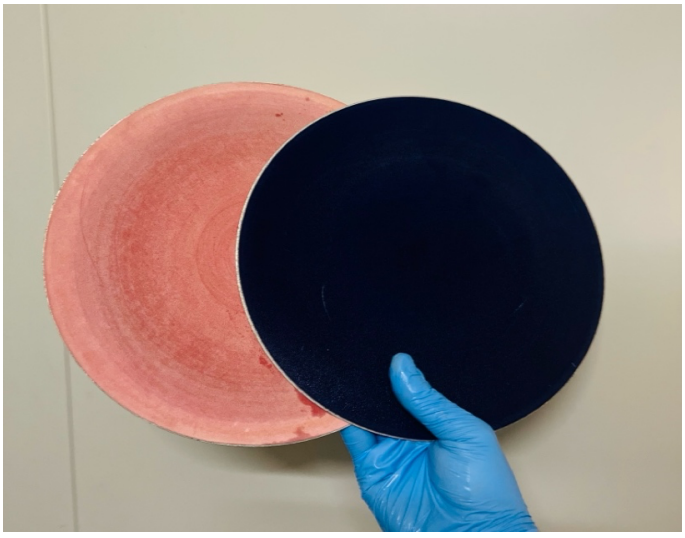

Fig. 42. Polishing pads with 1-micron (pink) and 3-micron (blue) grit sizes were used for polishing the samples.

(a) (b)

Fig. 43. (a) Diamond suspension and lubricant used during the polishing process with the 1-micron pink pad. (b) 0.3-micron aluminum oxide solution used during the polishing process with the 3-micron blue pad during the polishing process.

After finishing this stage, it was anticipated that the sample surfaces would exhibit a high degree of smoothness and reflectivity, resembling a mirror, as depicted in Fig. 44. At this point, the samples were prepared for the subsequent phase, where the microstructure was investigated using an OM.

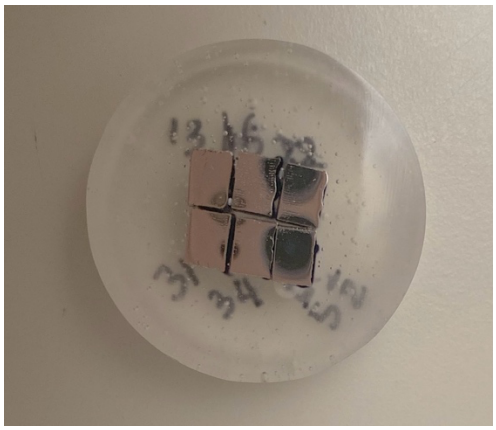

Fig. 44. The final appearance of the samples after grinding and polishing, with a smooth, mirror-like surface, ready for microstructural examination under OM.

To investigate the austenite microstructure of the samples and examine the melt pools created under different process parameters, the mounted and polished samples, depicted In Fig. 44, underwent etching. The etching procedure employed 100 mL of Kalling's No. 2 solution, as demonstrated in Fig. 45 Initially, the samples were submerged in the solution for 20 seconds and carefully rotated. They were then rinsed with water to eliminate any residual etchant, and the surfaces were dried. The samples were subsequently analyzed using an optical microscope to observe the melt pools.

Fig. 45. Kalling's No. 2 solution (100 mL) was used to etch the samples to reveal melt pool structures.

3.3.5. Optical Microscope

The surface of the samples were studied using an optical microscope after being polished. The investigation utilized a "LEICA" optical microscope (Fig. 46 (a)) with a manual x-y stage and objectives that offered magnification options ranging from 5x to 100x. Imaging was conducted using a black-and-white camera that was calibrated. In addition, the microscope is equipped with software that offers sophisticated image processing capabilities. The samples were placed on a specialized plane with the surface to be examined facing downward (Fig. 46 (b)). The surface study was performed using an optical microscope set at a magnification of 5x and 10x. The sample was manipulated using the adjustment knobs in order to acquire comprehensive photos of the complete surface of each sample. The microscope's focus was meticulously calibrated for each photograph to guarantee optimal sharpness and of the surface pores. The photos depict black dots on the background, which symbolize the porosities found within the material's section. Images of every section of the sample are captured in a matrix format. The optical microscope enables the acquisition of pictures at different levels of detail.

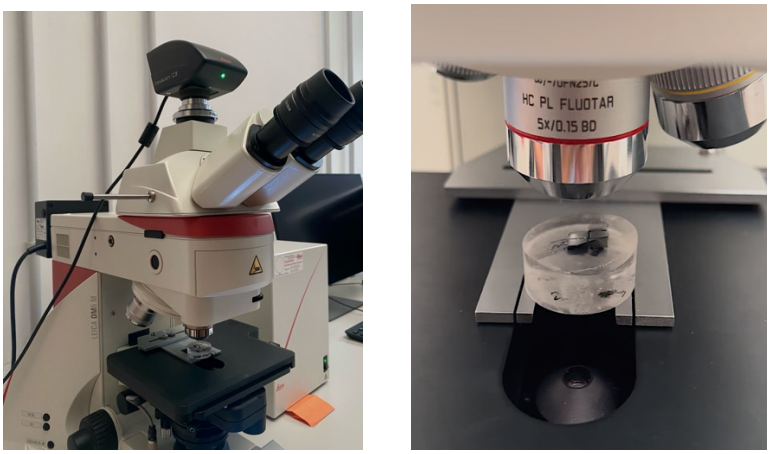

(a) (b)

Fig. 46. An optical microscope was used to take high-resolution images of metallographically prepared and numbered samples. (b)The sample is placed in a down position for analysis using an optical microscope.

3.3.6. Image Analysis

Following the acquisition of the photos, they engaged in post-processing with the software known as ImageJ. ImageJ is a Java-based software that was developed by the National Institutes of Health in the United States for processing and analyzing images. The porosity percentage of the samples was examined using the ImageJ software, as demonstrated in Table 7 as an example of one of the samples that has a porosity percentage of 2.329%. To do a porosity analysis, ImageJ requires an image that contains 8 bits. Consequently, the first step consisted of converting the image into an 8-bit format, which ultimately led to the creation of a grayscale representation in which the color of each pixel is determined by the intensity of the greyscale. The software made it easier to quantify the proportion of pores on the surfaces as well as the diameters of the pores. By adjusting the threshold to get rid of any distortions that were caused by polishing and any scratches that were still present, it became possible to exactly measure the percentage of darkened regions that corresponded to the pores in the samples (Fig. 47).

Table 7.Analysis of sample porosity using ImageJ software, demonstrating the quantification process of porosity within the sample.

	Area	Mean	StdDev	Mode	Min	Max	Median	%Area	MinThr	MaxThr
1	16708.651	255	0	255	255	255	255	2.329	255	255

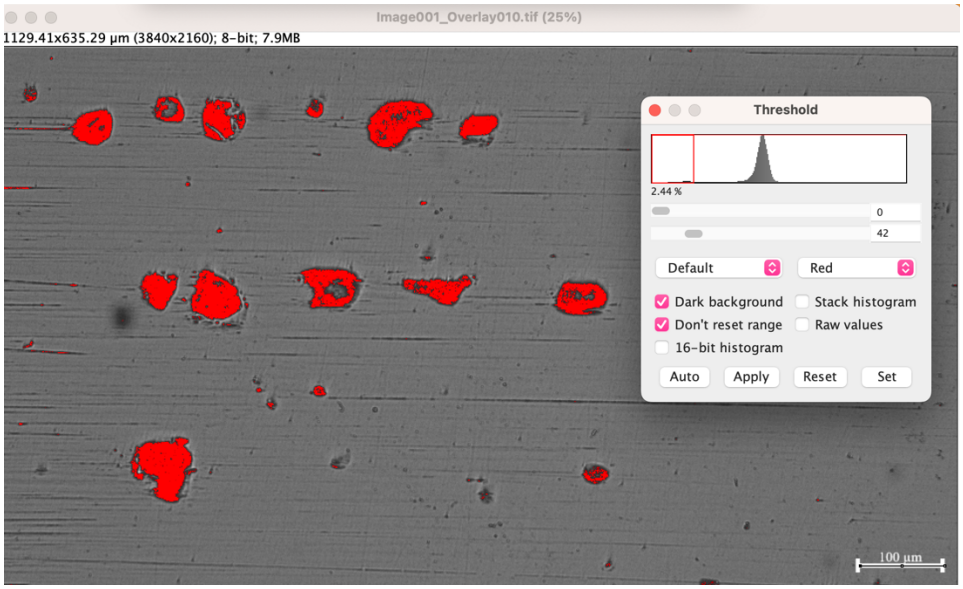

Fig. 47. The grayscale image was processed in ImageJ using thresholding to enhance and measure the pores (shown in red), while excluding any polishing errors and scratches.

3.3.7. Mechanical tests

After the initial 3D printing of cubic samples and the analysis of the correlation between their process parameters and porosity, an additional nine components were manufactured further to investigate the influence of porosity on mechanical properties. The nine components were meticulously chosen according to prior process parameters to exemplify high, medium, and low porosity levels. Tensile test specimens were fabricated from these printed components, featuring exact gauge dimensions of 10 mm in length, 2.5 mm in width, and 3 mm in thickness. Tensile testing was conducted using a universal Instron-5982 testing system at ambient temperature, employing a strain rate of 1×10^{-3} s^{-1}. Each sample underwent triplicate testing to guarantee consistency and repeatability of results.

Following the tensile tests, the fracture surfaces of the specimens were carefully analyzed utilizing scanning electron microscopy (SEM) in secondary electron imaging mode. This analysis offered insights into fracture behavior, facilitating a detailed examination of ductile and brittle fracture characteristics at various porosity levels. The study correlates porosity with fracture morphology, providing essential data on how different porosity levels affect mechanical performance, which is vital for optimizing process parameters in AM.

3.4. Evaluation of ML algorithms

Applying a regression model typically requires multiple metrics for a comprehensive evaluation [187]. The accuracy of the chosen models is assessed using three statistical metrics:

the coefficient of determination (R^2), the mean absolute error (MAE), mean square error (MSE).

The MAE represents the average absolute deviation for each statistic which is an indication of prediction accuracy[188]. MAE provides a more accurate representation of the actual amount of the prediction error, in contrast to other error metrics, by properly addressing the issue of error cancellation[189]. It should be noted that the MAE value is expressed in the same units as the original target variable. This feature facilitates comparisons among multiple machine learning models, specifically for the target data, rather than across different prediction tasks[187].

The Mean Square Error (MSE) denotes the sample standard deviation of the discrepancies between predicted and actual values, used as a metric that calculates the ratio between the squared differences of predicted and actual values, and the total number of data points. It is worth noting that the MSE is more sensitive to outliers compared to the MAE [189,190].

The coefficient of determination, often denoted as R^2, measures the strength of the relationship between two variables. It assesses the accuracy of the regression equation in fitting the observed data and capturing the variability in the dependent variable. Specifically, R^2 quantifies the level of the variation in the target variable that can be assigned to the changes in independent input variables in a regression model. Essentially, it signifies the degree of correlation between the input and target variables[72]. It is essential to note that assessing prediction accuracy by using only R^2, especially in non-linear regression, is inadequate. Therefore, in this study, R^2 is not the exclusive statistic for assessing model performance. Additionally, R^2 has certain limitations. Although, the increase of independent variables results in a rise in R^2, especially in large datasets, a very high value of R^2 may indicate an overfitted model, while an accurate model may have a reduced R^2. Negative R^2 values also indicate that predictions are worse than the mean target value[187]. MAE, MSE, and R^2 can be calculated by equations below.

$$\mathrm{MAE} = \frac{1}{n}\sum_{i=1}^{n}|y_i - \hat{y}_i| \tag{6}$$

$$MSE = \frac{1}{n}\sum_{i=1}^{n}(y_i - \hat{y}_i)^2 \tag{7}$$

$$\mathbf{R^2} = \frac{\sum_{i=1}^{n}(\hat{\boldsymbol{y}}_i - \bar{\boldsymbol{y}})^2}{\sum_{i=1}^{n}(\boldsymbol{y}_i - \bar{\boldsymbol{y}})^2} \tag{8}$$

Where y_i, $\hat{y}_i$, $\bar{y}$ represent actual, predicted, and mean values, respectively, and n is total number of data points. The high R^2 value and the low MAE and MSE values suggest that the analysis and statistical model are accurately representative[191].

To address the above-mentioned limitations and have a comprehensive analysis of algorithms accuracy, the Index of Merit (IM) is introduced in this study. As shown in equation (9) IM integrates the three statistical measures (MAE, MSE, and R^2) into a single metric that provides

a more holistic view of model accuracy. A value closer to zero indicates optimal predictive performance, whereas values further from zero suggest decreasing accuracy [192,193].

$$\text{IM} = \sqrt{(MAE)^2 + MSE + (1 - R^2)^2} \tag{9}$$

4. Result and Discussion

4.1. Overview

This section highlights the outcomes derived from the measurement methods outlined in the preceding chapter. Fig. 48 presents a comprehensive illustration of the complete workflow, illustrating the utilization of ML models to analyze the data and optimize the process parameters by finding a relation between them and defect content. In the final stages, the influence of process parameters on the microstructure was thoroughly analyzed. Subsequently, mechanical properties were measured to establish the relationship between porosity and mechanical performance.

Fig. 48 depicts the overall organization of the tasks carried out, with the first three sections related to the methodology detailed in the preceding chapter. These sections are essential as they provide the basis for the work done in this chapter. The following sections of the figure describe the procedures undertaken to process the data, test the models, and conduct a comprehensive analysis of the critical parameters. The data under study includes measured relative density percentages obtained through three distinct methodologies: Archimedes density measurement, image analysis, and X-ray computed tomography. These three methodologies were selected to guarantee an efficient and comprehensive dataset. Subsequently, Density data was split into training and test sets, a conventional procedure in ML for assessing model performance. In Fig. 48, the letter "i" denotes that the data partitioning into training and test sets took place in several phases, employing different sets. For instance, the data were partitioned using an 80/20 split, allocating 80% for training and 20% for testing. The focus has now transitioned to evaluating the effects of various model hyperparameters. The impact of these hyperparameters on model performance was analyzed through specific plots, which are discussed later in this chapter. Three evaluated hyperparameters exhibited the most substantial influence and were selected for a detailed analysis. To guarantee a comprehensive analysis, the impacts of these critical parameters were assessed using a large dataset. Their impact on the R^2 value (a metric of model precision) was evaluated. As the R^2 value nears 1, the model's efficacy seems to enhance, signifying that the predictions closely correspond with the actual data. Following identifying the optimal two hyperparameters, the influence of a third parameter was investigated. This analysis utilized 2D plots to assess errors through multiple metrics. The error plots facilitated the identification of the optimal range for the third parameter, which, similar to the preceding hyperparameters, was chosen based on the maximum R^2 value achieved. Following the completion of hyperparameter tuning, attention shifted to the prediction phase. During this phase, two-dimensional graphs were used to compare the model's predicted values with the measured values. Subsequently, regression analysis was employed to evaluate the accuracy of the model's predictions about actual outcomes. This comparison is essential, as it offers a final assessment of the model's accuracy and the accuracy of the predictions. After the prediction phase, a critical evaluation was performed to ascertain if the training size had attained 90%. If it had not, the entire process was started again with a new training and test data division. Upon reaching the 90% training size, the workflow advanced to the final stage, during which the optimal model and its associated hyperparameters were chosen.

This chapter subsequently discusses a variety of ML models in detail. Upon reaching the specified training size, the outcomes of these models, including their optimal parameters and performance, are documented.

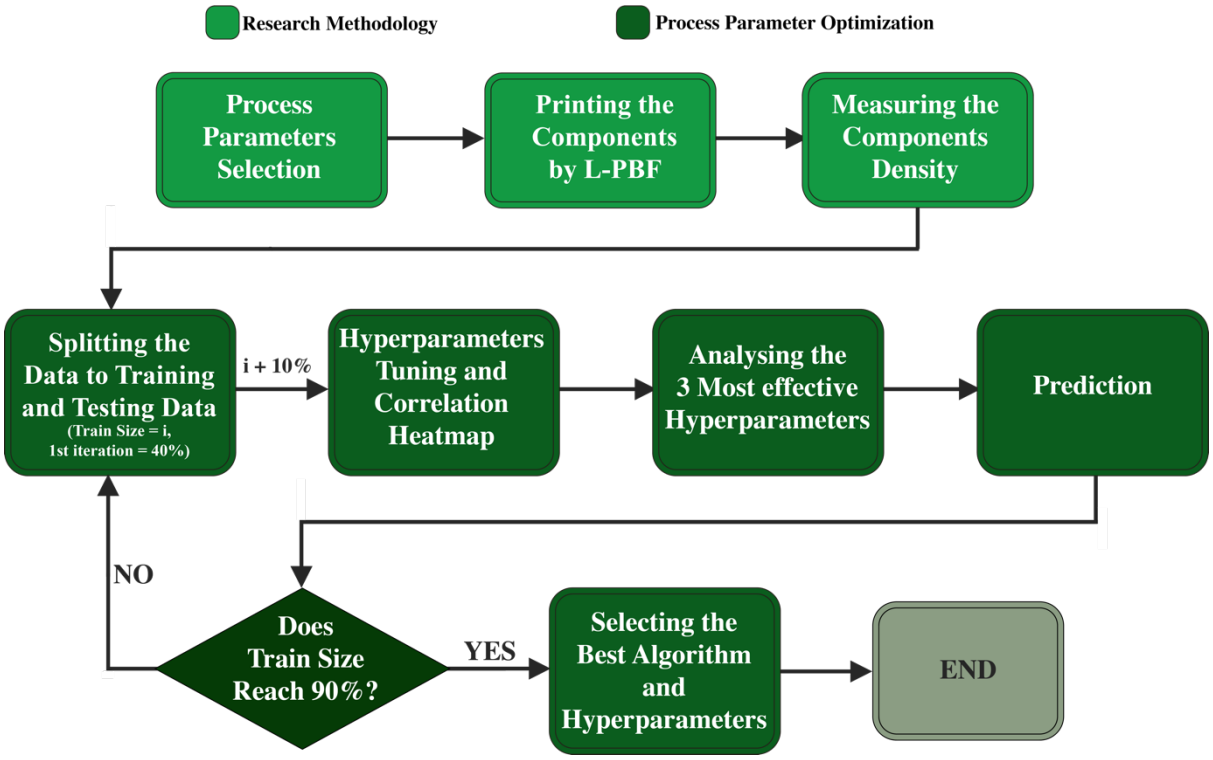

Fig. 48.An overview of the workflow is provided in this chapter, demonstrating the use of machine learning models to analyze data and optimize process parameters by finding a relationship between them and defect content. The initial three sections pertain to the approach, whereas the subsequent sections outline the process parameter optimization.

4.2. Data preprocessing

All data acquired from the second part has been compiled at this stage. Table 8 presents the relative density percentages measured for each of the 64 samples. Furthermore, for a specific subset of chosen samples, the densities were assessed using two alternative methods, as detailed in Table 8. This table additionally displays the porosity percentages for the samples. Upon gathering data from the three methodologies, the averages were computed to facilitate the implementation of diverse ML models such as Bayesian Regression, Decision Tree Regression (DT), Gradient Boosting Regression (GBR), Gaussian Process Regression (GPR), K-Nearest Neighbors (KNN), Support Vector Regression (SVR), and Random Forest Regression (RFR) on the average density. The primary objective is to enhance the process parameters according

to these models. The tomography and metallography methods were not conducted on all 64 specimens. The average values of 13 pieces were initially computed, and subsequently, these averages were extrapolated to the remaining pieces. This methodology guarantees a thorough analysis while considering the data constraints of specific techniques. The data was divided into training and test sets. The total number of these portions equals 100%. Multiple machine learning models were utilized on up to 90% of the training data, and the ideal ratio of training to test data was subsequently determined. The analyses and conclusions are presented based on these chosen ratios. This precise data splitting and model setup procedure ensures that the models' performance is both powerful and reliable, resulting in important insights into optimizing process parameters. The findings of these analyses, including optimal arrangements for training and testing data, are detailed, providing the precise selection of the most appropriate machine learning models for the dataset.

Table 8.Relative density percentages measured for 64 samples.

Sample ID	Relative Density[%]	Sample ID	Relative Density [%]
1	96.89	33	96.11
2	98.27	34	98.80
3	98.46	35	99.93
4	99.69	36	99.15
5	99.03	37	96.33
6	97.68	38	98.30
7	98.90	39	99.56
8	98.24	40	98.87
9	97.87	41	97.94
10	97.38	42	98.25
11	98.69	43	97.81
12	98.79	44	97.64
13	96.40	45	96.38
14	97.74	46	97.05
15	98.03	47	98.51
16	97.27	48	97.60
17	96.36	49	95.89
18	96.44	50	97.42
19	98.57	51	98.52
20	98.48	52	99.09
21	96.47	53	97.88
22	97.74	54	98.31
23	98.10	55	99.53
24	99.48	56	98.55
25	96.16	57	96.99
26	98.58	58	98.19
27	97.77	59	98.51
28	98.80	60	98.89
29	96.86	61	95.95
30	97.90	62	97.92
31	99.33	63	97.66
32	98.08	64	97.28

The results from the metallography and tomography techniques, as illustrated in Table 9, were determined by images obtained by optical microscopy and Tomography analysis. The optical microscope images were subsequently analyzed using ImageJ software. The porosity percentages were determined via image analysis of the tomographic data. This detailed analysis confirmed a thorough examination of the samples' surface and volumetric characteristics, providing significant insights into the materials' internal structure. Advanced imaging techniques and software facilitated a more precise assessment of porosity, thereby improving the overall accuracy of the data and its significance to the study.

Table 9.Porosity percentages for selected samples using two additional methods (metallography and X-ray

Sample ID	Porosity content by XCT [%]	Porosity content by image analysis [%]	Porosity content by Archimedes Density analysis[%]
5	0.99	-	0.97
7	1.09	-	1.10
9	4.72	-	2.13
13	4.55	1.99	3.60
16	2.52	7.58	2.73
18	3.11	2.82	3.56
21	3.26	2.41	3.53
22	0,90	1.37	2.26
23	1.26	1.38	1.90
31	2.24	2.11	0.67
34	1.11	1.24	1.20
39	1.43	-	0,44
52	0.96	0.94	0.91

A selection of samples was made for additional analysis to investigate the correlation between tomography and metallography data. The density percentage for each sample was determined using two distinct methodologies. In Sample 16, the notable difference between tomography and metallography results can be attributed to the fact that metallography mainly investigates the surface. Fig. 50(b) illustrates that this sample exhibits significant porosity at the surface, whereas the bulk displays reduced porosity, highlighting the differences between these measurement techniques. The 3D tomography images depicted in Fig. 50(a) illustrate the distribution, morphology, and dimensions of the pores. In denser samples, such as Sample 52, the outcomes from both methods converge more closely due to the reduced porosity, resulting in a minimal disparity between the methods.

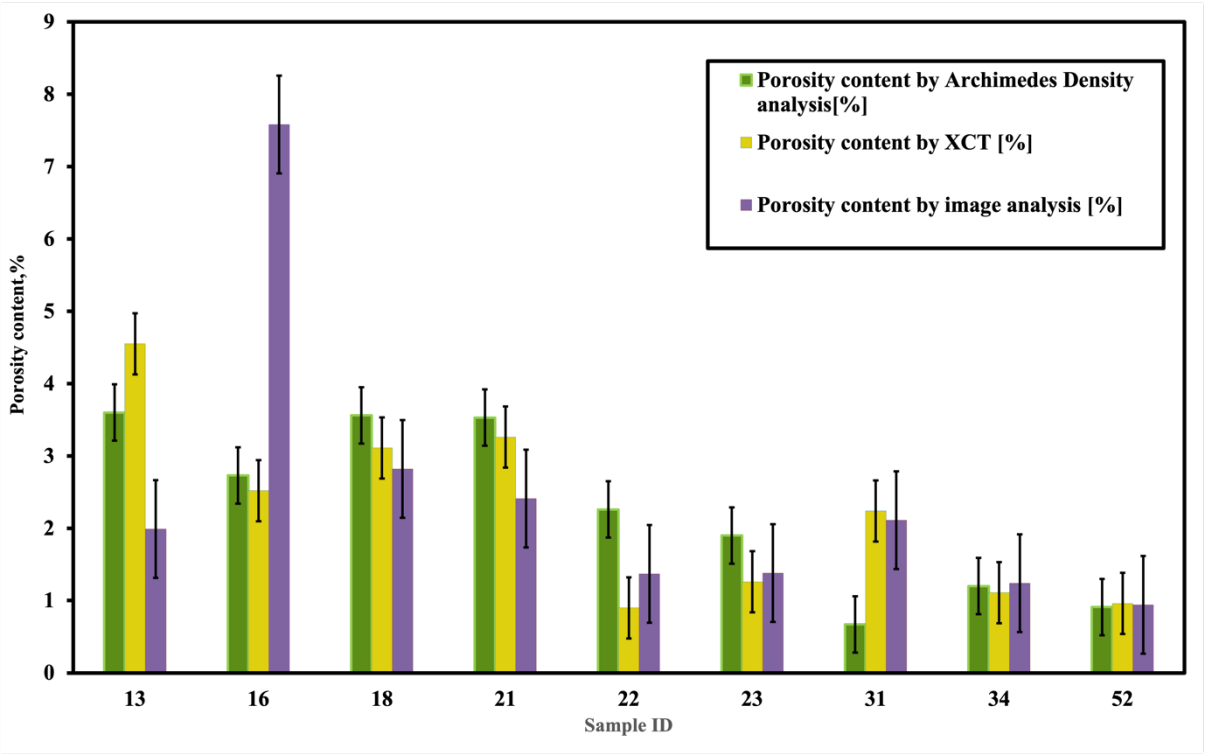

Fig. 49. Porosity percentage chart displaying the results after applying standard error to the data in Table 8.

Furthermore, after applying the standard error to all data in Table 9, the porosity percentage chart is illustrated in Fig. 49. This figure illustrates that, following the application of the standard error, the proximity of the data points is significant. The analysis concentrated exclusively on the Archimedes method applied to all 64 samples. The purpose of this analysis was to determine the closeness of the data using the Archimedes method to achieve a precise comprehension of its accuracy. The notable disparity identified in Sample 16 can be ascribed to the metallographic analysis, which is confined to a singular surface and indicates that the predominant porosity is localized in that region. Conversely, tomography revealed that the upper portion of the sample demonstrates markedly reduced porosity, underscoring a constraint of the metallographic technique.Fig. 50 demonstrates that the 3D representation depicts the distribution and morphology of the pores, showing that the majority of the porosity in Sample 16 is concentrated near the surface. This concentration yields a markedly porous appearance in the metallographic analysis. The metallographic and tomographic data for the remaining samples are relatively similar and consistent. Sample 52 demonstrates alignment between the 3D and 2D tomographic images shown in Fig. 50 (a) and (b), along with the metallographic image in Fig. 50 (c).

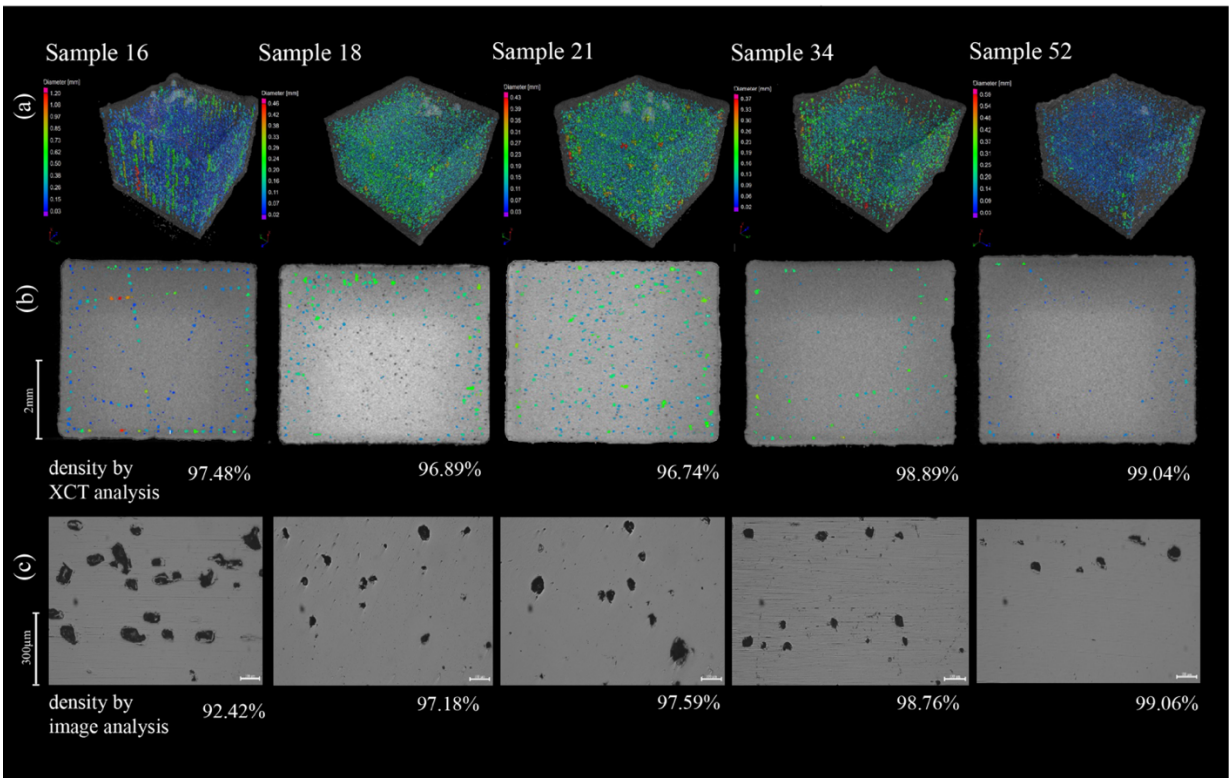

Fig. 50. This figure thoroughly analyzes the samples employing various density measurement techniques. (a) presents the 3D tomography, providing a comprehensive visualization of the sample structure, with each sample measuring 5 × 5 × 5 mm, (b) emphasizes the frontal perspective of the samples, displaying internal characteristics via tomography imaging, (c) presents metallographic images acquired through OM, comprehensively analyzing the sample's structure. Furthermore, the density values of the samples, obtained through XCT and image analysis techniques, are presented for comparison.

Fig. 51 depicts the influence of process parameters on the relative density of components as it varies with the VED. The intensity of the laser power is represented by the size of the points, whereas the hatch distance and scan speed are denoted by the color in Fig. 3a and Fig. 3b, respectively. The VED ranges from 33 to 283 J/mm³, resulting in component densities between 90.9% and 99.9%. Sample 38 demonstrated the greatest density at 99.9%, accompanied by a VED of 66 J/mm³. Insufficient laser energy at lower VED values leads to incomplete fusion, thereby diminishing the density of the components. However, when the VED surpasses 50 J/mm³, the L-PBF process yields components with a significant density, as evidenced by the optical micrographs presented in Fig. 51. As VED increases, a reduction in density transpires due to keyhole formation, underscoring the importance of vaporization effects at elevated VED levels. Consequently, both exceedingly low and exceedingly high values of VED are generally unsuitable for producing a fully dense component. Consequently, variations in the VED result in the observation of distinct types of porosities.

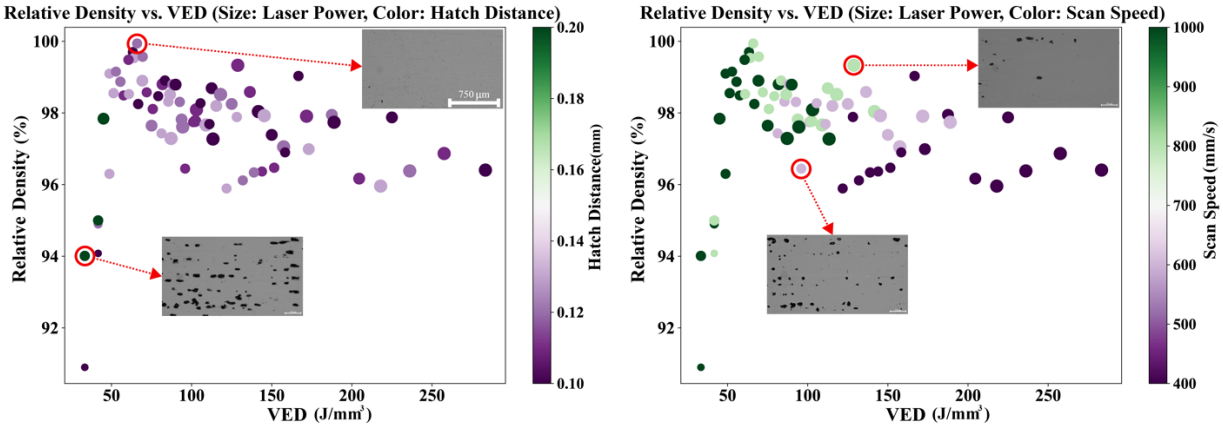

Fig. 51. Illustration of the relationship between VED and the relative density. The size of the points represents laser power, while color indicates (a) scan speed and (b) hatch distance.

4.3. Hyperparameter Tuning

Various ML models were utilized on the density measutrement data, assessing their impact to identify the most accurate and optimal model for process parameter optimization. Supervised learning is a prominent ML approach that employs labeled data segmented into training and testing sets, primarily to develop models that identify relationships between predictors (features) and the response (target) within the dataset. Supervised learning can be subdivided into two categories: regression, which forecasts continuous values, and classification, which entails predicting discrete class labels [131,194]. Given that the target variables and relative density in this study were continuous, regression models including SVR, GPR, GBR, k-NN, DT, RF, and Bayesian regression were utilized. A heat map was employed to analyze the influence of distinct hyperparameters associated with each ML model on the R^2 value. This analysis identified the three hyperparameters showing the most significant influence on the R^2 score. In the subsequent step, a 3D mesh plot was utilized to identify the hyperparameter configurations yielding the highest R^2 value. A 2D plot was employed to examine the correlation between the subsequent hyperparameter and various error metrics, including R^2, MSE, and MAE, to determine the optimal value for the hyperparameter. In the subsequent phase, following applying the selected hyperparameters to the ML model, a two-dimensional plot of predicted density against actual density was generated utilizing regression. This facilitated an assessment of which model provided the most precise prediction, exhibiting the closest correspondence between the predicted and actual data.

4.3.1. Heat map correlation plot

In the heat map correlation plot, as illustrated in Fig. 52 for various ML models, each model applied to the data has its distinct hyperparameters. To find the optimal value for each hyperparameter, heat maps were utilized to show the effect of each parameter on the R^2 score. The best hyperparameters were identified by examining the bottom row or last column, highlighting the parameters with the maximum impact. The three hyperparameters with the

most significant impact were selected for further analysis in the next stage, where the optimal value, corresponding to the lowest error, was determined for each. For instance, as shown in Fig. 52 (a) , the parameters C, kernel, and gamma were found to have the most significant impact. Similarly, for the other models, three hyperparameters were chosen for further examination to determine their precise values in the following optimization stage.

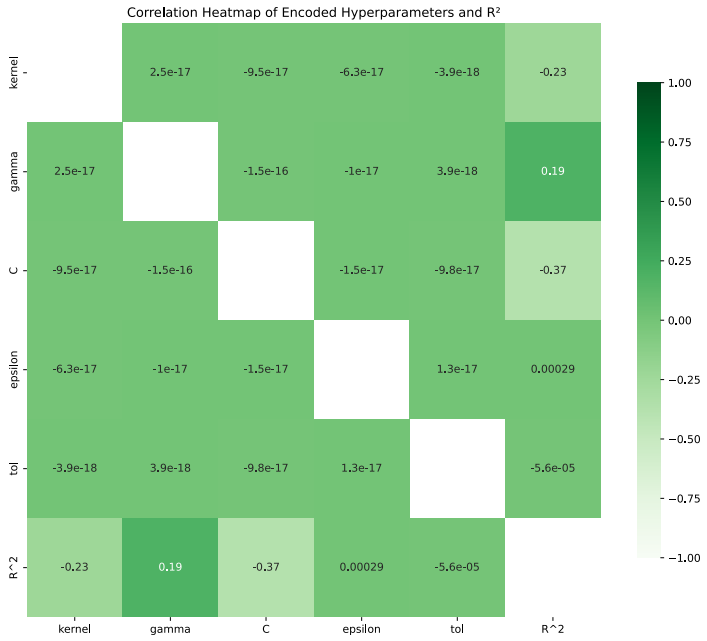

(a)

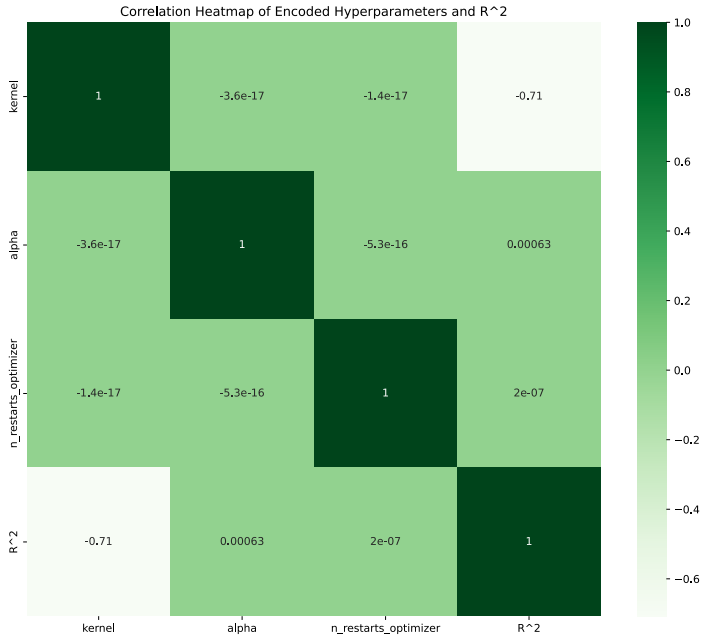

(b)

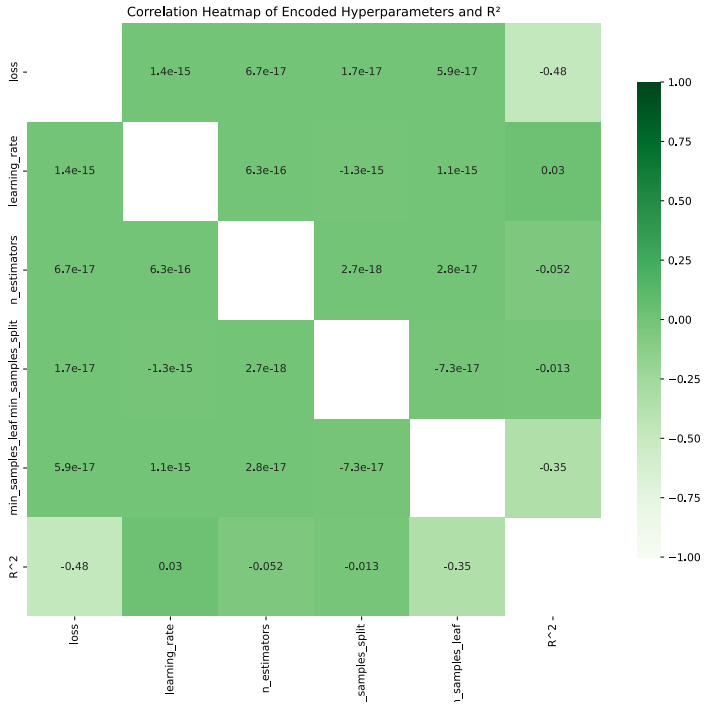
Correlation Heatmap of Encoded Hyperparameters and R²
loss
learning_rate
n_estimators
min_samples_split
min_samples_leaf
R^2
1.4e-15 6.7e-17 1.7e-17 5.9e-17 -0.48
1.4e-15 6.3e-16 -1.3e-15 1.1e-15 0.03
6.7e-17 6.3e-16 2.7e-18 2.8e-17 -0.052
1.7e-17 -1.3e-15 2.7e-18 -7.3e-17 -0.013
5.9e-17 1.1e-15 2.8e-17 -7.3e-17 -0.35
-0.48 0.03 -0.052 -0.013 -0.35
1.00
0.75
0.50
0.25
0.00
−0.25
−0.50
−0.75
−1.00

(c)

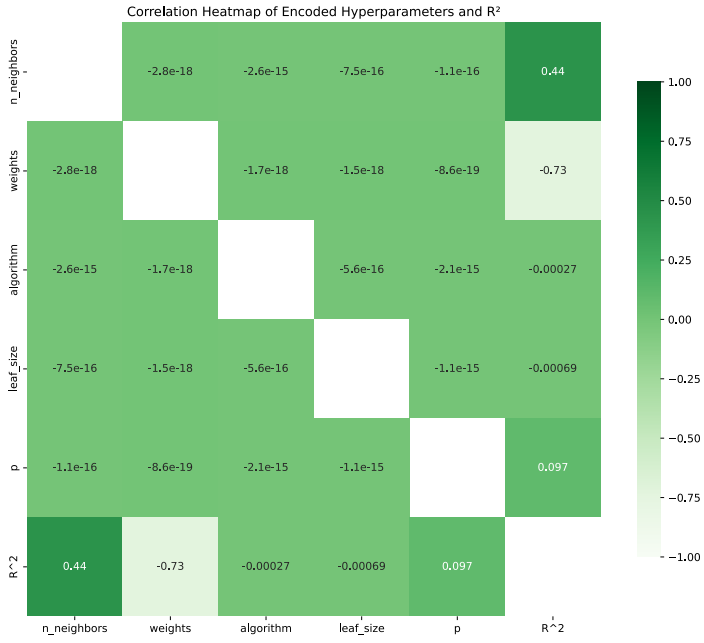
Correlation Heatmap of Encoded Hyperparameters and R²
n_neighbors
weights
algorithm
leaf_size
p
R^2
-2.8e-18 -2.6e-15 -7.5e-16 -1.1e-16 0.44
-2.8e-18 -1.7e-18 -1.5e-18 -8.6e-19 -0.73
-2.6e-15 -1.7e-18 -5.6e-16 -2.1e-15 -0.00027
-7.5e-16 -1.5e-18 -5.6e-16 -1.1e-15 -0.00069
-1.1e-16 -8.6e-19 -2.1e-15 -1.1e-15 0.097
0.44 -0.73 -0.00027 -0.00069 0.097
1.00
0.75
0.50
0.25
0.00
−0.25
−0.50
−0.75
−1.00

(d)

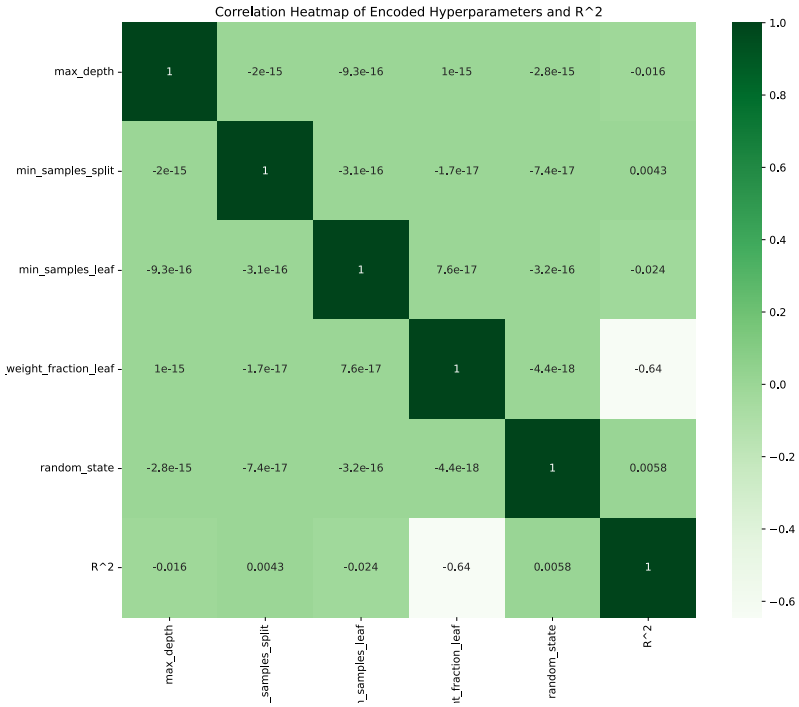
Correlation Heatmap of Encoded Hyperparameters and R^2
max_depth
min_samples_split
min_samples_leaf
weight_fraction_leaf
random_state
R^2
1
-2e-15
-9.3e-16
1e-15
-2.8e-15
-0.016
-2e-15
1
-3.1e-16
-1.7e-17
-7.4e-17
0.0043
-9.3e-16
-3.1e-16
1
7.6e-17
-3.2e-16
-0.024
1e-15
-1.7e-17
7.6e-17
1
-4.4e-18
-0.64
-2.8e-15
-7.4e-17
-3.2e-16
-4.4e-18
1
0.0058
-0.016
0.0043
-0.024
-0.64
0.0058
1
1.0
0.8
0.6
0.4
0.2
0.0
−0.2
−0.4
−0.6

(e)

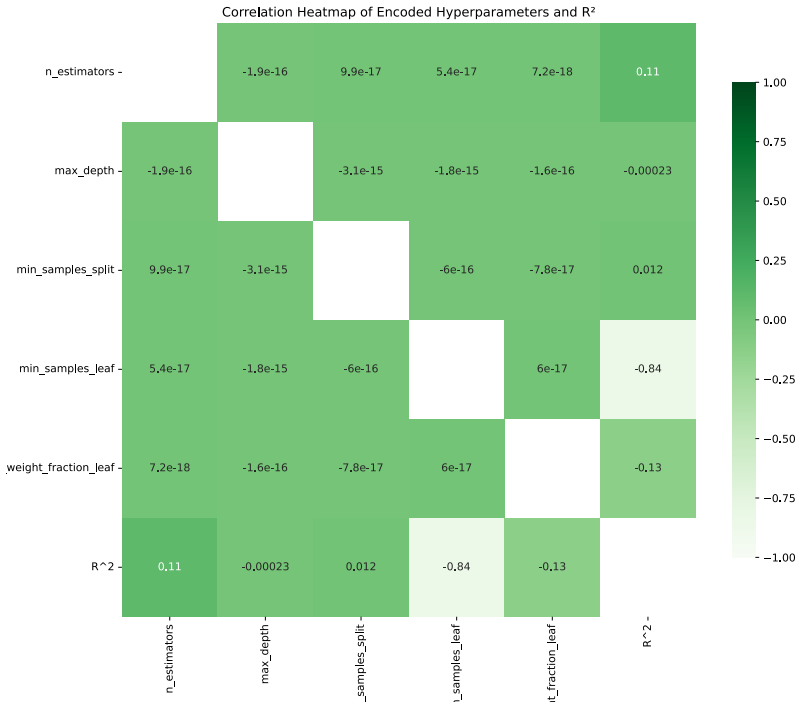
Correlation Heatmap of Encoded Hyperparameters and R²
n_estimators
max_depth
min_samples_split
min_samples_leaf
weight_fraction_leaf
R^2
-1.9e-16
9.9e-17
5.4e-17
7.2e-18
0.11
-1.9e-16
-3.1e-15
-1.8e-15
-1.6e-16
-0.00023
9.9e-17
-3.1e-15
-6e-16
-7.8e-17
0.012
5.4e-17
-1.8e-15
-6e-16
6e-17
-0.84
7.2e-18
-1.6e-16
-7.8e-17
6e-17
-0.13
0.11
-0.00023
0.012
-0.84
-0.13
1.00
0.75
0.50
0.25
0.00
−0.25
−0.50
−0.75
−1.00

(f)

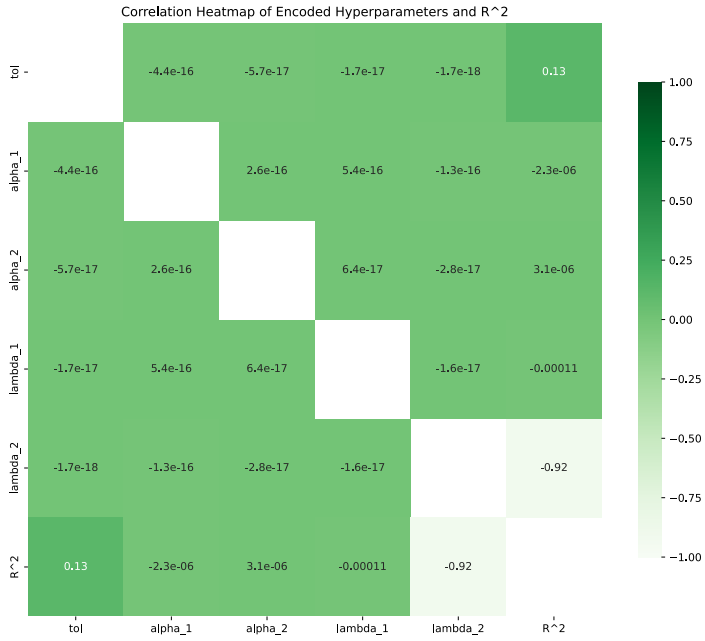

(g)

Fig. 52.Heat map correlation plot illustrating the impact of different hyperparameters on the R^2 score for various ML models: (a) SVR, (b) GPR, (c) GBR, (d) k-NN, (e) DT, (f) RF, and (g) Bayesian Regression. The color intensity represents the degree of influence each hyperparameter has on the model's performance. (training size is 80%)

4.3.2. 3D plot surafce

At this stage, a 3D plot is created utilizing two of the hyperparameters chosen in the preceding step, and the maximum R^2, indicative of the minimal error, is determined for each model. Fig. 53 depicts the optimal hyperparameter values that yield the R^2 for each model. Following this step, only one hyperparameter remains unassigned a value. In the subsequent phase, a 2D plot is employed to ascertain the optimal value for the remaining hyperparameter by analyzing the minimal errors.

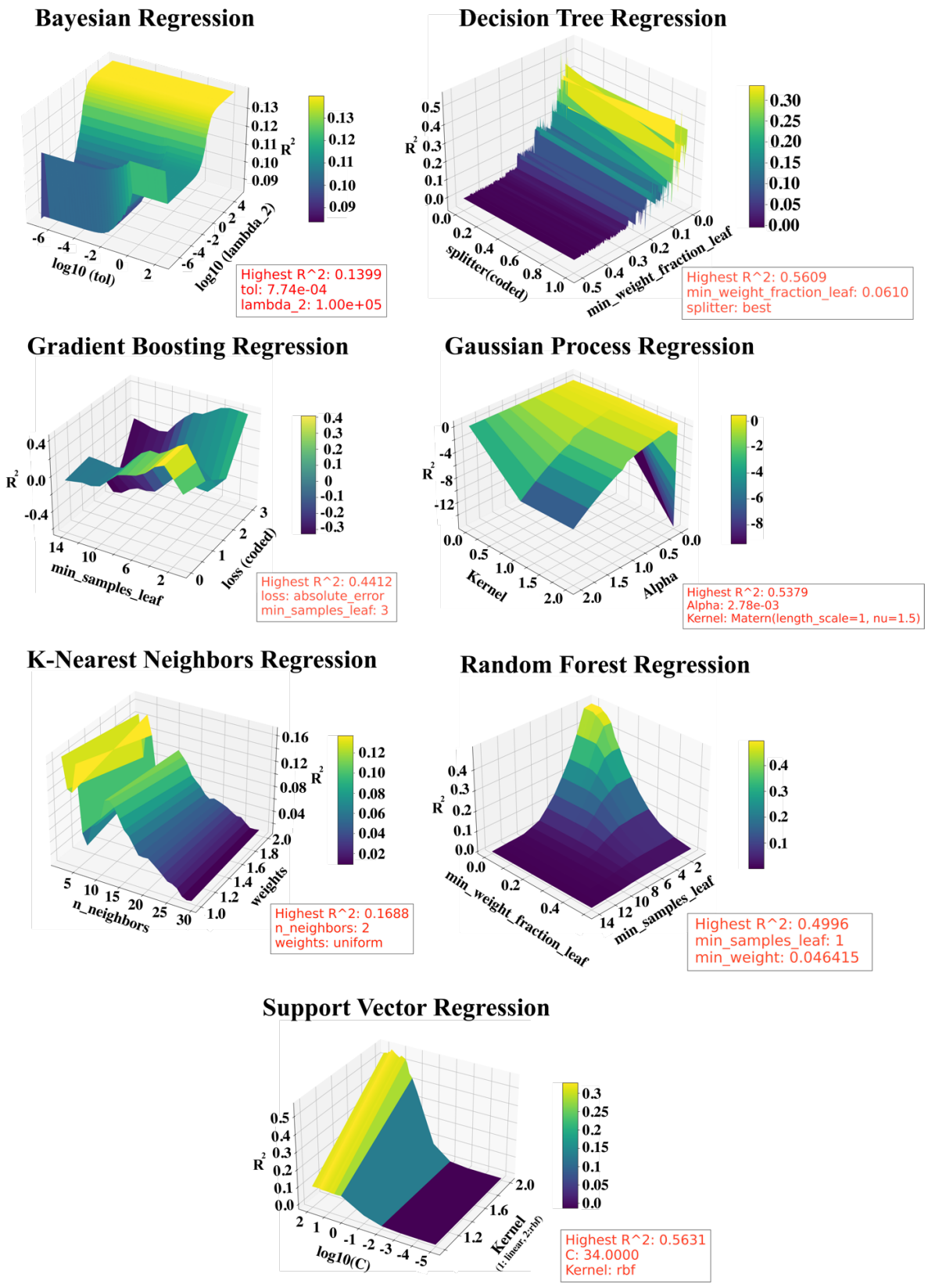

Fig. 53. 3D plots illustrating the optimal hyperparameter values for achieving the maximum R^2 score (minimum error) for various machine learning models.

4.3.3. 2D plot Based on Hyperparameter Optimization

The following part employs 2D plots to identify the optimal value for the third hyperparameter, utilizing three distinct error metrics: R^2, MSE, and MAE, as depicted in Fig. 54. The ideal value for the third hyperparameter is determined by the criterion that an elevated R^2 and lowered MSE and MAE signify superior model performance with minimized error. This step represents the last stage of hyperparameter selection, wherein values for all hyperparameters have been established for each model. The next step is to investigate the error rates of the various models.

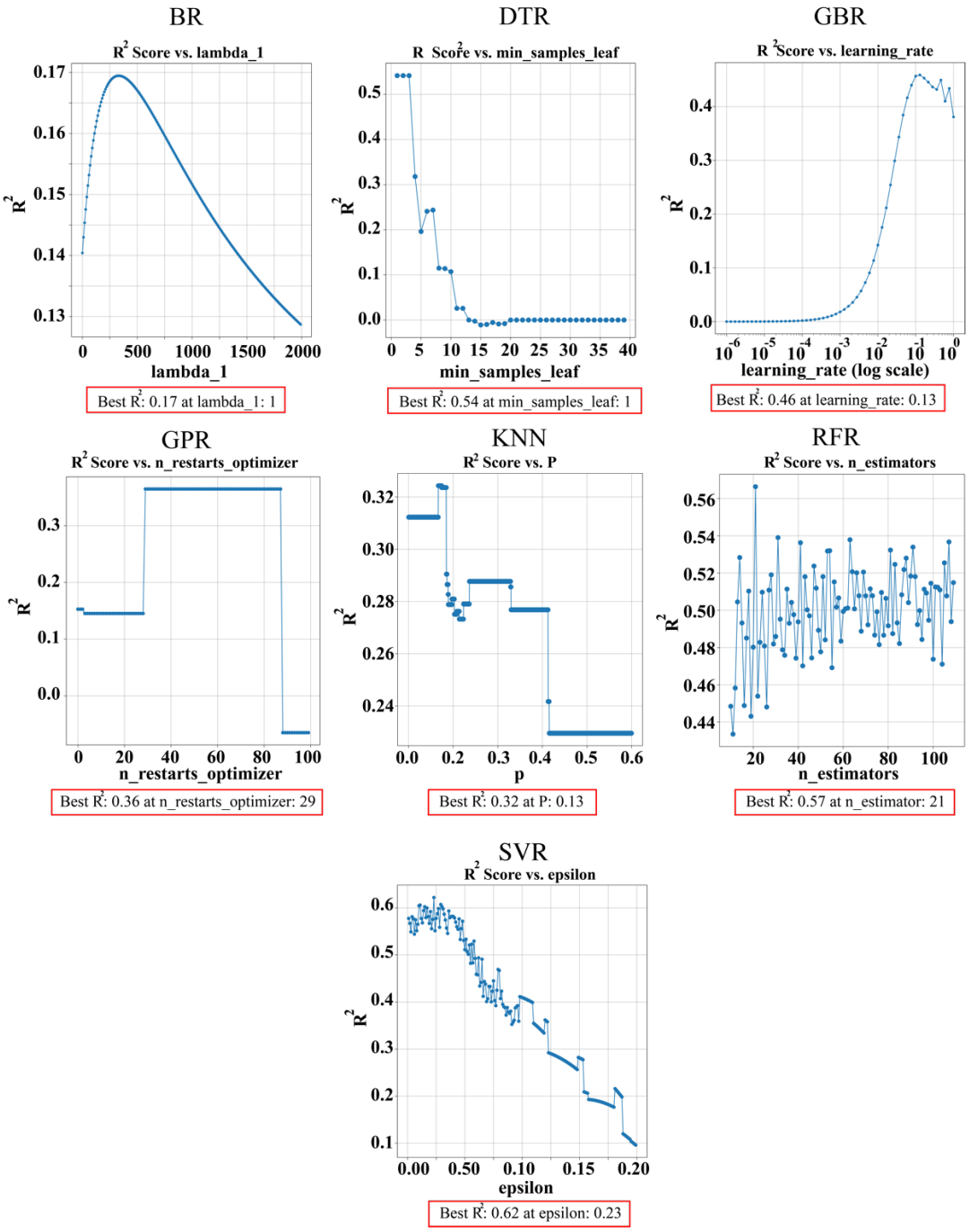

Fig. 54.2D plots showing the optimal value selection for the third hyperparameter based on three error metrics, including R^2, MSE, and MAE for various ML models.

4.3.4. Model Evaluation

This section has identified the optimal hyperparameters for the models. To assess performance, a graph of predicted density against actual density is created for each model as can be seen in Fig. 55, and regression analysis is employed to evaluate accuracy. The model exhibiting the highest R^2 value, nearest to 1, is considered the most precise for prediction.

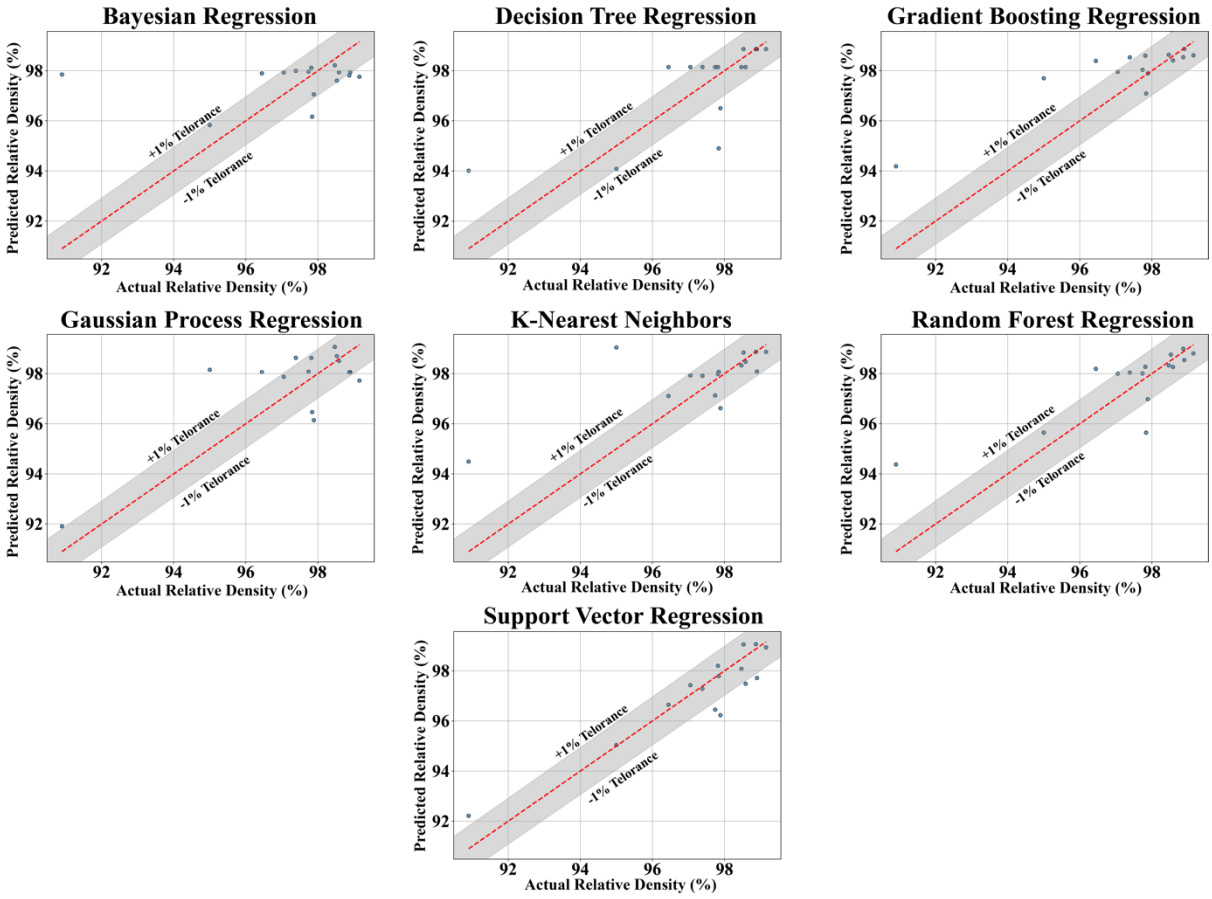

Fig. 55. Comparison of predicted vs. actual relative densities for all algorithms at 80% training size. The red dashed line indicates the optimal prediction (when projected values align with actual values), and the gray-shaded area indicates ±1% tolerance range.

After completing the hyperparameter tuning process and identifying the optimized hyperparameters, we employed these values in the machine learning algorithms to forecast the target variable (the relative density of the testing data) for which the actual values were previously established. The efficacy of each model was subsequently evaluated by measuring the discrepancies between the predicted and actual values. The influence of varying training sizes on model performance, evaluated via R2, MAE, and MSE, is a critical aspect of model assessment and enhancement. Figure 8 illustrates the influence of different training sizes (40%, 50%, 60%, 70%, 80%, 90%) on the specified error metrics across multiple algorithms including Bayesian Regressor, Decision Tree Regression, GBR, GPR, KNN, SVR, and RF. Fig. 56 (a) reveals a general trend where an increase in training size percentage correlates with a rise in MSE across most algorithms, adversely impacting prediction accuracy. The augmentation in MSE is more pronounced in the Bayesian Regressor. For example, with a training size of 40%,

the Bayesian Regressor exhibits an MSE of 1.987, which escalates to 7.043 when the training size is increased to 90%. The substantial increase in MSE underscores the model's susceptibility to reduced testing size, resulting in diminished predictive efficacy. Conversely, certain algorithms, like SVR, exhibit an inverse trend, wherein an increase in training size results in a reduction of the MSE, signifying improved predictive accuracy with larger datasets.

The influence of train size on MAE, illustrated in Fig. 56 (b), exhibits a comparable trend to that of MSE. The minimal MAE values are generally recorded at a 60% training size, whereas increased training sizes of 90% yield elevated MAE values. In the GBR model, the MAE is 0.713 at a 60% training size, increasing to 0.896 at 90%. This indicates that a 60% training size may produce optimal results for minimizing MAE; however, it is crucial to consider additional error metrics, such as MSE and R^2, to determine the most suitable training size for overall model efficacy.Fig. 56 (c)illustrates that the coefficient of determination (R^2) escalates with an increase in training size, signifying enhanced predictive accuracy. Notable enhancements in R^2 manifest when the training size attains 80% and 90%. In the GPR model, the R^2 value begins at 0.252 with a 40% training size and exceeds 0.856 when the training size increases to 90%. The SVR model exhibits a notable enhancement, with the R^2 rising from 0.344 at a 40% training size to 0.842 and 0.871 at 80% and 90%, respectively. This trend is not uniform across all algorithms. In the Bayesian Regressor, a contrasting trend is evident, as an increase in training size results in a reduction of R2, underscoring the unique characteristics of each algorithm. Utilizing 90% of the data for training typically yields the highest R^2 score across multiple algorithms; however, employing merely 10% of the data for testing results in an elevation of MAE and MSE. This indicates that relying solely on R^2 is insufficient for assessing the accuracy of the model's predictions; additional error metrics must also be taken into account.

The findings demonstrate that a training size of 80% attains an optimal equilibrium among three distinct error metrics, contingent upon the algorithm utilized. Among the examined algorithms, SVR demonstrates superior accuracy across nearly all training sizes, whereas the Bayesian Regressor exhibits the least predictive efficacy throughout the assessment. These findings underscore the importance of selecting an appropriate training size and optimal hyperparameters to enhance accuracy and error metrics for each algorithm.

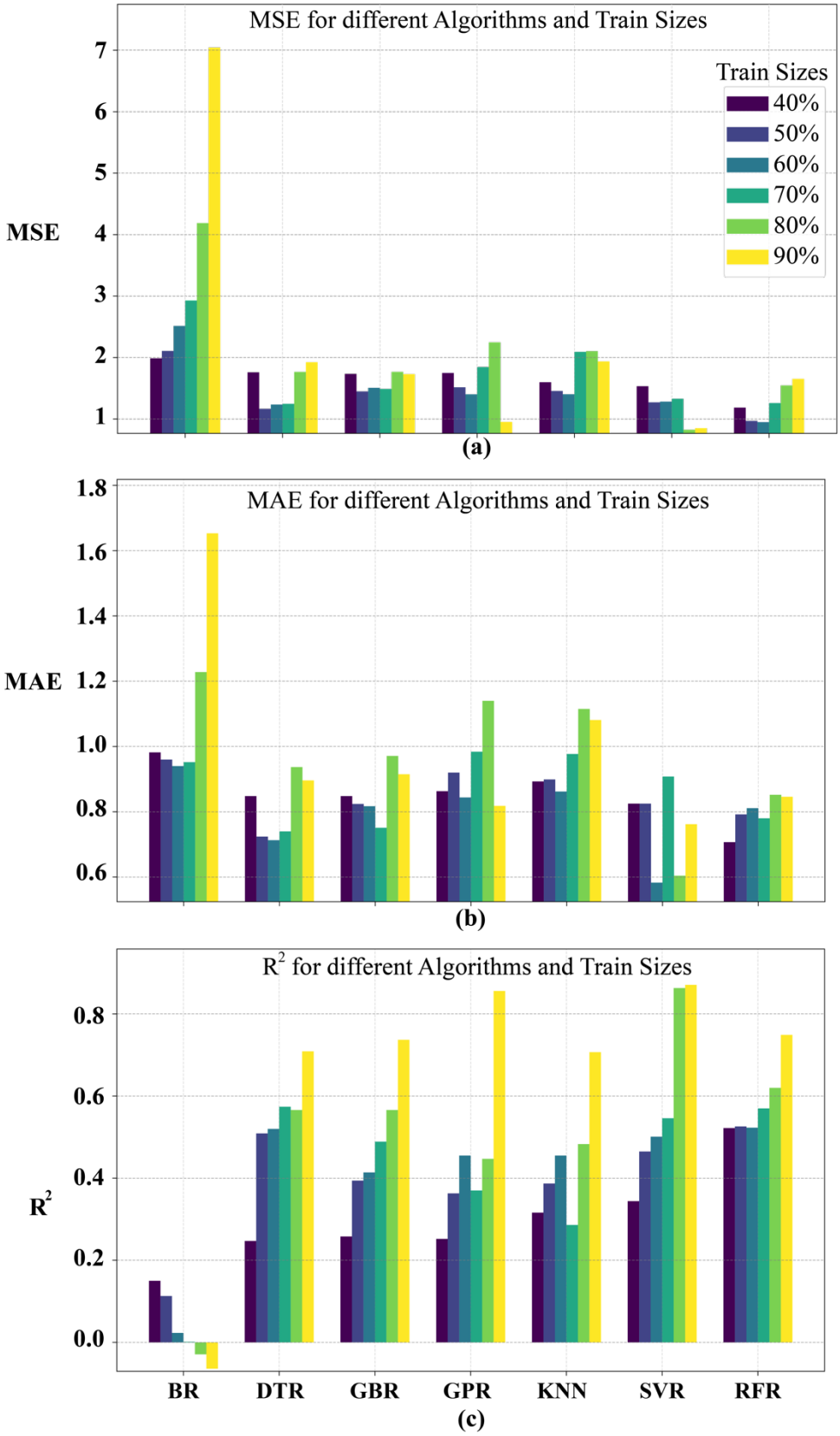

Fig. 56. R2, MAE, and MSE values for different values and train sizes of each machine learning algorithm.

4.4. Final Model Selection

Following the assessment of the models, the optimal machine learning model for density prediction has been identified which was SVR. Subsequently, the ideal process parameters for the desired feature can be predicted utilizing the most accurate model, resulting in reduced powder usage for printing and time and cost savings. Supplementary advantages encompass enhanced efficiency and diminished material waste in production, thereby fostering more sustainable and economically viable manufacturing.

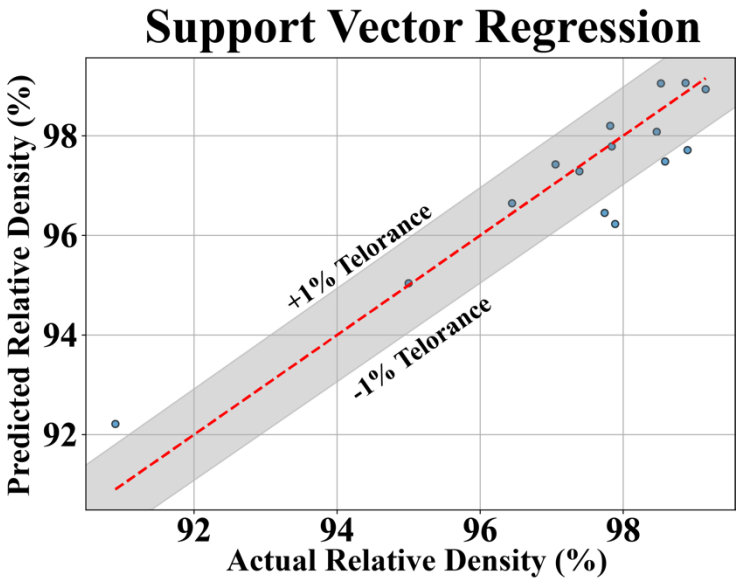

Fig. 57. Comparison of predicted vs. actual relative densities for SVR algorithms at 80% training size.

4.5. Selected Model Verification

Fig. 58 compares the actual and predicted relative densities achieved by the optimal machine-learning model utilizing testing data. The SVR algorithm, using optimized hyperparameters (kernel = rbf, C = 215.44, Max_iter = 990, tol = 0.0278, epsilon = 0.1), was employed to forecast relative densities at 15 testing points. Among the models, SVR demonstrated superior performance, achieving the lowest MAE of 0.601, MSE of 0.640, and the highest R2 of 0.842 with a training size of 80%. The predictions closely align with the actual values, as illustrated in Fig. 58. Furthermore, Fig. 58 illustrates the optimal values of the target variable (relative density), the associated VED, and the similar trend depicted in Fig. 51for manufacturing under optimal conditions.

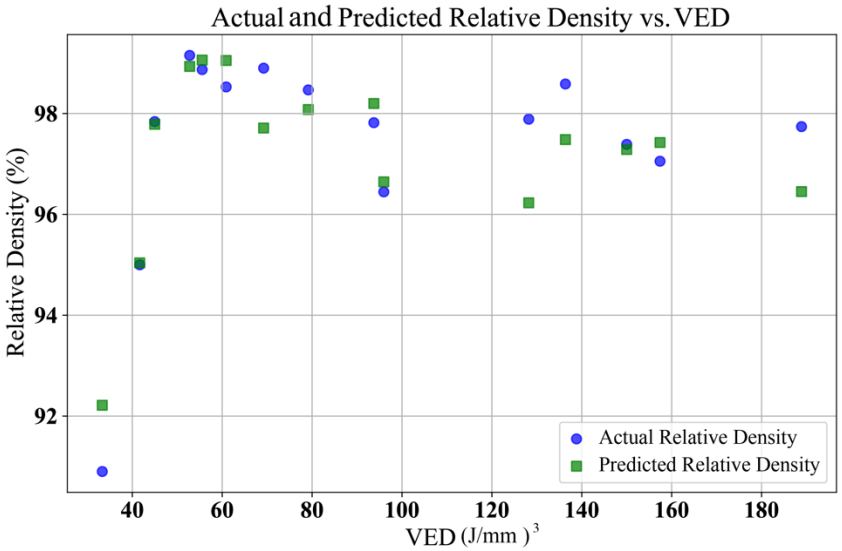

Fig. 58. Comparison of actual and predicted relative density as a function of calculated VED using SVR with optimized hyperparameters at the training size of 80%.

Fig. 59 illustrates the predicted relative density for four different scan speeds: 400, 600, 800, and 1000 mm/s based on the best predictor model, SVR at the training size of 80% with specific optimized hyperparameters. These values are within the specified range of hatch distance (0.1 to 0.2 mm) and power (100 to 400 W). Generally, as the scan speed increases, the contour plots in Figure 10 indicate a continuous rise in predicted relative density, as shown by the expansion of yellow and green regions. This trend highlights the influence of scan speed on the densification process, where higher scanning speeds caused enhanced relative density under the given conditions.At a scanning speed of 400 mm/s, the minimum relative densities are observed in the power range of 300 to 400 W, independent of the hatch distance. Conversely, the highest relative densities at this scan speed are obtained when the power ranges from 100 to 200 W, with the hatch distance between 0.13 and 0.15 mm. This suggests that optimal relative density at the scan speed of 400 mm/s can be achieved within these specific process parameters at lower power levels combined with moderate hatch distances.At a scanning speed of 600 mm/s, the predicted relative density improved across the entire hatch distance and power range compared to the previous scan speed. However, the maximum predicted relative density is still lower at scanning speeds of 800 and 1000 mm/s. The lowest relative density is observed when the power exceeds 300 W, particularly at hatch distances less than 0.12 mm. On the other hand, when the power is less than 300 W, the highest relative densities are achieved in two specific hatch distance ranges, 0.10 to 0.11 m, and 0.15 to 0.18 mm.The maximum predicted relative density at a scan speed of 800 mm/s increased by 0.8% compared to the previous scan speed of 600 mm/s, and by 1.1% compared to the speed of 400 mm/s, reaching a peak of 99.5%. The highest relative densities were achieved in the hatch distance range of 0.12 to 0.18 mm. However, at high P values, particularly around 400 W, the highest percentage of porosity would be possible, especially in small hatch distance ranges.At the scanning speed of 1000 mm/s, the maximum relative density decreased by 0.5%. The predicted relative density value reached its lowest value at the hatch distance range of less than 0.12 mm. For hatch distances greater than 0.12 mm, the power should be set between 100 and 250 W to achieve high relative

density, particularly at a hatch distance of 0.14 mm.Based on Fig. 59, it can be concluded that while high relative density values are achievable in all four plots, a scanning speed of 800 mm/s can be considered the optimal value. At this scanning speed, porosities can be further minimized using a power setting of approximately 250 W and a hatch distance of 0.13 mm. By analyzing the relationship between process parameters and porosity content, various objectives, such as maximizing productivity and identifying optimal process parameters for that, can be achieved through this model.

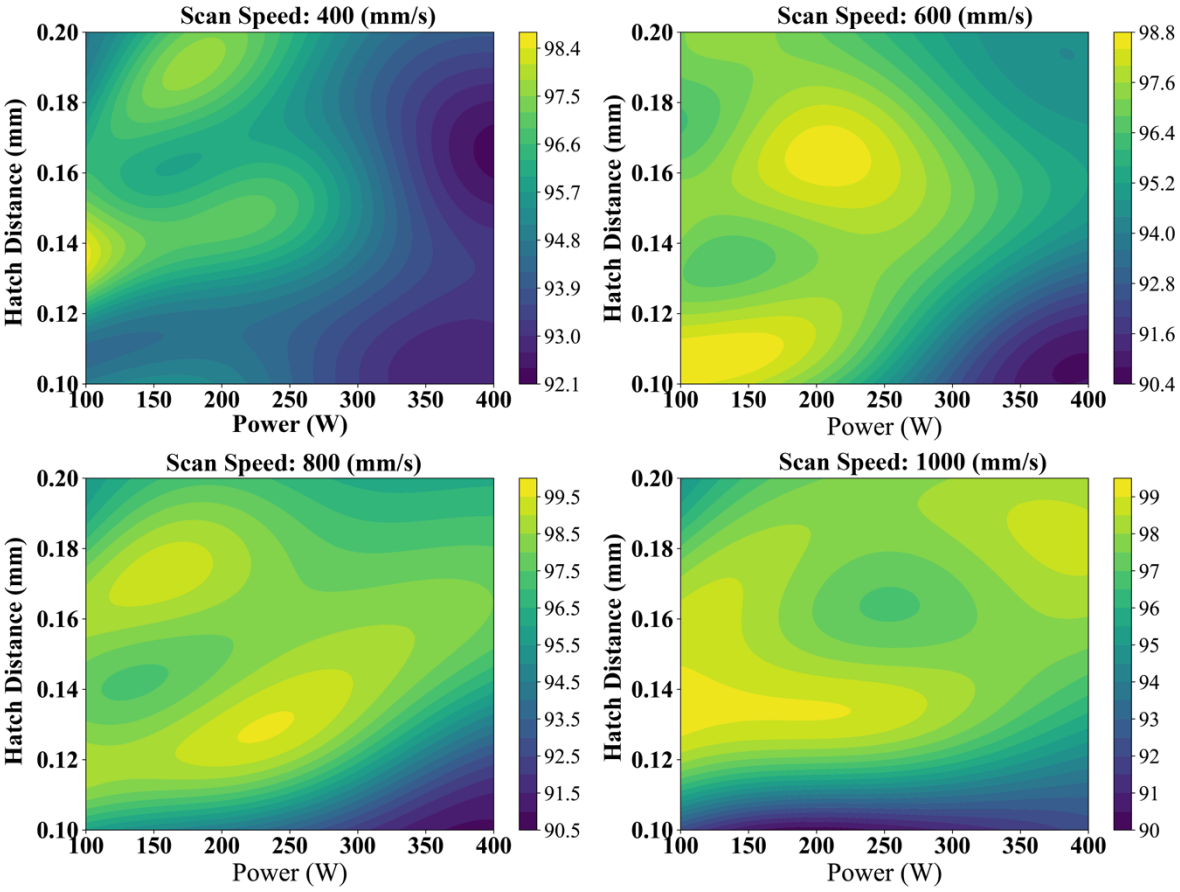

Fig. 59. Illustration of predicted relative density for different scan speeds (400, 600, 800, and 1000 mm/s) by varying power (100-400 W) and hatch distance (0.1-0.2 mm) ranges, using the SVR algorithm at the training size of 80% after hyperparameter tuning.

4.6. Microstructure Analysis

Based on different VEDs, AISI 316L-Cu samples exhibit different densities. Fig. 60 presents OM images comparing different AISI 316L-Cu samples. In these images, the ring-shaped melt pools observed for the AISI 316L-Cu samples have average depth of 100 µm, and widths of 89 µm, respectively. This difference in melt pool dimensions is likely due to the rapid solidification and increased temperature gradient resulting from copper's significantly higher thermal conductivity (approximately 385 W/m·K) compared to that of stainless steel (10–30 W/m·K)[195].It is well known that copper can dissolve into iron, forming a substitutional solid solution within the steel matrix[196]. As copper is an austenite stabilizer, its presence is

expected to promote a fully austenitic microstructure. This finding aligns with earlier research, suggesting that copper atoms in solid solution, or substituting for iron atoms, may contribute to a slight increase in lattice distortion of the austenite phase[197]. Studies have indicated that materials with higher thermal conductivity exhibit an elevated temperature gradient and enhanced cooling rate during solidification, which supports faster heat extraction during dendrite formation, ultimately leading to finer microstructures[195].

The microstructural analysis focuses on understanding the influence of process parameters on the melt pool geometry, analyzing type of cells, and porosity distribution within the samples. Variations in laser power, scanning speed, and hatch distance directly impact the melt pool dimensions which subsequently govern the solidification behavior and microstructural characteristics. By adjusting these parameters, it is possible to optimize the grain structure and minimize defects, ultimately enhancing the mechanical properties of the material. Higher energy densities promote deeper melt pools, leading to slower cooling rates and coarser grains. Conversely, lower energy densities result in shallower melt pools, faster cooling rates, and finer grains [198].

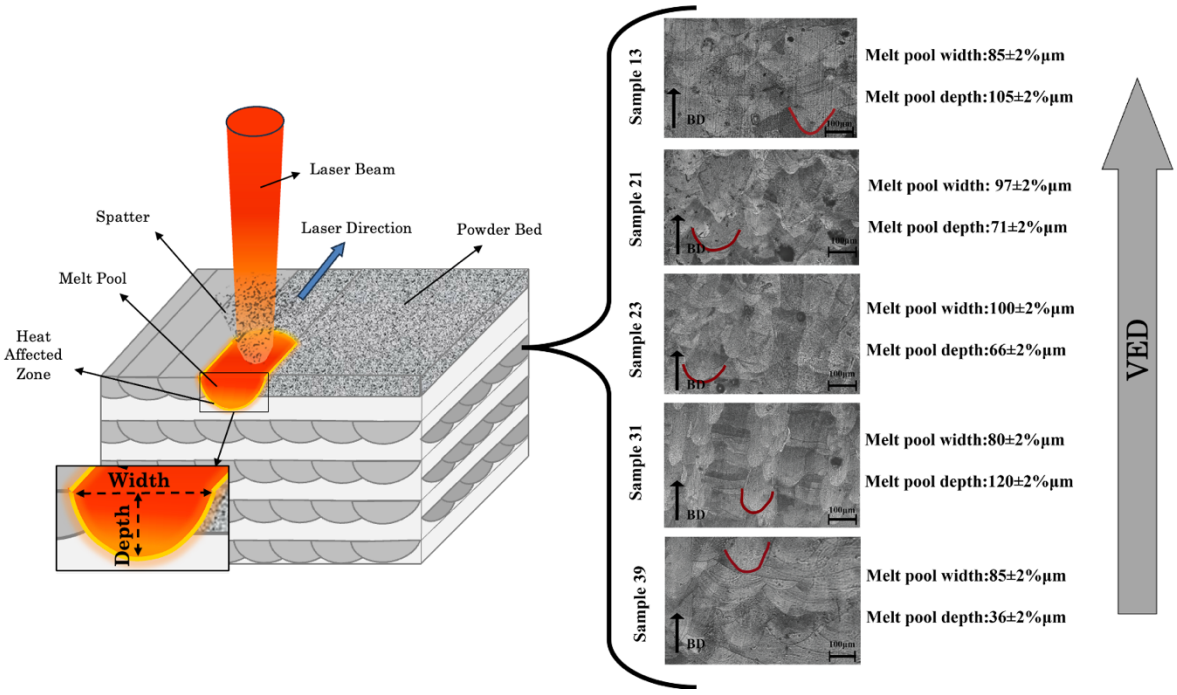

Fig. 60. Schematic depiction of melt pool geometry in laser-based AM , highlighting melt pool width and depth. Microscopic images of melt pools illustrate differences in shape and depth under diverse processing conditions. The red outlines delineate the boundaries of the melt pool, while the build direction (BD) arrows signify the layer-wise stacking in the manufacturing process.

Fig. 60 provides a detailed examination of melt pool geometry in laser-based AM. The left side illustrates a schematic representation of the melt pool created by the interaction of a laser beam with the material. This schematic emphasizes two essential dimensions, melt pool width, denoting the horizontal extent of the pool, and melt pool height (or depth), indicating the

penetration depth of the melt pool into the material. The dimensions are directly affected by process parameters including laser power, scanning speed, and hatch distance. Increased laser power generally leads to a deeper melt pool, whereas elevated scan speeds tend to create a shallower pool. The geometrical variations are essential for regulating the solidification behavior, microstructure, and ultimately the mechanical properties of the material [198]. On the right side of Fig. 60, a collection of micrographs illustrates the melt pool configurations observed in various samples. These samples were selected to investigate the melt pools with varying VEDs. The red outlines in each image demonstrate the boundaries of the melt pools, which display the characteristic semi-circular profiles typical of laser-based additive manufacturing. The build direction (BD), denoted by arrows in the images, illustrates the vertical layering of components throughout the process. The geometries of the melt pool vary according to the process conditions, with curvature and depth differing among samples. Images with high magnification emphasize intricate details of the microstructure, such as grain boundaries and possible defects like porosity. Shallow melt pools typically result in accelerated cooling rates and finer grain structures, thereby improving mechanical properties such as strength and toughness. Conversely, deeper melt pools exhibit a slower cooling rate, leading to the formation of coarser grains. Moreover, defects such as pores, cracks, or unmelted areas may be discerned at elevated magnifications, potentially resulting from inadequate energy input or improper melting processes. These defects adversely affect the density and mechanical properties of the final component. A noticeable trend indicates that a rise in VED is associated with an enlarged melt pool size, which can substantially affect the microstructural characteristics of the samples. This observation relies on evaluating essential characteristics, including the depth, width, and overall geometry of the melt pools, which are pivotal in influencing the mechanical properties and integrity of the final product.Though indicative of a singular instance, this observation has yet to be thoroughly evaluated across all samples. Consequently, the conclusion reached remains broad. The dimensions of the melt pools in each sample are specified, illustrating this prevailing trend. Moreover, variations in melt pool characteristics may impact cooling rates and solidification behavior, subsequently affecting the distribution of porosity and alloying elements within the samples. These insights emphasize the intricacy of the AM process and underscore the need for additional research into the correlations among processing parameters, melt pool morphology, and resultant material properties. A thorough comprehension is crucial for optimizing the additive manufacturing process and improving the performance of the final components [199,200].

The SEM backscattered images in Fig. 61(a) and (b) depict the microstructure of the as-fabricated AISI316L-Cu sample52. Fig. 61(a) depicts the grain structures within the melt pools that developed throughout solidification. Fig. 61(b) presents an enlarged perspective This figure illustrates the solidification of the melt pool, comprising both columnar grains and delicate cellular structures at the microstructural level. This substructure is probably associated with the elevated cooling rate, the intricate and non-equilibrium thermal history of the L-PBF process, and fluctuations in chemical composition resulting from insufficient homogenization of larger atoms [201]. Various substructures are located at the junctions of multiple melt track borders, resulting in intricate growth orientations of columnar grains perpendicular to the BD, considerably affecting tensile properties.

, whereby region (1) is defined by equiaxed cells, signifying rapid solidification within the melt pool. This microstructure is recognized for increasing mechanical strength and facilitating isotropic characteristics. Conversely, region (2) has columnar cells resulting from directed solidification, frequently resulting in anisotropic material behavior. The interplay of equiaxed and columnar grain patterns, influenced by specific process factors like laser power, scanning speed, and hatch distance, is vital in defining the material's mechanical properties. The equilibrium between isotropic and anisotropic properties substantially affects tensile strength, and yield strength. The coexistence of different grain forms indicates regulated temperature gradients during solidification, which directly influences the material's performance and application potential[179].

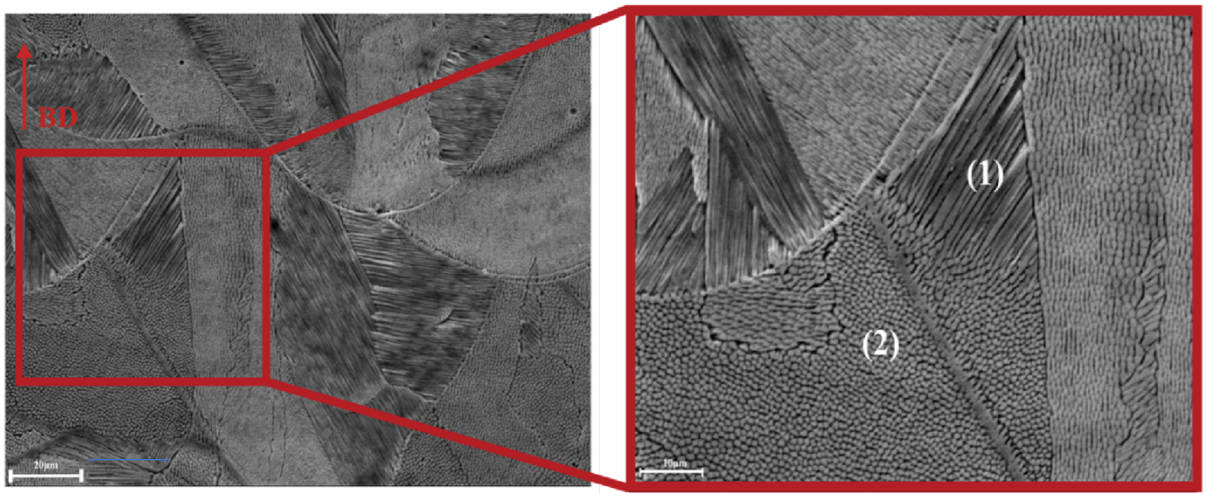

Fig. 61.SEM backscattered images highlighting the microstructure of sample 52. (a) depicts the melt pools with clearly defined grain shapes, (b) offers an enlarged perspective, with (1) displaying equiaxed cells and (2) presenting columnar cells.

Prior research [202] has demonstrated that the dimensions of the melt pool are affected by the parameters of the L-PBF process, leading to irregular overlaps and variations between neighboring layers.The cell size of the as-fabricated AISI316L-Cu samples, determined via the triangle method [16], is 0.68 ± 2% μm. The intricate cellular microstructure results from the elevated cooling rate caused by the localized quenching process. Numerous researchers have reported that the cooling rate during solidification is a critical parameter that inversely influences cell size[16]. The cooling rate for the AISI316L-Cu sample was estimated at 1.8 × 10^6 K/s, signifying that the incorporation of copper increased thermal conductivity, thereby improving the cooling rate during the L-PBF process and subsequently decreasing cell size.

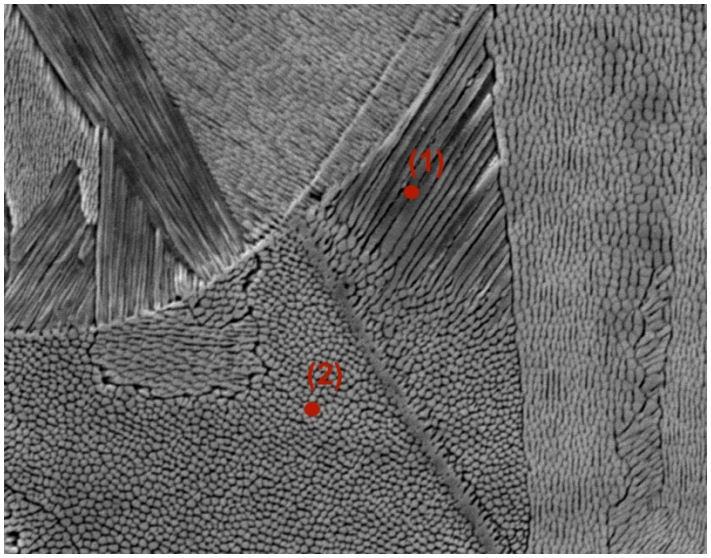

Fig. 62.Backscattered SEM image displaying columnar and equiaxed cellular structures.

The EDS analysis results, illustrated in Fig. 63 for Spot 1 in (a) and Spot 2 in (b), reveal elemental peaks for Fe, Cr, Ni, Mo, and Cu. Accelerated solidification during the construction process, coupled with the reheating of the solidified layers, may facilitate the segregation of alloying elements and induce microstructural variations. This results in a more luminous appearance in the backscattered SEM image, ascribed to elevated concentrations of alloying elements and localized elemental segregation during the L-PBF process. Fig. 62 depicts the backscattered SEM image, revealing distinct microstructural characteristics of the as-fabricated AISI316L-Cu sample. The pronounced contrast in specific areas signifies the presence of higher atomic number elements, such as nickel and molybdenum, which can augment the material's strength and resistance to corrosion. The interfaces between different microstructural features may act as potential sites for crack initiation under stress. Table 10 presents the EDS elemental analysis findings for Spots 1 and 2 . The tables present comprehensive data on the composition of the examined regions, emphasizing the variations in elemental distribution and concentration that can substantially affect the alloy's mechanical properties.

Table 10.EDS elemental analysis results for Spots 1 and 2 in Fig. 62.

Element	spot1 (Weight %)	spot1 (Atomic %)	spot2 (Weight %)	spot2 (Atomic %)
MoL	3.56	2.09	4.24	2.51
CrK	16.66	18.05	16.61	18.11
FeK	69.38	70.00	65.65	66.62
NiK	8.82	8.46	9.93	9.59
CuK	1.58	1.40	3.56	3.18

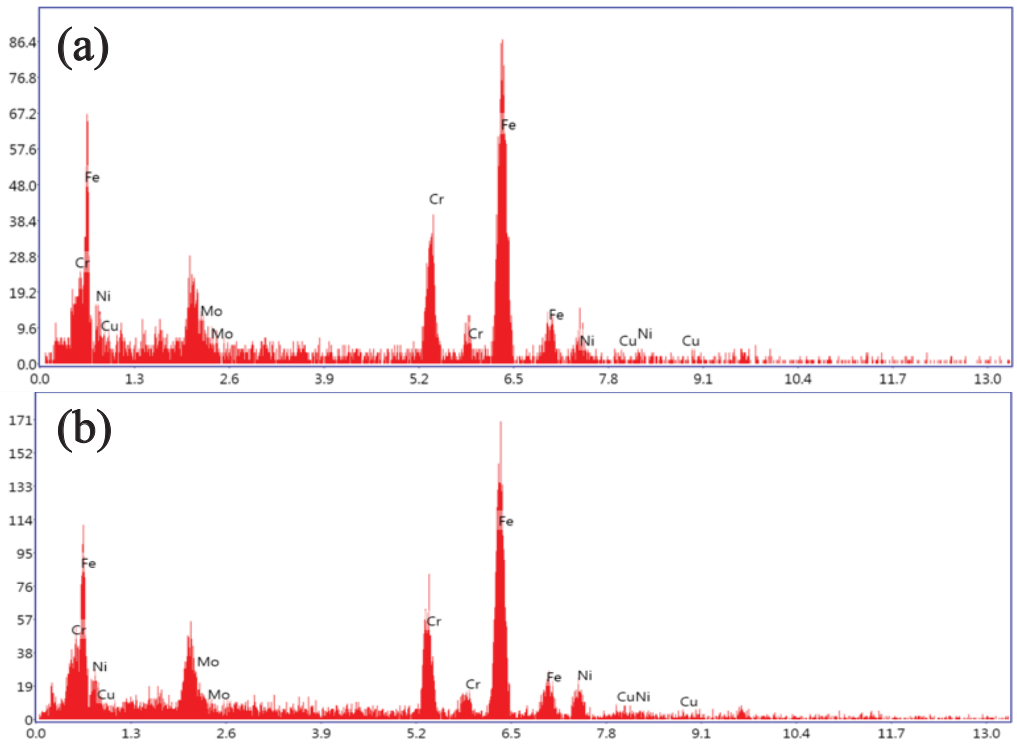

Fig. 63. EDS analysis for Spot 1 in Fig. (a) and Spot 2 in Fig. (b), shows elemental peaks for Fe, Cr, Ni, Mo, and Cu.

4.7. Mechanical test

Tensile tests on samples with various porosity levels demonstrate a distinct inverse correlation between porosity, tensile strength, and other mechanical properties. The specimen with the most significant porosity demonstrated the least tensile strength, while the specimen with the lowest amount of porosity exhibited the highest strength among the samples. The red curve in Fig. 64 denotes a maximum tensile strength of 550 MPa, signifying the sample with the least porosity. The green curve, at 538 MPa, and the blue curve, at 489.9 MPa, further illustrate this trend, emphasizing the influence of porosity on mechanical performance. The curves display a similar initial elastic region but diverge in plastic deformation, with lower density samples showing reduced mechanical strength and earlier failure. This underscores the significance of density optimization in enhancing material properties for 316L stainless steel with copper. These findings highlight the significance of controlling porosity in AM processes, as increased porosity may compromise structural integrity and diminish load-bearing capacity. Pores can act as stress concentrators, as initiation sites for crack propagation, especially under tensile stress. Consequently, optimizing processing parameters to reduce porosity can markedly enhance the material's mechanical properties, thereby improving its overall durability and strength.

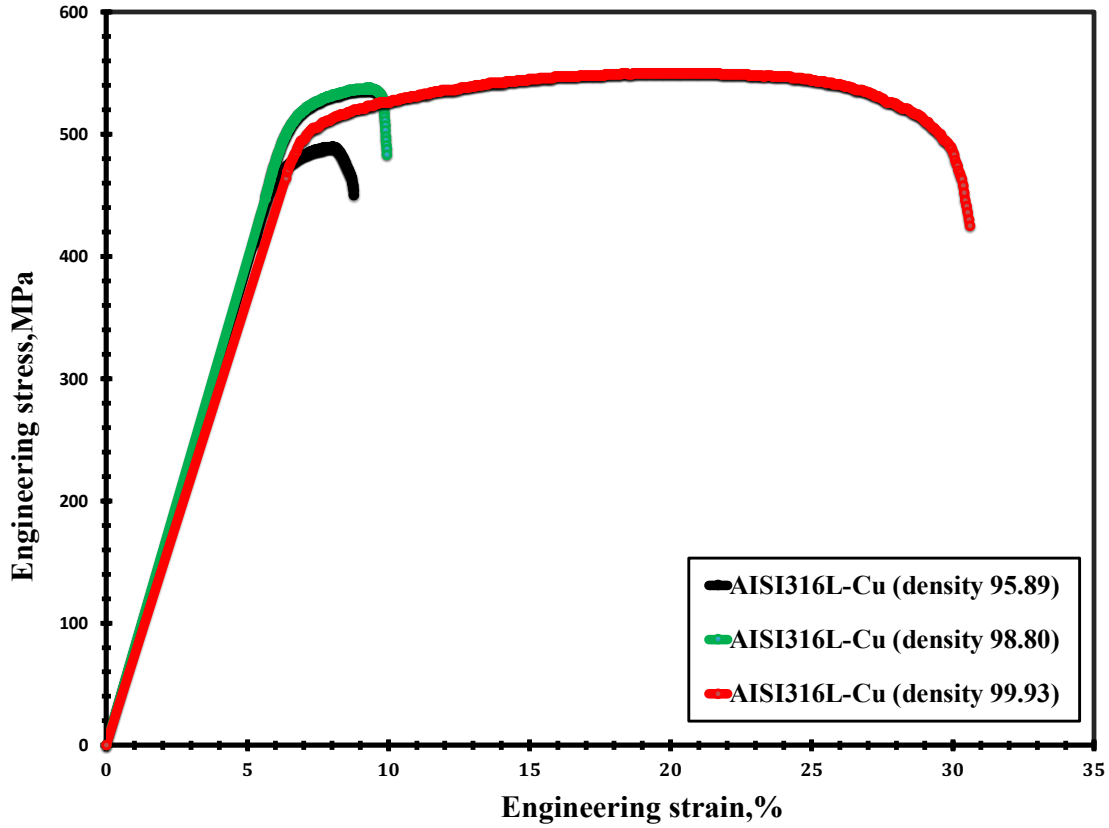

Fig. 64.Tensile stress-strain curves for samples with different porosity levels.

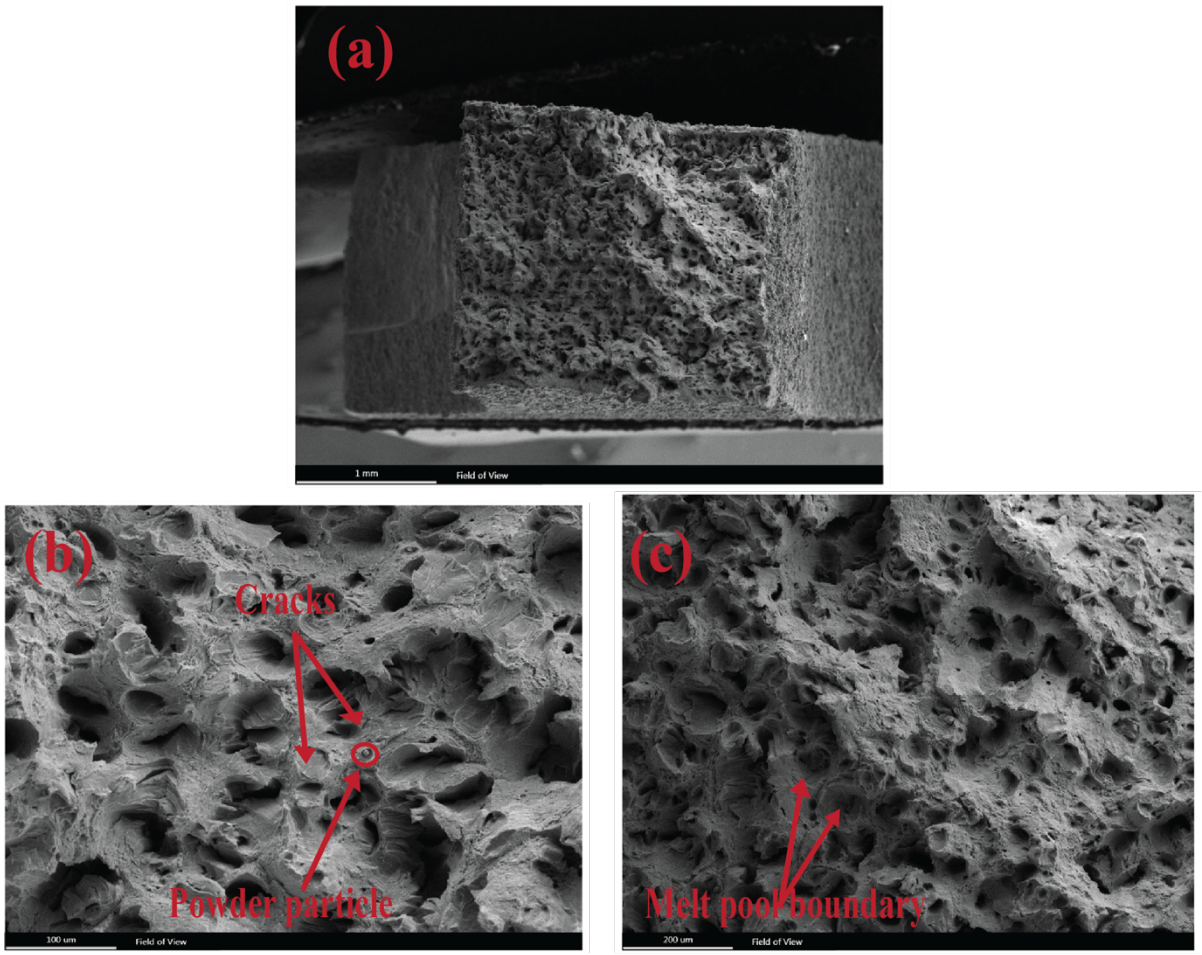

Fig. 65. Fracture surfaces of the AISI 316L-2.5% Cu samples

The fracture surface morphology of AISI316L-Cu samples post tensile testing at ambient temperature is depicted in Fig. 65. A comprehensive analysis of the fracture surface indicates a ductile fracture marked by dimple networks, corroborating the 22.4% elongation noted in the as-built sample with a relative density of 99,93%, alongside areas of brittle fracture displaying protrusions (Fig. 65(b)). A quasi-cleavage plane, possibly indicating the boundaries of the melt pool, is observable between the layered structures (Fig. 65(c)). The boundaries of these melt pools exhibit inadequate interfacial bonding, rendering them probable locations for crack initiation and sample failure under tensile stresses. Various dimples of differing sizes are evident on the fracture surface, corresponding to the intra-granular cellular structures (Fig. 65(b)). Furthermore, Fig. 65(b) illustrates an unmelted spherical powder particle and cracks along the boundaries of the melt pool, which developed during the testing procedure. These particles are recognized for promoting crack propagation under tensile stresses. The L-PBF process has been extensively documented to allow partially melted or unmelted powder particles to exist between melt pools, thereby compromising the overall mechanical strength of the samples[202]. During tensile testing, these particles often dislodge, forming crater-like voids that are considerably larger than standard dimples on the fracture surface. However, optimizing the L-PBF processing parameters can reduce these defects and significantly

improve the material's mechanical properties.Analysis of additional mechanical properties indicators, including elongation, yield strength, and ultimate tensile strength (UTS), reveals that the deterioration of mechanical qualities correlates directly with the increase in porosity. The ultimate tensile strength, yield strength, and elongation, which collectively show mechanical performance, are all shown to decrease with increasing porosity, as represented in Fig. 66.

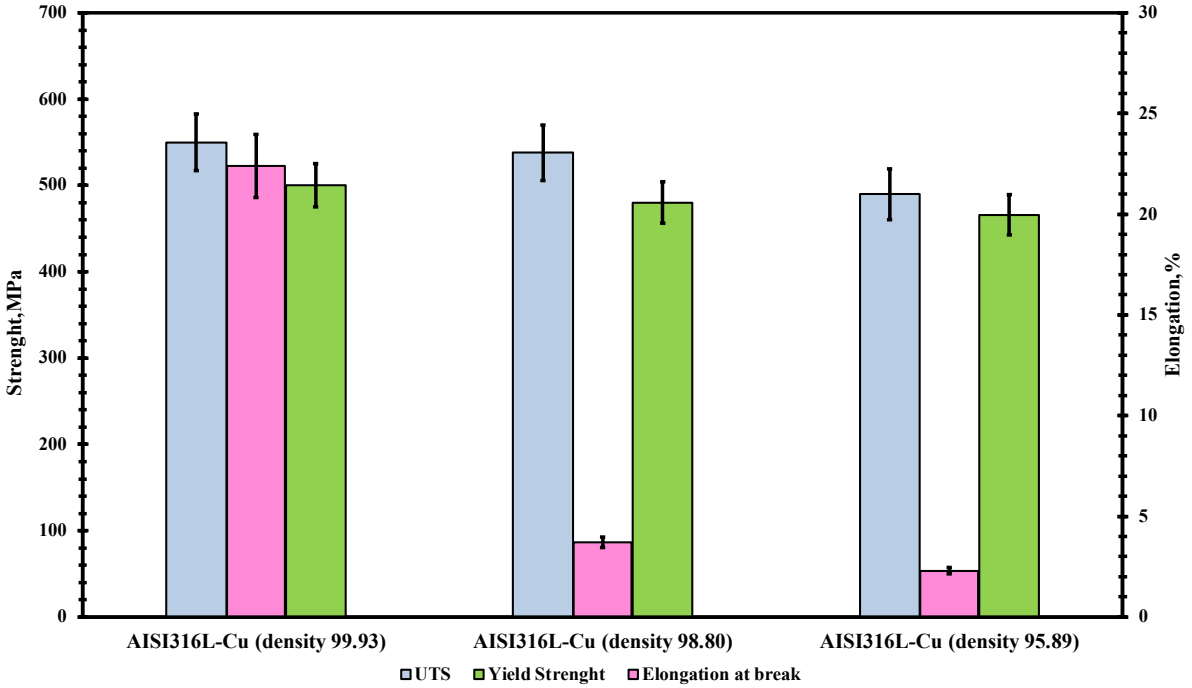

Fig. 66. Effect of Increasing Porosity on UTS, Yield Strength, and Elongation in Additively Manufactured Samples

5. Conclusion and Future Perspective

In the future, 3D printing is expected to become more diverse and application-focused in terms of materials, departing from traditional perspectives. This shift is driven by increased willingness and the availability of a broader range of materials. Industries, such as aerospace and automotive, are increasingly turning to 3D printing to develop materials that meet their specific needs. Designers can now choose materials specifically tailored to their applications to evaluate printability, complexity, time, cost, raw materials, model size, and geometry for prototypes or manufacturing. To address this, GA(Genetic Algorithms) and genetics-based ML methods optimize these multi-indicators and minimize complexity. GA is preferred due to its ability to handle extensive data in binary string format [203].

As discussed in this thesis, addressing the challenges of applying ML algorithms in AM involves overcoming limitations related to specific machines, materials, and process parameters. A crucial research gap is the need to generalize these ML models to broader contexts, necessitating further investigation. Additionally, even though the data used in these algorithms is often voluminous, it may prove insufficient. Various sensors on AM machines can be combined to improve defect detection and accuracy for monitoring goals, yet this introduces new challenges. Handling diverse and high-volume sensor data requires the development of novel ML algorithms. Consequently, the following research directions are proposed to enhance the use of ML techniques for real-time monitoring and control of AM processes.

5.1. Sensor Development

To ensure timely corrective actions are taken in AM, it is essential to have a prompt response when employing the ML model for real-time control [21]. As a solution, it has been proposed to create an intelligent sensor that can leverage "Big Data" analytics and facilitate AM integration into the Industry 4.0 framework [204]. Moreover, computational tools and algorithms are essential for operating newly developing sensing platforms. These tools enable the platforms to perform better than earlier sensor technologies in terms of cost, resolution, size, and sensitivity, among other factors [204]. Furthermore, it is important to emphasize that the benefits are reciprocal (Fig. 67); using ML algorithms can enable an iterative design process that rectifies inconsistencies in prototype sensors as they transfer to large-scale manufacture [205], further paving toward acquiring high-quality data.

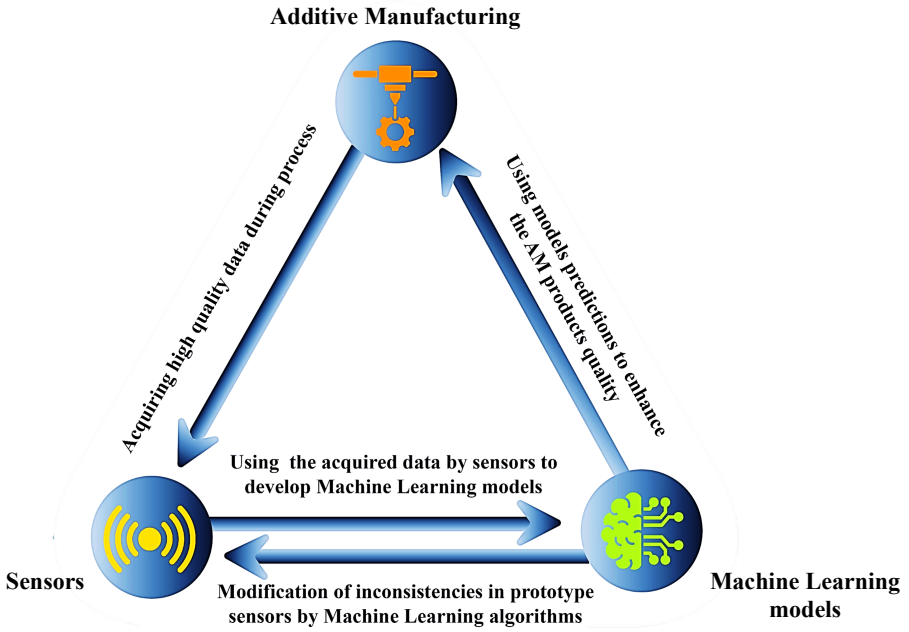

Fig. 67. The mutual benefits sensors and ML models may offer to enhance the quality of metal AM.

This thesis provides an in-depth overview of the current research on machine learning in laser-based AM processes such as L-PBF. It examines the key issues, focusing on application case studies, methodologies, and model development. Conducting a thorough thesis of the current literature on the applications of ML in L-PBF reveals that researchers are exploring innovative approaches, including data-driven techniques, to address time and cost-related issues. According to this thesis conducted on the applications of ML in process parameter optimization, the following outcomes can be drawn:

1. Following the assessment of multiple machine learning models, the SVR algorithm was determined to be the most effective for predicting process parameter defect detection relationship of samples generated by LPBF. The SVR model attained high accuracy and reliability with an optimal data division of 80% for training and 20% for testing, demonstrated by its low MAE, MSE, and high R^2 value. The model facilitated precise predictions of relative density based on VED, thereby optimizing process parameters to minimize material consumption, production duration, and expenses.

2. The analysis demonstrated that scan speed significantly affects densification, with 800 mm/s recognized as the optimal speed for attaining high relative density under specific power and hatch distance parameters. The selection of optimal process parameters enhances sustainable manufacturing by reducing porosity and increasing material efficiency.

3. Microstructural observations reveal that the columnar type of grains and fine cell structures formed along the building direction.

4. Increased energy densities yield deeper melt pools with coarser grains, whereas decreased energy densities generate shallower melt pools with finer grains. This illustrates that attaining an optimal equilibrium in process parameters is crucial for improving material properties, including strength and density, in the final component.

5. The tensile test analysis of AISI316L-Cu samples demonstrates that porosity substantially affects mechanical properties, with increased porosity resulting in reduced tensile strength, yield strength, and elongation. The sample exhibiting the lowest porosity attained the highest tensile strength, highlighting the significance of density optimization in additive manufacturing.

It is noteworthy that ML alone cannot address every problem. It is crucial to identify the specific conditions and contexts in which ML is advantageous and select the appropriate algorithm to address the issue. Although there are many promising applications, using ML to improve the production process of L-PBF still faces numerous challenges. Overcoming these obstacles will require further investigation

6. References

1. Saboori A, Aversa A, Marchese G, Biamino S, Lombardi M, Fino P. Application of directed energy deposition-based additive manufacturing in repair. Appl Sci. 2019;9(16):3316.
2. Rinaldi M, Ghidini T, Cecchini F, Brandao A, Nanni F. Additive layer manufacturing of poly (ether ether ketone) via FDM. Compos Part B Eng. 2018;145:162–72.
3. Mosallanejad MH, Niroumand B, Aversa A, Saboori A. In-situ alloying in laser-based additive manufacturing processes: A critical review. J Alloys Compd. 2021;872:159567.
4. Carrozza A, Marchese G, Saboori A, Bassini E, Aversa A, Bondioli F, et al. Effect of Aging and Cooling Path on the Super β-Transus Heat-Treated Ti-6Al-4V Alloy Produced via Electron Beam Melting (EBM). Vol. 15, Materials. 2022.
5. Bandekhoda MR, Mosallanejad MH, Atapour M, Iuliano L, Saboori A. Investigation on the Potential of Laser and Electron Beam Additively Manufactured Ti–6Al–4V Components for Orthopedic Applications. Met Mater Int. 2024;30(1):114–26.
6. Zhu Y, Zou J, Yang H yong. Wear performance of metal parts fabricated by selective laser melting: a literature review. J Zhejiang Univ A. 2018;19(2):95–110.
7. Liu K, Gu D, Guo M, Sun J. Effects of processing parameters on densification behavior, microstructure evolution and mechanical properties of W–Ti alloy fabricated by laser powder bed fusion. Mater Sci Eng A. 2022;829:142177.
8. Calignano F. Investigation of the accuracy and roughness in the laser powder bed fusion process. Virtual Phys Prototyp. 2018;13(2):97–104.
9. Eliasu A, Duntu SH, Hukpati KS, Amegadzie MY, Agyapong J, Tetteh F, et al. Effect of individual printing parameters on residual stress and tribological behaviour of 316L stainless steel fabricated with laser powder bed fusion (L-PBF). Int J Adv Manuf Technol. 2022;119(11):7041–61.
10. Milewski JO. Additive Manufacturing of Metals: From Fundamental Technology to Rocket Nozzles, Medical Implants, and Custom Jewelry. Addit Manuf Met. 2017;
11. Zhang M, Liu C, Shi X, Chen X, Chen C, Zuo J, et al. Residual stress, defects and grain morphology of Ti-6Al-4V alloy produced by ultrasonic impact treatment assisted selective laser melting. Appl Sci. 2016;6(11):304.
12. Ansarian I, Taghiabadi R, Amini S, Mosallanejad MH, Iuliano L, Saboori A. Improvement of Surface Mechanical and Tribological Characteristics of L-PBF Processed Commercially Pure Titanium through Ultrasonic Impact Treatment. Acta Metall Sin (English Lett. 2024;37(6):1034–46.
13. Patel S, Vlasea M. Melting modes in laser powder bed fusion. Materialia. 2020;9:100591.
14. Oliveira JP, LaLonde AD, Ma J. Processing parameters in laser powder bed fusion metal additive manufacturing. Mater Des. 2020;193:108762.
15. Marrey M, Malekipour E, El-Mounayri H, Faierson EJ. A framework for optimizing process parameters in powder bed fusion (PBF) process using artificial neural network (ANN). Procedia Manuf. 2019;34:505–15.

16. Frazier WE. Metal additive manufacturing: a review. J Mater Eng Perform. 2014;23:1917–28.
17. Johnson NS, Vulimiri PS, To AC, Zhang X, Brice CA, Kappes BB, et al. Invited review: Machine learning for materials developments in metals additive manufacturing. Addit Manuf. 2020;36.
18. DebRoy T, Wei HL, Zuback JS, Mukherjee T, Elmer JW, Milewski JO, et al. Additive manufacturing of metallic components – Process, structure and properties. Vol. 92, Progress in Materials Science. Pergamon; 2018. p. 112–224.
19. Sarker IH. AI-Based Modeling: Techniques, Applications and Research Issues Towards Automation, Intelligent and Smart Systems. SN Computer Science, Vol. 3. 2022.
20. Liu J, Ye J, Silva Izquierdo D, Vinel A, Shamsaei N, Shao S. A review of machine learning techniques for process and performance optimization in laser beam powder bed fusion additive manufacturing. J Intell Manuf. 2022;
21. Qi X, Chen G, Li Y, Cheng X, Li C. Applying Neural-Network-Based Machine Learning to Additive Manufacturing: Current Applications, Challenges, and Future Perspectives. Engineering. 2019 Aug 1;5(4):721–9.
22. Gupta P, Krishna C, Rajesh R, Ananthakrishnan A, Vishnuvardhan A, Patel SS, et al. Industrial internet of things in intelligent manufacturing: a review, approaches, opportunities, open challenges, and future directions. Int J Interact Des Manuf [Internet]. 2022; Available from: https://doi.org/10.1007/s12008-022-01075-w
23. Geron A. Handson Machine Learning with Scikitlearn, Keras & TensorFlow. o'Reiley Media. Inc, Sebatopol, CA. 2019;
24. Meng L, McWilliams B, Jarosinski W, Park HY, Jung YG, Lee J, et al. Machine Learning in Additive Manufacturing: A Review. JOM. 2020;72(6):2363–77.
25. Wang C, Tan XP, Tor SB, Lim CS. Machine learning in additive manufacturing: State-of-the-art and perspectives. Addit Manuf. 2020;36:101538.
26. Yuan B, Guss GM, Wilson AC, Hau-Riege SP, DePond PJ, McMains S, et al. Machine-Learning-Based Monitoring of Laser Powder Bed Fusion. Adv Mater Technol. 2018 Dec;3(12):1800136.
27. Scime L, Beuth J. Anomaly detection and classification in a laser powder bed additive manufacturing process using a trained computer vision algorithm. Addit Manuf. 2018;19:114–26.
28. Pandiyan V, Drissi-Daoudi R, Shevchik S, Masinelli G, Le-Quang T, Logé R, et al. Semi-supervised Monitoring of Laser powder bed fusion process based on acoustic emissions. Virtual Phys Prototyp. 2021;16(4):481–97.
29. Era IZ, Farahani MA, Wuest T, Liu Z. Machine learning in Directed Energy Deposition (DED) additive manufacturing: A state-of-the-art review. Manuf Lett. 2023;35:689–700.
30. Li S, Chen B, Tan C, Song X. In situ identification of laser directed energy deposition condition based on acoustic emission. Opt Laser Technol. 2024;169.
31. Zhang Z, Liu Z, Wu D. Prediction of melt pool temperature in directed energy deposition using machine learning. Addit Manuf. 2021;37.
32. Sutton RS, Barto AG. Reinforcement learning: An introduction. MIT press; 2018.

33. DebRoy T, Mukherjee T, Milewski JO, Elmer JW, Ribic B, Blecher JJ, et al. Scientific, technological and economic issues in metal printing and their solutions. Nat Mater [Internet]. 2019;18(10):1026–32. Available from: https://doi.org/10.1038/s41563-019-0408-2
34. Bose S, Ke D, Sahasrabudhe H, Bandyopadhyay A. Additive manufacturing of biomaterials. Prog Mater Sci. 2018 Apr 1;93:45–111.
35. Shinde MS, Ashtankar KM. Additive manufacturing–assisted conformal cooling channels in mold manufacturing processes. Adv Mech Eng [Internet]. 2017 May 1;9(5):1687814017699764. Available from: https://doi.org/10.1177/1687814017699764
36. Qi D, Yu H, Liu M, Huang H, Xu S, Xia Y, et al. Mechanical behaviors of SLM additive manufactured octet-truss and truncated-octahedron lattice structures with uniform and taper beams. Int J Mech Sci [Internet]. 2019;163:105091. Available from: https://www.sciencedirect.com/science/article/pii/S0020740319319587
37. Technologies ACF on AM, Terminology ACF on AMTSF 91 on. Standard terminology for additive manufacturing technologies. Astm International; 2012.
38. Wang Q, Zhang S, Zhang C, Wu C, Wang J, Chen J, et al. Microstructure evolution and EBSD analysis of a graded steel fabricated by laser additive manufacturing. Vacuum [Internet]. 2017;141:68–81. Available from: https://www.sciencedirect.com/science/article/pii/S0042207X17300507
39. Liu ZC, Jiang Q, Li T, Dong S, Yan S, Zhang HC, et al. Environmental benefits of remanufacturing: A case study of cylinder heads remanufactured through laser cladding. J Clean Prod. 2016 Jun 1;133.
40. Dass A, Moridi A. State of the Art in Directed Energy Deposition: From Additive Manufacturing to Materials Design. Coatings. 2019 Jun 29;9:418.
41. Ahn DG. Directed Energy Deposition (DED) Process: State of the Art. Int J Precis Eng Manuf Technol. 2021 Feb 15;8.
42. Khanzadeh M, Chowdhury S, Tschopp M, Doude H, Marufuzzaman M, Bian L. In-Situ Monitoring of Melt Pool Images for Porosity Prediction in Directed Energy Deposition Processes. IISE Trans. 2017 Dec 14;51.
43. Thompson SM, Bian L, Shamsaei N, Yadollahi A. An overview of Direct Laser Deposition for additive manufacturing; Part I: Transport phenomena, modeling and diagnostics. Addit Manuf [Internet]. 2015;8:36–62. Available from: https://www.sciencedirect.com/science/article/pii/S2214860415000317
44. Rahmati S. 10.12 - Direct Rapid Tooling. In: Hashmi S, Batalha GF, Van Tyne CJ, Yilbas BBTCMP, editors. Oxford: Elsevier; 2014. p. 303–44. Available from: https://www.sciencedirect.com/science/article/pii/B978008096532101013X
45. Elmer J, GIBBS G, CARPENTER J, COUGHLIN D, HOCHANADEL PAT, VAJA JAY, et al. Wire-Based Additive Manufacturing of Stainless Steel Components. Weld J. 2020 Jan 1;99:8–24.
46. Gu D, Shen Y. Balling phenomena in direct laser sintering of stainless steel powder: Metallurgical mechanisms and control methods. Mater Des [Internet]. 2009;30(8):2903–10. Available from: https://www.sciencedirect.com/science/article/pii/S0261306909000181

47. Song YU, Song BU, Jung MK, Lee C, Choi JP, Lee I. Multi-fidelity Gaussian process modeling of a thin-walled structure for laser powder bed fusion (LPBF) process window. J Manuf Process [Internet]. 2024;127:107–14. Available from: https://www.sciencedirect.com/science/article/pii/S1526612524007394
48. Abd-Elaziem W, Elkatatny S, Abd-Elaziem AE, Khedr M, Abd El-baky MA, Hassan MA, et al. On the current research progress of metallic materials fabricated by laser powder bed fusion process: a review. J Mater Res Technol [Internet]. 2022;20:681–707. Available from: https://www.sciencedirect.com/science/article/pii/S2238785422011243
49. Sames WJ, List FA, Pannala S, Dehoff RR, Babu SS. The metallurgy and processing science of metal additive manufacturing. Int Mater Rev [Internet]. 2016;61(5):315–60. Available from: https://doi.org/10.1080/09506608.2015.1116649
50. Lannunziata E, Zapparoli N, Iuliano L, Saboori A. Effect of powder atomising route on the surface quality and mechanical performance of AISI 316L samples produced via laser powder bed fusion process. Procedia CIRP [Internet]. 2023;118:688–93. Available from: https://www.sciencedirect.com/science/article/pii/S2212827123003451
51. Mukherjee T, DebRoy T. A digital twin for rapid qualification of 3D printed metallic components. Appl Mater Today [Internet]. 2019;14:59–65. Available from: https://www.sciencedirect.com/science/article/pii/S2352940718304931
52. Donoghue J, Antonysamy AA, Martina F, Colegrove PA, Williams SW, Prangnell PB. The effectiveness of combining rolling deformation with Wire–Arc Additive Manufacture on β-grain refinement and texture modification in Ti–6Al–4V. Mater Charact [Internet]. 2016;114:103–14. Available from: https://www.sciencedirect.com/science/article/pii/S1044580316300262
53. Koike M, Greer P, Owen K, Lilly G, Murr L, Gaytan S, et al. Evaluation of Titanium Alloys Fabricated Using Rapid Prototyping Technologies---Electron Beam Melting and Laser Beam Melting. Materials (Basel). 2011 Dec 1;4.
54. Vayssette B, Saintier N, Brugger C, Elmay M, Pessard E. Surface roughness of Ti-6Al-4V parts obtained by SLM and EBM: Effect on the High Cycle Fatigue life. Procedia Eng [Internet]. 2018;213:89–97. Available from: https://www.sciencedirect.com/science/article/pii/S1877705818302327
55. Antonysamy AA, Meyer J, Prangnell PB. Effect of build geometry on the β-grain structure and texture in additive manufacture of Ti6Al4V by selective electron beam melting. Mater Charact. 2013;84:153–68.
56. Chowdhury S, Yadaiah N, Prakash C, Ramakrishna S, Dixit S, Gupta LR, et al. Laser powder bed fusion: a state-of-the-art review of the technology, materials, properties & defects, and numerical modelling. J Mater Res Technol. 2022;20:2109–72.
57. Ataee A, Li Y, Song G, Wen C. Metal scaffolds processed by electron beam melting for biomedical applications. In: Metallic Foam Bone. Elsevier; 2017. p. 83–110.
58. Singh S. Implant Materials and Their Processing Technologies. In: Reference Module in Materials Science and Materials Engineering. 2016.
59. Oshida Y. Bioscience and bioengineering of titanium materials. Elsevier; 2010.
60. Zhang LC, Liu Y, Li S, Hao Y. Additive Manufacturing of Titanium Alloys by

Electron Beam Melting: A Review. Adv Eng Mater [Internet]. 2018;20(5):1700842. Available from: https://doi.org/10.1002/adem.201700842
61. Gao W, Zhang Y, Ramanujan D, Ramani K, Chen Y, Williams C, et al. The Status, Challenges, and Future of Additive Manufacturing in Engineering. Comput Des. 2015 Apr 17;69.
62. Francois MM, Sun A, King WE, Henson NJ, Tourret D, Bronkhorst CA, et al. Modeling of additive manufacturing processes for metals: Challenges and opportunities. Curr Opin Solid State Mater Sci. 2017 Aug;21(4):198–206.
63. Zhang Y, Gao X, Katayama S. Weld appearance prediction with BP neural network improved by genetic algorithm during disk laser welding. J Manuf Syst [Internet]. 2015;34:53–9. Available from: https://www.sciencedirect.com/science/article/pii/S0278612514001149
64. Taghian M, Mosallanejad MH, Lannunziata E, Del Greco G, Iuliano L, Saboori A. Laser powder bed fusion of metallic components: Latest progress in productivity, quality, and cost perspectives. J Mater Res Technol. 2023;27:6484–500.
65. Yasa E, Kruth JP, Deckers J. Manufacturing by combining selective laser melting and selective laser erosion/laser re-melting. CIRP Ann. 2011;60(1):263–6.
66. Sarkon GK, Safaei B, Kenevisi MS, Arman S, Zeeshan Q. State-of-the-Art Review of Machine Learning Applications in Additive Manufacturing; from Design to Manufacturing and Property Control. Arch Comput Methods Eng. 2022;29(7):5663–721.
67. Learned-Miller EG. Introduction to supervised learning. I Dep Comput Sci Univ Massachusetts. 2014;3.
68. Dedeloudi A, Weaver E, Lamprou DA. Machine learning in additive manufacturing & Microfluidics for smarter and safer drug delivery systems. Int J Pharm [Internet]. 2023;636:122818. Available from: https://www.sciencedirect.com/science/article/pii/S0378517323002387
69. Singh D, Singh B. Investigating the impact of data normalization on classification performance. Appl Soft Comput. 2020;97:105524.
70. Kumar S, Gopi T, Harikeerthana N, Gupta MK, Gaur V, Krolczyk GM, et al. Machine learning techniques in additive manufacturing: a state of the art review on design, processes and production control. J Intell Manuf. 2023;34(1):21–55.
71. Parsazadeh M, Sharma S, Dahotre N. Towards the next generation of machine learning models in additive manufacturing: A review of process dependent material evolution. Prog Mater Sci. 2023;135.
72. Eshkabilov S, Ara I, Azarmi F. A comprehensive investigation on application of machine learning for optimization of process parameters of laser powder bed fusion-processed 316L stainless steel. Int J Adv Manuf Technol. 2022;123(7):2733–56.
73. Peng X, Wu S, Qian W, Bao J, Hu Y, Zhan Z, et al. The potency of defects on fatigue of additively manufactured metals. Int J Mech Sci. 2022;221:107185.
74. Caiazzo F, Caggiano A. Laser Direct Metal Deposition of 2024 Al Alloy: Trace Geometry Prediction via Machine Learning. Vol. 11, Materials. 2018.
75. Khanzadeh M, Chowdhury S, Marufuzzaman M, Tschopp M, Bian L. Porosity prediction: Supervised-learning of thermal history for direct laser deposition. J Manuf

Syst. 2018 Apr;47:69–82.
76. Bridgelall R. Tutorial on Support Vector Machines. 2022;
77. Tripathi S, Hemachandra N. Scalable linear classifiers based on exponential loss function. In: Proceedings of the ACM India Joint International Conference on Data Science and Management of Data. 2018. p. 190–200.
78. Duchi JC. CS 229 Supplemental Lecture notes Hoeffding ' s inequality. In 2016.
79. Krizhevsky A, Sutskever I, Hinton GE. ImageNet Classification with Deep Convolutional Neural Networks. In: Pereira F, Burges CJ, Bottou L, Weinberger KQ, editors. Advances in Neural Information Processing Systems [Internet]. Curran Associates, Inc.; 2012. Available from: https://proceedings.neurips.cc/paper_files/paper/2012/file/c399862d3b9d6b76c8436e924a68c45b-Paper.pdf
80. Nguyen VM, Chau VT. Enhancing the Dynamic Stability of Pylons via Their Drag and Lift Coefficients by Finite Volume Method. Buildings. 2023;13(5):1120.
81. Saha S. A Comprehensive Guide to Convolutional Neural Networks: The ELI5 Way.
82. Fu Y, Downey ARJ, Yuan L, Zhang T, Pratt A, Balogun Y. Machine learning algorithms for defect detection in metal laser-based additive manufacturing: A review. Vol. 75, Journal of Manufacturing Processes. Elsevier; 2022. p. 693–710.
83. Michau G, Fink O. Unsupervised transfer learning for anomaly detection: Application to complementary operating condition transfer. Knowledge-Based Syst. 2021;216:106816.
84. Shi Z, Mamun A Al, Kan C, Tian W, Liu C. An LSTM-autoencoder based online side channel monitoring approach for cyber-physical attack detection in additive manufacturing. J Intell Manuf. 2023;34(4):1815–31.
85. Scime L, Beuth J. Anomaly Detection and Classification in a Laser Powder Bed Additive Manufacturing Process using a Trained Computer Vision Algorithm. Addit Manuf. 2017 Nov;19.
86. Donegan SP, Schwalbach EJ, Groeber MA. Zoning additive manufacturing process histories using unsupervised machine learning. Mater Charact. 2020;161:110123.
87. Snell R, Tammas-Williams S, Chechik L, Lyle A, Hernández-Nava E, Boig C, et al. Methods for Rapid Pore Classification in Metal Additive Manufacturing. JOM. 2020;72(1):101–9.
88. Singh A, Nowak R, Zhu J. Unlabeled data: Now it helps, now it doesn't. Adv Neural Inf Process Syst. 2008;21.
89. Okaro IA, Jayasinghe S, Sutcliffe C, Black K, Paoletti P, Green PL. Automatic fault detection for laser powder-bed fusion using semi-supervised machine learning. Addit Manuf. 2019;27(January):42–53.
90. Van Engelen JE, Hoos HH. A survey on semi-supervised learning. Mach Learn. 2020;109(2):373–440.
91. Sutton RS. Introduction: The challenge of reinforcement learning. In: Reinforcement learning. Springer; 1992. p. 1–3.
92. Yoon J, Arik S, Pfister T. Data valuation using reinforcement learning. In: International Conference on Machine Learning. PMLR; 2020. p. 10842–51.
93. Ryo M, Rillig MC. Statistically reinforced machine learning for nonlinear patterns and

variable interactions. Ecosphere. 2017;8(11):e01976.
94. Mahmoud D, Magolon M, Boer J, Elbestawi MA, Mohammadi MG. Applications of machine learning in process monitoring and controls of l-pbf additive manufacturing: A review. Vol. 11, Applied Sciences (Switzerland). 2021.
95. Wasmer K, Le Quang T, Meylan B, Shevchik S. In Situ Quality Monitoring in AM Using Acoustic Emission: A Reinforcement Learning Approach. J Mater Eng Perform. 2019 Feb;28:666–72.
96. Knaak C, Masseling L, Duong E, Abels P, Gillner A. Improving Build Quality in Laser Powder Bed Fusion Using High Dynamic Range Imaging and Model-Based Reinforcement Learning. IEEE Access. 2021 Mar;PP:1.
97. Zhang Y, Wu L, Guo X, Kane S, Deng Y, Jung YG, et al. Additive Manufacturing of Metallic Materials: A Review. J Mater Eng Perform. 2018;27(1):1–13.
98. Qin J, Hu F, Liu Y, Witherell P, Wang CCL, Rosen DW, et al. Research and application of machine learning for additive manufacturing. Addit Manuf. 2022 Apr 1;52:102691.
99. Mahmoudi M, Aziz Ezzat A, Elwany A. Layerwise Anomaly Detection in Laser Powder-Bed Fusion Metal Additive Manufacturing. J Manuf Sci Eng. 2018 Nov 28;141.
100. Zhang Y, Hong GS, Ye D, Zhu K, Fuh JYH. Extraction and evaluation of melt pool, plume and spatter information for powder-bed fusion AM process monitoring. Mater Des [Internet]. 2018; Available from: https://api.semanticscholar.org/CorpusID:139675708
101. Ren Z, Gao L, Clark SJ, Fezzaa K, Shevchenko P, Choi A, et al. Machine learning–aided real-time detection of keyhole pore generation in laser powder bed fusion. Science (80-). 2023 Jan;379(6627):89–94.
102. Li W, Lambert-Garcia R, Getley ACM, Kim K, Bhagavath S, Majkut M, et al. AM-SegNet for additive manufacturing in situ X-ray image segmentation and feature quantification. Virtual Phys Prototyp. 2024 Dec;19(1).
103. Chen R, Sodhi M, Imani M, Khanzadeh M, Yadollahi A, Imani F. Brain-inspired computing for in-process melt pool characterization in additive manufacturing. CIRP J Manuf Sci Technol. 2023 Apr;41:380–90.
104. Grasso M, Laguzza V, Semeraro Q, Colosimo BM. In-process monitoring of selective laser melting: spatial detection of defects via image data analysis. J Manuf Sci Eng. 2017;139(5):51001.
105. Yadav P, Singh VK, Joffre T, Rigo O, Arvieu C, Le Guen E, et al. Inline Drift Detection Using Monitoring Systems and Machine Learning in Selective Laser Melting. Adv Eng Mater. 2020;22(12).
106. Baumgartl H, Tomas J, Buettner R, Merkel M. A deep learning-based model for defect detection in laser-powder bed fusion using in-situ thermographic monitoring. Prog Addit Manuf. 2020;5(3):277–85.
107. Williams J, Dryburgh P, Clare A, Rao P, Samal A. Defect Detection and Monitoring in Metal Additive Manufactured Parts through Deep Learning of Spatially Resolved Acoustic Spectroscopy Signals. Smart Sustain Manuf Syst. 2018 Nov 19;2:20180035.
108. Dongsen Y, Fuh J, Zhang Y, Hong GS, Zhu K. Defects Recognition in Selective Laser

Melting with Acoustic Signals by SVM Based on Feature Reduction. IOP Conf Ser Mater Sci Eng. 2018 Oct;436:12020.
109. Gobert C, Reutzel EW, Petrich J, Nassar AR, Phoha S. Application of supervised machine learning for defect detection during metallic powder bed fusion additive manufacturing using high resolution imaging. Addit Manuf. 2018;21:517–28.
110. Caggiano A, Zhang J, Alfieri V, Caiazzo F, Gao R, Teti R. Machine learning-based image processing for on-line defect recognition in additive manufacturing. CIRP Ann. 2019;68(1):451–4.
111. Scime L, Beuth J. A multi-scale convolutional neural network for autonomous anomaly detection and classification in a laser powder bed fusion additive manufacturing process. Addit Manuf. 2018;24:273–86.
112. Mojahed Yazdi R, Imani F, Yang H. A hybrid deep learning model of process-build interactions in additive manufacturing. J Manuf Syst. 2020;57:460–8.
113. Gaikwad A, Imani F, Yang H, Reutzel EW, Rao P. In Situ Monitoring of Thin-Wall Build Quality in Laser Powder Bed Fusion Using Deep Learning. Smart Sustain Manuf Syst. 2019 Nov;3.
114. Imani F, Gaikwad A, Montazeri M, Rao P, Yang H, Reutzel E. Process mapping and in-process monitoring of porosity in laser powder bed fusion using layerwise optical imaging. J Manuf Sci Eng. 2018;140(10):101009.
115. Yuan B, Giera B, Guss G, Matthews I, McMains S. Semi-Supervised Convolutional Neural Networks for In-Situ Video Monitoring of Selective Laser Melting. 2019 IEEE Winter Conf Appl Comput Vis [Internet]. 2019;744–53. Available from: https://api.semanticscholar.org/CorpusID:71152364
116. Okaro IA, Jayasinghe S, Sutcliffe C, Black K, Paoletti P, Green PL. Automatic fault detection for laser powder-bed fusion using semi-supervised machine learning. Addit Manuf. 2019;27:42–53.
117. Montazeri M, Nassar AR, Dunbar AJ, Rao P. In-process monitoring of porosity in additive manufacturing using optical emission spectroscopy. IISE Trans. 2020;52(5):500–15.
118. Seifi SH, Tian W, Doude H, Tschopp M, Bian L. Layer-Wise Modeling and Anomaly Detection for Laser-Based Additive Manufacturing. J Manuf Sci Eng. 2019 May;141:1.
119. Guo W, Tian Q, Guo S, Guo Y. A physics-driven deep learning model for process-porosity causal relationship and porosity prediction with interpretability in laser metal deposition. CIRP Ann. 2020 May;69.
120. Gaja H, Liou F. Defect classification of laser metal deposition using logistic regression and artificial neural networks for pattern recognition. Int J Adv Manuf Technol. 2018 Jan;94.
121. Khanzadeh M, Chowdhury S, Tschopp MA, Doude HR, Marufuzzaman M, Bian L. In-situ monitoring of melt pool images for porosity prediction in directed energy deposition processes. IISE Trans [Internet]. 2019 May 4;51(5):437–55. Available from: https://doi.org/10.1080/24725854.2017.1417656
122. Jafari-Marandi R, Khanzadeh M, Tian W, Smith B, Bian L. From in-situ monitoring toward high-throughput process control: cost-driven decision-making framework for

laser-based additive manufacturing. J Manuf Syst [Internet]. 2019;51:29–41. Available from: https://www.sciencedirect.com/science/article/pii/S0278612518302929
123. Francis J, Bian L. Deep Learning for Distortion Prediction in Laser-Based Additive Manufacturing using Big Data. Manuf Lett [Internet]. 2019;20:10–4. Available from: https://www.sciencedirect.com/science/article/pii/S221384631830172X
124. Zhang B, Liu S, Shin YC. In-Process monitoring of porosity during laser additive manufacturing process. Addit Manuf [Internet]. 2019;28:497–505. Available from: https://www.sciencedirect.com/science/article/pii/S2214860419303653
125. Gonzalez Val C, Pallas A, Panadeiro V, Rodriguez A. A convolutional approach to quality monitoring for laser manufacturing. J Intell Manuf. 2020 Mar;31.
126. Chen L, Yao X, Xu P, Moon S, Bi G. Rapid surface defect identification for additive manufacturing with in-situ point cloud processing and machine learning. Virtual Phys Prototyp. 2020 Oct;16.
127. Zhang Y, Hong GS, Dongsen Y, Fuh J, Zhu K. Powder-Bed Fusion Process Monitoring by Machine Vision With Hybrid Convolutional Neural Networks. IEEE Trans Ind Informatics. 2019 Nov 26;PP:1.
128. Tapia G, Elwany A, Sang H. Prediction of Porosity in Metal-based Additive Manufacturingusing Spatial Gaussian Process Models. Addit Manuf. 2016 May;12.
129. Minkowitz L, Arneitz S, Effertz PS, Amancio-Filho ST. Laser-powder bed fusion process optimisation of AlSi10Mg using extra trees regression. Mater Des. 2023 Mar;227:111718.
130. Mooraj S, Kim G, Fan X, Samuha S, Xie Y, Li T, et al. Additive manufacturing of defect-free TiZrNbTa refractory high-entropy alloy with enhanced elastic isotropy via in-situ alloying of elemental powders. Commun Mater. 2024 Feb;5(1):14.
131. Rankouhi B, Jahani S, Pfefferkorn FE, Thoma DJ. Compositional grading of a 316L-Cu multi-material part using machine learning for the determination of selective laser melting process parameters. Addit Manuf. 2021;38:101836.
132. Wang J, Jeong SG, Kim ES, Kim HS, Lee BJ. Material-agnostic machine learning approach enables high relative density in powder bed fusion products. Nat Commun. 2023 Oct;14(1):6557.
133. García-Moreno AI, Alvarado Orozco J, Ibarra-Medina J, Martinez Franco E. Image-based porosity classification in Al-alloys by laser metal deposition using random forests. Int J Adv Manuf Technol. 2020 Oct;110:1–19.
134. Lu ZL, Li DC, Lu BH, Zhang A, Zhu GX, Pi G. The prediction of the building precision in the Laser Engineered Net Shaping process using advanced networks. Opt Lasers Eng - OPT LASER ENG. 2010 May;48:519–25.
135. Gihr M, Rashid A, Melkote SN. Bead geometry prediction and optimization for corner structures in directed energy deposition using machine learning. Addit Manuf. 2024;84:104080.
136. Wacker C, Köhler M, David M, Aschersleben F, Gabriel F, Hensel J, et al. Geometry and Distortion Prediction of Multiple Layers for Wire Arc Additive Manufacturing with Artificial Neural Networks. Vol. 11, Applied Sciences. 2021.
137. Dang L, He X, Tang D, Xin H, Zhan Z, Wang X, et al. Pore-induced fatigue failure: A prior progressive fatigue life prediction framework of laser-directed energy deposition

Ti-6Al-4V based on machine learning. Theor Appl Fract Mech. 2024;130:104276.
138. Sohil F, Sohail M, Shabbir J. An introduction to statistical learning with applications in R: by Gareth James, Daniela Witten, Trevor Hastie, and Robert Tibshirani, New York, Springer Science and Business Media, 2013, $41.98, eISBN: 978-1-4614-7137-7. Stat Theory Relat Fields. 2021 Sep;6:1.
139. Goh GD, Sing SL, Yeong WY. A review on machine learning in 3D printing: applications, potential, and challenges. Artif Intell Rev. 2021 Jan;54.
140. Li Z, Zhang Z, Shi J, Wu D. Prediction of surface roughness in extrusion-based additive manufacturing with machine learning. Robot Comput Integr Manuf. 2019;57:488–95.
141. Tapia G, Elwany AH, Sang H. Prediction of porosity in metal-based additive manufacturing using spatial Gaussian process models. Addit Manuf. 2016;12:282–90.
142. Tapia G, Khairallah S, Matthews M, King WE, Elwany A. Gaussian process-based surrogate modeling framework for process planning in laser powder-bed fusion additive manufacturing of 316L stainless steel. Int J Adv Manuf Technol. 2018 Feb;94(9–12):3591–603.
143. Meng L, Zhang J. Process design of laser powder bed fusion of stainless steel using a Gaussian process-based machine learning model. Jom. 2020;72(1):420–8.
144. Kamath C. Data mining and statistical inference in selective laser melting. Int J Adv Manuf Technol. 2016;86:1659–77.
145. Chowdhury S, Anand S. Artificial neural network based geometric compensation for thermal deformation in additive manufacturing processes. In: International Manufacturing Science and Engineering Conference. American Society of Mechanical Engineers; 2016. p. V003T08A006.
146. Reddy NS, Panigrahi BB, Ho CM, Kim JH, Lee CS. Artificial neural network modeling on the relative importance of alloying elements and heat treatment temperature to the stability of α and β phase in titanium alloys. Comput Mater Sci. 2015;107:175–83.
147. Silbernagel C, Aremu A, Ashcroft I. Using machine learning to aid in the parameter optimisation process for metal-based additive manufacturing. Vol. ahead-of-p, Rapid Prototyping Journal. 2019.
148. Li P, Pei Y, Li J. A comprehensive survey on design and application of autoencoder in deep learning. Appl Soft Comput. 2023;138:110176.
149. Maleki E, Bagherifard S, Guagliano M. Application of artificial intelligence to optimize the process parameters effects on tensile properties of Ti-6Al-4V fabricated by laser powder-bed fusion. Int J Mech Mater Des. 2021;1–24.
150. Wang H, Li B, Zhang W, Xuan F. Microstructural feature-driven machine learning for predicting mechanical tensile strength of laser powder bed fusion (L-PBF) additively manufactured Ti6Al4V alloy. Eng Fract Mech. 2024 Jan;295:109788.
151. Scime L, Joslin C, Collins DA, Sprayberry M, Singh A, Halsey W, et al. A Data-Driven Framework for Direct Local Tensile Property Prediction of Laser Powder Bed Fusion Parts. Materials (Basel). 2023 Nov;16(23):7293.
152. Yang Z, Yang M, Sisson R, Li Y, Liang J. A machine-learning model to predict tensile properties of Ti6Al4V parts prepared by laser powder bed fusion with hot isostatic

pressing. Mater Today Commun. 2022 Dec;33:104205.
153. Minerva G, Awd M, Tenkamp J, Walther F, Beretta S. Machine learning-assisted extreme value statistics of anomalies in AlSi10Mg manufactured by L-PBF for robust fatigue strength predictions. Mater Des. 2023 Nov;235:112392.
154. Jia Y, Fu R, Ling C, Shen Z, Zheng L, Zhong Z, et al. Fatigue life prediction based on a deep learning method for Ti-6Al-4V fabricated by laser powder bed fusion up to very-high-cycle fatigue regime. Int J Fatigue. 2023 Jul;172:107645.
155. Moon S, Ma R, Attardo R, Tomonto C, Nordin M, Wheelock P, et al. Impact of surface and pore characteristics on fatigue life of laser powder bed fusion Ti–6Al–4V alloy described by neural network models. Sci Rep. 2021 Oct;11(1):20424.
156. Elangeswaran C, Cutolo A, Gallas S, Dinh TD, Lammens N, Erdelyi H, et al. Predicting fatigue life of metal LPBF components by combining a large fatigue database for different sample conditions with novel simulation strategies. Addit Manuf. 2022 Feb;50:102570.
157. Barrionuevo GO, Walczak M, Ramos-Grez J, Sánchez-Sánchez X. Microhardness and wear resistance in materials manufactured by laser powder bed fusion: Machine learning approach for property prediction. CIRP J Manuf Sci Technol. 2023 Jul;43:106–14.
158. Hassanin H, Zweiri Y, Finet L, Essa K, Qiu C, Attallah M. Laser Powder Bed Fusion of Ti-6Al-2Sn-4Zr-6Mo Alloy and Properties Prediction Using Deep Learning Approaches. Materials (Basel). 2021 Apr;14(8):2056.
159. Lesko CCC, Sheridan LC, Gockel JE. Microhardness as a Function of Process Parameters in Additively Manufactured Alloy 718. J Mater Eng Perform. 2021 Sep;30(9):6630–9.
160. Zhang T, Zhou X, Zhang P, Duan Y, Cheng X, Wang X, et al. Hardness Prediction of Laser Powder Bed Fusion Product Based on Melt Pool Radiation Intensity. Materials (Basel). 2022 Jul;15(13):4674.
161. Zhang W, Desai P. MACHINE LEARNING ENABLED POWDER SPREADING PROCESS MAP FOR METAL ADDITIVE MANUFACTURING (AM). 2017.
162. Kumar P, Jain NK. Surface roughness prediction in micro-plasma transferred arc metal additive manufacturing process using K-nearest neighbors algorithm. Int J Adv Manuf Technol. 2022;119(5):2985–97.
163. Cao Z, Liu Q, Liu Q, Yu X, Kruzic JJ, Li X. A machine learning method to quantitatively predict alpha phase morphology in additively manufactured Ti-6Al-4V. npj Comput Mater. 2023;9(1):195.
164. Özel T, Shaurya A, Altay A, Yang L. Process monitoring of meltpool and spatter for temporal-spatial modeling of laser powder bed fusion process. Procedia CIRP [Internet]. 2018;74:102–6. Available from: https://www.sciencedirect.com/science/article/pii/S2212827118308333
165. Mani M, Wong YS, Fuh JYH, Loh HT. Benchmarking for comparative evaluation of RP systems and processes. Rapid Prototyp J. 2004 Apr 1;10:123–35.
166. Zhu Z, Ferreira K, Anwer N, Mathieu L, Guo K, Qiao L. Convolutional Neural Network for geometric deviation prediction in Additive Manufacturing. Procedia CIRP [Internet]. 2020;91:534–9. Available from:

https://www.sciencedirect.com/science/article/pii/S2212827120308623
167. Estalaki SM, Lough CS, Landers RG, Kinzel EC, Luo T. Predicting defects in laser powder bed fusion using in-situ thermal imaging data and machine learning. Addit Manuf. 2022 Oct;58:103008.
168. Gobert C, Reutzel EW, Petrich J, Nassar AR, Phoha S. Application of supervised machine learning for defect detection during metallic powder bed fusion additive manufacturing using high resolution imaging. Addit Manuf. 2018;21:517–28.
169. Ye Z, Liu C, Tian W, Kan C. In-situ point cloud fusion for layer-wise monitoring of additive manufacturing. J Manuf Syst. 2021;61:210–22.
170. Kaji F, Nguyen-Huu H, Budhwani A, Narayanan JA, Zimny M, Toyserkani E. A deep-learning-based in-situ surface anomaly detection methodology for laser directed energy deposition via powder feeding. J Manuf Process. 2022;81:624–37.
171. Gaikwad A, Giera B, Guss GM, Forien JB, Matthews MJ, Rao P. Heterogeneous sensing and scientific machine learning for quality assurance in laser powder bed fusion–A single-track study. Addit Manuf. 2020;36:101659.
172. du Plessis A. Effects of process parameters on porosity in laser powder bed fusion revealed by X-ray tomography. Addit Manuf. 2019;30:100871.
173. Jiang R, Smith J, Yi YT, Sun T, Simonds BJ, Rollett AD. Deep learning approaches for instantaneous laser absorptance prediction in additive manufacturing. npj Comput Mater. 2024;10(1):6.
174. Gorgannejad S, Martin AA, Nicolino JW, Strantza M, Guss GM, Khairallah S, et al. Localized keyhole pore prediction during laser powder bed fusion via multimodal process monitoring and X-ray radiography. Addit Manuf. 2023 Sep;78:103810.
175. Sun S, Brandt M, Easton M. 2 - Powder bed fusion processes: An overview. In: Brandt MBTLAM, editor. Woodhead Publishing Series in Electronic and Optical Materials [Internet]. Woodhead Publishing; 2017. p. 55–77. Available from: https://www.sciencedirect.com/science/article/pii/B9780081004333000026
176. Thijs L, Verhaeghe F, Craeghs T, Humbeeck J Van, Kruth JP. A study of the microstructural evolution during selective laser melting of Ti–6Al–4V. Acta Mater [Internet]. 2010;58(9):3303–12. Available from: https://www.sciencedirect.com/science/article/pii/S135964541000090X
177. Sadowski M, Ladani L, Brindley W, Romano J. Optimizing quality of additively manufactured Inconel 718 using powder bed laser melting process. Addit Manuf [Internet]. 2016;11:60–70. Available from: https://www.sciencedirect.com/science/article/pii/S2214860416300483
178. Gu Z, Sharma S, Riley D, Pantawane M, Joshi S, Fu S, et al. A universal predictor-based machine learning model for optimal process maps in laser powder bed fusion process. J Intell Manuf. 2022 Aug 23;34:1–23.
179. Behjat A, Shamanian M, Iuliano L, Saboori A. Laser powder bed fusion in situ alloying of AISI 316L-2.5%Cu alloy: microstructure and mechanical properties evolution. Prog Addit Manuf [Internet]. 2024; Available from: https://doi.org/10.1007/s40964-023-00557-x
180. Ukey K, Rameshchandra Sahu A, Sheshrao Gajghate S, Kumar Behera A, Limbadri C, Majumder H. Wire electrical discharge machining (WEDM) review on current

optimization research trends. Mater Today Proc [Internet]. 2023; Available from: https://www.sciencedirect.com/science/article/pii/S2214785323034958
181. Spierings A, Schneider M, Eggenberger R. Comparison of Density Measurement Techniques for Additive Manufactured Metallic Parts. Rapid Prototyp J. 2011 Aug 2;17:380–6.
182. Casalino G, Campanelli SL, Contuzzi N, Ludovico AD. Experimental investigation and statistical optimisation of the selective laser melting process of a maraging steel. Opt Laser Technol [Internet]. 2015;65:151–8. Available from: https://www.sciencedirect.com/science/article/pii/S0030399214002011
183. Obaton AF, Lê MQ, Prezza V, Marlot D, Delvart P, Huskic A, et al. Investigation of new volumetric non-destructive techniques to characterise additive manufacturing parts. Weld World. 2018 Jun 5;62.
184. Standard Guide for Additive Manufacturing of Metal — Finished Part Properties — Methods for Relative Density Measurement. 10.04:6. Available from: https://www.astm.org/f3637-23.html
185. Kruth JP, Bartscher M, Carmignato S, Schmitt R, Chiffre L, Weckenmann A. Computed tomography for dimensional metrology. Cirp Ann Technol - CIRP ANN-MANUF TECHNOL. 2011 Dec 31;60:821–42.
186. Hsieh J. Computed Tomography: Principles, Design, Artifacts, and Recent Advances. In 2003. Available from: https://api.semanticscholar.org/CorpusID:108848922
187. Gu Z, Sharma S, Riley DA, Pantawane M V, Joshi SS, Fu S, et al. A universal predictor-based machine learning model for optimal process maps in laser powder bed fusion process. J Intell Manuf. 2023;34(8):3341–63.
188. Yan F, Lin Z, Wang X, Azarmi F, Sobolev K. Evaluation and prediction of bond strength of GFRP-bar reinforced concrete using artificial neural network optimized with genetic algorithm. Compos Struct. 2017;161:441–52.
189. Shen T, Zhang W, Li B. Machine learning-enabled predictions of as-built relative density and high-cycle fatigue life of Ti6Al4V alloy additively manufactured by laser powder bed fusion. Mater Today Commun. 2023;37:107286.
190. Saboori A, Abdi A, Fatemi SA, Marchese G, Biamino S, Mirzadeh H. Hot deformation behavior and flow stress modeling of Ti–6Al–4V alloy produced via electron beam melting additive manufacturing technology in single β-phase field. Mater Sci Eng A. 2020;792:139822.
191. Ghanavati R, Naffakh-Moosavy H, Moradi M, Gadalińska E, Saboori A. Residual stresses and distortion in additively-manufactured SS316L-IN718 multi-material by laser-directed energy deposition: A validated numerical-statistical approach. J Manuf Process. 2023;108:292–309.
192. Chandra M, Vimal KEK, Rajak S. A comparative study of machine learning algorithms in the prediction of bead geometry in wire-arc additive manufacturing. Int J Interact Des Manuf. 2023;
193. Barrionuevo GO, Ramos-Grez JA, Walczak M, Betancourt CA. Comparative evaluation of supervised machine learning algorithms in the prediction of the relative density of 316L stainless steel fabricated by selective laser melting. Int J Adv Manuf Technol. 2021;113:419–33.

194. Toorandaz S, Taherkhani K, Liravi F, Toyserkani E. A novel machine learning-based approach for in-situ surface roughness prediction in laser powder-bed fusion. Addit Manuf [Internet]. 2024;91:104354. Available from: https://www.sciencedirect.com/science/article/pii/S2214860424004007
195. Zhao H, Ding Y, Li J, Wei G, Zhang M. Corrosion resistance of laser melting deposited Cu-bearing 316L stainless steel coating in 0.5 M H2SO4 solution. Mater Chem Phys. 2022 Aug 1;291:126572.
196. Liu Y, Yang J, Yang H, Li K, Qiu Y, Zhang W, et al. Cu-bearing 316L stainless steel coatings produced by laser melting deposition: Microstructure and corrosion behavior in simulated body fluids. Surf Coatings Technol [Internet]. 2021; Available from: https://api.semanticscholar.org/CorpusID:243474062
197. Hong IT, Koo CH. Antibacterial properties, corrosion resistance and mechanical properties of Cu-modified SUS 304 stainless steel. Mater Sci Eng A-structural Mater Prop Microstruct Process [Internet]. 2005;393:213–22. Available from: https://api.semanticscholar.org/CorpusID:53405797
198. Zhang Z, Zhang T, Sun C, Sivaji K, Yuan L. Understanding Melt Pool Behavior of 316L Stainless Steel in Laser Powder Bed Fusion Additive Manufacturing. Micromachines. 2024 Jan 23;15:170.
199. Saboori A, Aversa A, Marchese G, Biamino S, Lombardi M, Fino P. Microstructure and Mechanical Properties of AISI 316L Produced by Directed Energy Deposition-Based Additive Manufacturing: A Review. Appl Sci. 2020 May 9;10:3310.
200. Saboori A, Piscopo G, Lai M, Salmi A, Biamino S. An investigation on the effect of deposition pattern on the microstructure, mechanical properties and residual stress of 316L produced by Directed Energy Deposition. Mater Sci Eng A [Internet]. 2020;780:139179. Available from: https://www.sciencedirect.com/science/article/pii/S0921509320302653
201. Saboori A, Toushekhah M, Aversa A, Lai M, Lombardi M, Biamino S, et al. Critical Features in the Microstructural Analysis of AISI 316L Produced By Metal Additive Manufacturing. Metallogr Microstruct Anal. 2020 Jan 2;9.
202. Sohrabpoor H, Salarvand V, Lupoi R, Chu Q, Li W, Aldwell B, et al. Microstructural and mechanical evaluation of post-processed SS 316L manufactured by laser-based powder bed fusion. J Mater Res Technol [Internet]. 2021;12:210–20. Available from: https://www.sciencedirect.com/science/article/pii/S2238785421002167
203. Goldberg DE, Holland JH. Genetic algorithms and Machine Learning. Mach Learn [Internet]. 1988;3:95–9. Available from: https://api.semanticscholar.org/CorpusID:2043246
204. Ballard Z, Brown C, Madni AM, Ozcan A. Machine learning and computation-enabled intelligent sensor design. Nat Mach Intell. 2021;3(7):556–65.
205. Sui X, Downing JR, Hersam MC, Chen J. Additive manufacturing and applications of nanomaterial-based sensors. Mater Today. 2021 Sep;48:135–54.

Acknowledgments

I wish to convey my profound appreciation to my esteemed supervisor, Dr. Saboori, for his invaluable guidance, patience, and encouragement during this journey. His expertise, insight, and steadfast support have been crucial to completing this work. This achievement would not have been attainable without his mentorship and unwavering support, for which I am eternally grateful.

I deeply appreciate my husband, who has been my unwavering source of emotional strength and motivation. His patience, comprehension, and support throughout the numerous hours of research and writing, especially during my moments of self-doubt, have been invaluable to me. I appreciate your unwavering support and faith in me. I extend my sincere gratitude to my beloved parents, who, despite the distance, have demonstrated unwavering love and emotional support. Their distant encouragement has been a significant source of motivation, and I am fortunate to have them as my foundation. I am profoundly grateful to my parents for instilling in me the importance of education and diligence, as well as for their sacrifices and steadfast faith in my potential.

I am grateful to my colleagues and friends who have accompanied me on this journey. Your companionship, support, and insightful dialogues have enhanced my research experience and made it more pleasurable. I am writing to express my gratitude to the faculty and staff of the Integrated Additive Manufacturing Lab at Politecnico di Torino for supplying the resources and environment essential for conducting this research. Your assistance has been pivotal in accomplishing this task.